

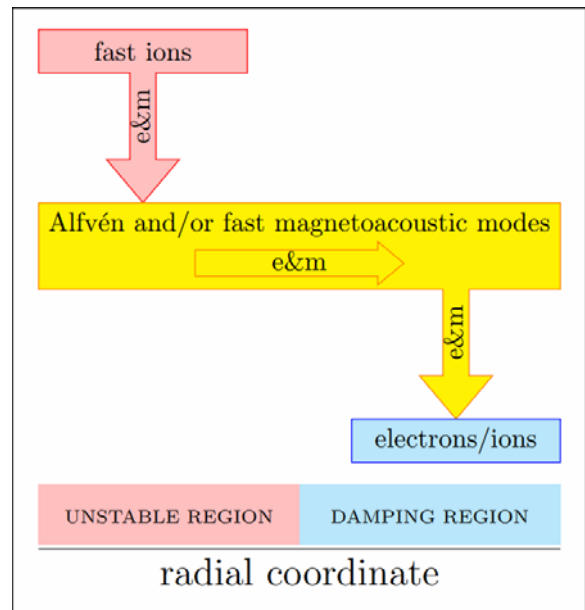
**A set of  
Synopsises of  
works which  
are planned to  
report at the  
KINR Annual  
conference-2020**

# PLASMA PHENOMENA CONNECTED WITH THE TRANSFER OF ENERGY AND MOMENTUM BY EIGENMODES

**A. V. Tykhyy**

*Institute for Nuclear Research, National Academy of Sciences of Ukraine, Kyiv, Ukraine*

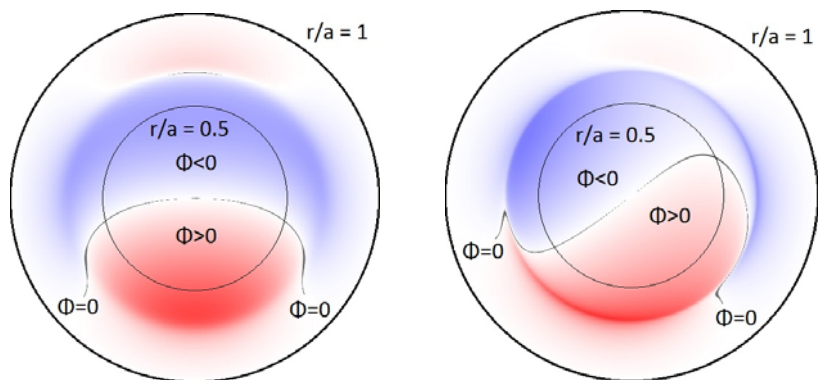
The phenomenon of SC of energy and momentum is a factor that can affect plasma performance in toroidal devices. It is associated with energetic ions produced by NBI, ICRH, and fusion reactions; but it can occur also in a Maxwellian plasma, being caused by suprathermal ions with energies exceeding the thermal energy by a few times. The latter is true, at least, for stellarators where Alfvén eigenmodes can be destabilized by the ion temperature gradient due to non-axisymmetric resonances. In the steady state, the mode energy flux is directed from the unstable region to the region where damping dominates, i.e., either outwards or inwards. However, when the drive exceeds the damping, so that the mode amplitude grows, the picture of the mode fluxes is more complicated, and both outward and inward wave energy / momentum fluxes in different plasma regions during the same instability may occur. Since SC transfers energy and momentum, it may affect plasma energy confinement (deteriorating or improving it), plasma rotation and concomitant frequency Doppler shift, the heating of the electron and ion components, and features of the eigenmodes themselves. In general, SC plays a considerable role when, first, the region driving the instability is well separated from the damping region and, second, the mode amplitudes are not very small.



Sketch of spatial channeling

The analysis in this work shows that SC due to high-frequency modes, with frequencies above and around the ion cyclotron frequency, is more likely to affect plasma energy balance for reasonable values of mode amplitudes than low-frequency Alfvén modes. Estimates for a JET-like tokamak with NBI heating power of about 10 MW show that modes with  $\omega \geq \omega_{Bi}$  and  $\omega \approx \omega_{Bi}$  (fast magnetoacoustic waves, global Alfvén eigenmodes, and high-frequency Alfvén modes present in stellarators such as Helicity- and Mirror-Induced Alfvén Eigenmodes) may directly affect plasma energy balance when mode amplitudes are reasonable ( $\delta B/B \sim 10^{-4}$ ), whereas low-frequency Alfvén modes with  $\omega \ll \omega_{Bi}$  can only affect plasma energy balance for mode amplitudes which seem unrealistic ( $\delta B/B \approx 2 \cdot 3 \cdot 10^{-3}$ ). On the other hand, SC of momentum can significantly affect sheared plasma rotation for  $\delta B/B \sim 10^{-4}$ , independently of mode frequency, especially on the plasma periphery.

Modification of the structure of Alfvén eigenmodes is considered. A radial dependence of the mode phase and concomitant curving of the wavefront due to SC is predicted by means of a simple qualitative analysis. This supports experimental findings in the DIII-D tokamak and in the NSTX spherical torus. The condition of the mode persistence (14) [4] was reformulated to be convenient for practical application.



Structure of TAE mode with  $m=1/2, n=1$  for weak SC (left) and strong SC (right)

These qualitative results were checked numerically by considering a low-mode-number TAE mode (with

$m=1 / 2, n=1$ ) in a tokamak with radially separated destabilizing and stabilizing regions. A model term describing the drive and damping, which enabled observation of the evolution of the mode by varying SC strength, was used. It is found that SC decreases the TAE frequency and makes the mode shape more peaked; when the local drive / damping is sufficiently large, the mode disappears, merging into the Alfvén continuum. These effects, obtained numerically, take place when SC is sufficiently strong, in agreement with the analytically obtained condition.

It is not clear whether / how the change of the modes caused by the SC affects the saturation level of the instabilities.

Till now, SC has been considered in connection with a limited number of experiments. It seems probable, however, that SC took place, although not recognized, in many experiments where Alfvén modes and fast magnetoacoustic modes were destabilized.

*This work was supported by the STCU-NASU Project No.~6392 and was partly carried out within the framework of the EUROfusion Consortium, having received funding from the EURATOM research and training programme 2014--2018 and 2019-2020 under grant agreement No.~633053. The views and opinions expressed herein do not necessarily reflect those of the European Commission.*

1. Kolesnichenko Ya.I., Tykhyy A.V., White R.B., 16th IAEA Technical Meeting on Energetic Particles in Magnetic Confinement Systems – Theory of Plasma Instabilities, Shizuoka, 2019.
2. Kolesnichenko Ya.I., Tykhyy A.V., White R.B., *Nucl. Fusion*, submitted.
3. Kolesnichenko Ya.I., Tykhyy A.V. 2018 *Phys. Lett. A* **382** 2689
4. Kolesnichenko Ya.I., Lutsenko V.V., Tyshchenko M.H., Weisen H., Yakovenko Yu.V. and the JET team 2018 *Nucl. Fusion* **58** 076012
5. Kolesnichenko Ya.I., Tykhyy A.V. 2018 *Phys. Plasmas* **25** 102507
6. Kolesnichenko Ya.I., Yakovenko Yu.V., Tyshchenko M.H. 2018 *Phys. Plasmas* **25** 122508
7. Kolesnichenko Ya.I., Tykhyy A.V. 2018 *Plasma Phys. Control. Fusion* **60** 125004

## DEVELOPMENT OF COMPTON CAMERA BASED ON MONOLITHIC SCINTILLATOR FOR PROMPT GAMMA-RAY IMAGING

A. Sh. Georgadze

*Institute for Nuclear Research, National Academy of Sciences of Ukraine, Kyiv, Ukraine*

We develop a new Compton gamma camera for imaging gamma-rays in the MeV region. The detector is based on cylindrical shape monolithic inorganic scintillator read-out on both ends with silicon photomultiplier (SiPM) arrays. GEANT4-based Monte Carlo simulation has been performed in order to evaluate the ability of the proposed camera to perform 3D reconstruction of hit positions in crystal scintillator of high energy gamma rays for gamma sources localization with the target on pulsed fast neutron analysis (PFNA). PFNA utilized microsecond wide fast neutron pulses produced by electronic neutron generator to initiate fast neutron inelastic scattering reactions on nuclei. Characteristic combination of prompt gamma-rays from nitrogen, carbon and oxygen nuclei excitations is an evidence of presence explosive materials. Since the fluorescence decay time of widely used and relatively cheap NaI(Tl), BGO and CsI scintillators can reach 300-1000 ns pulse pile-up become serious problem that cause resolution degradation, spectral distortion and peak position shift. In this case the choice is to use fast LaBr<sub>3</sub>(Ce) scintillator with <30 ns decay time. But this scintillator is 10-20 times more expensive and has relatively high intrinsic radiation background. To address these issues cylindrical shape monolithic scintillator III2"Q2" coupled to SiPMs arrays for double side readout were simulated using Geant4 optical transport. The photodetectors are composed of a 2x2 arrangement of 8x8 channels 3x3 mm<sup>2</sup> photosensitive area SiPMs arrays of the Ketek PA3325-WB-0808 which have in total 256 channels.

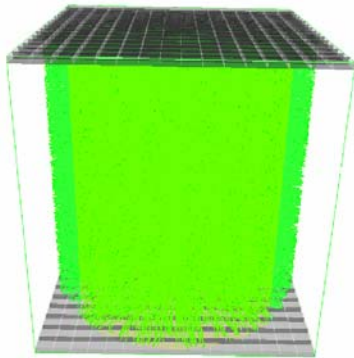


Fig. 1. The 3-D visualization by VRML driver of GEANT4 simulation of Compton camera.

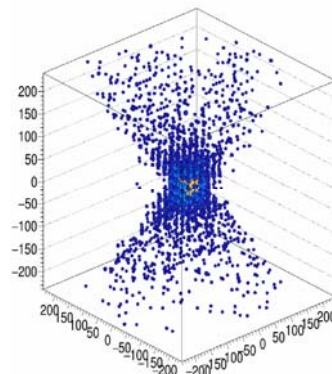


Fig. 2. Reconstructed hit positions of 4.4 MeV gamma-ray source at a distance of 1 m.

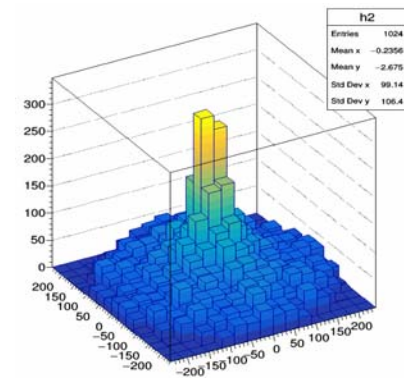


Fig. 3. Scintillation patterns observed from the side view of the detector unit for alpha particles.

Scintillators simulated in this work were NaI(Tl), BGO and LaBr<sub>3</sub>(Ce). On Fig. 1. the geometry of simulated Compton camera is presented. According to simulations gamma rays in the range 4-9 MeV undergo multiple Compton scattering inside the III2"Q2" cylindrical crystal. Interaction processes within the crystal scintillator were estimated by using the three-dimensional extended Anger-type calculation [2]. When multiple interaction occurred in a crystal, optical photons are generated and produce hit patterns on 256 pixels of top and 256 pixels of bottom SiPMs arrays. Center of gravity of these multiple interactions were reconstructed using the signals from both SiPMs arrays and the Anger-type formula:

$$x = \frac{1}{P} \sum_{i=1}^N p_i X_i, \quad y = \frac{1}{P} \sum_{i=1}^N p_i Y_i, \quad z = \frac{1}{P} \sum_{i=1}^N p_i Z_i, \quad P = \sum_{i=1}^N p_i$$

where  $p_i$  is the signal amplitude of the  $i$ th SiPMs channel, and  $X_i$ ,  $Y_i$  and  $Z_i$  are the physical  $x$ ,  $y$  and  $z$  coordinates of the  $i$ th SiPMs channel. In several percent of events multiple Compton scattering processes form scattering and absorption clusters which are spatially separated. Calculating centers of gravity and amplitudes of scattering and absorption clusters and using Compton scattering kinematics it is possible to

estimate location of a gamma-ray source by following the tracks of scattered gamma-rays backward according to without any mechanical collimation. According to preliminary simulation results high energy gamma rays undergo multiple Compton scattering inside the  $^{22}\text{Na}$  cylindrical crystal several percent of such events form the scattering and absorption clusters spatially separated. Center of gravity of scattering and absorption clusters can be resolved and used to calculate direction on the gamma-ray source.

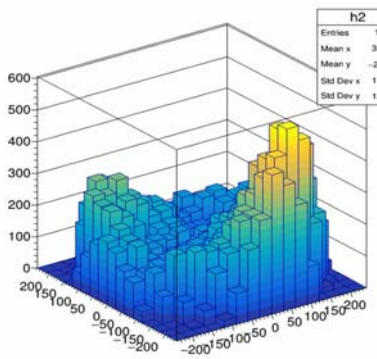


Fig. 4. Scintillation pattern of scattering and absorption clusters of Compton scattering event.

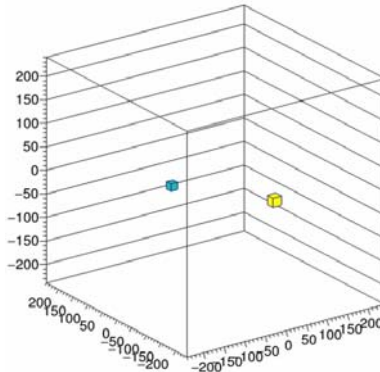


Fig. 5. Reconstructed positions of

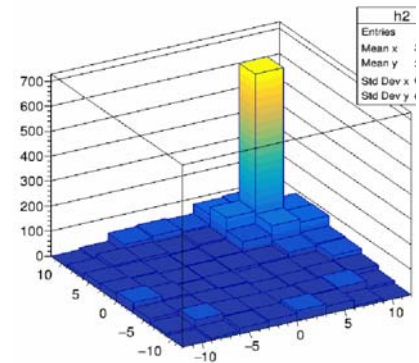


Fig. 6. Experimentally detected single Compton scattering event in  $^{22}\text{Na}$  NaI(Tl) scintillator.

Cluster analysis on event-by-event basis allow to separate Compton scattering events from alpha particle absorption events which are the main source of intrinsic background of  $\text{LaBr}_3(\text{Ce})$  scintillator thus improving its detection sensitivity. In case of two gamma quanta hitting the crystal simultaneously cluster analysis can reconstruct 3D positions of interaction events of gamma rays with scintillator and part of this events can be recognized as pile-up pulses and thus rejected. This will allow to use cheap but relatively slow NaI(Tl) and BGO scintillators for imaging gamma sources for the PFNA application as well as to improve performance of systems based on  $\text{LaBr}_3(\text{Ce})$  scintillators by rejecting internal backgrounds.

Preliminary measurements have been done with simplified setup using CAEN DT5550W board. The DT5550W is full featured Acquisition System with programmable FPGA which read out 4  $\text{PC}$  PETIROC2A ASICs. Two KETEK matrices (64 channels) are connected to board. The DT5550W has an onboard 14-bit 80 MS/s simultaneous sampling ADC, to monitor and acquire the analogue outputs of the ASICs. Energy and time stamped list mode output file provides timing information as well as energy. Compton scattering inside the  $^{22}\text{Na}$  cylindrical NaI(Tl) scintillator are easily reconstructed even with one side readout by KETEK SiPM array.

Performed simulations indicate that applying double sided readout of crystal scintillator with SiPMs arrays allow to use cheap but relatively slow NaI(Tl) and BGO scintillators for imaging gamma sources for the PFNA application as well as to improve performance of systems based on  $\text{LaBr}_3(\text{Ce})$  scintillators by rejecting internal backgrounds.

1. T. Iguchi et al. Conference: Nuclear Science Symposium Conference Record, 2005 IEEE, Volume: 2, P. 735.
2. Yamaya et al. Phys. Med. Biol. **56** (2011) 6793–6807.

# $\alpha + t(^3\text{He})$ INTERACTIONS AND EXCITATION SPECTRUM OF $^6\text{Li}$ NUCLEAR

O. K. Gorpinich, O. M. Povoroznyk

*Institute for Nuclear Research, National Academy of Sciences of Ukraine, Kyiv, Ukraine*

As a result of the fact, that the  $^6\text{Li}$  nucleus is one of the lightest with peculiar cluster structure of the ground and excited states, it is the object of intensive experimental and theoretical investigations during last decades. Excited states of the  $^6\text{Li}$  nucleus, like other lightest nuclei, are mostly unbound and decay due to the emission of clusters and nucleons. In Fig. 1 we report the  $^6\text{Li}$  energy levels given by compilations Ajzenberg-Selove [1] and Tilley [2].

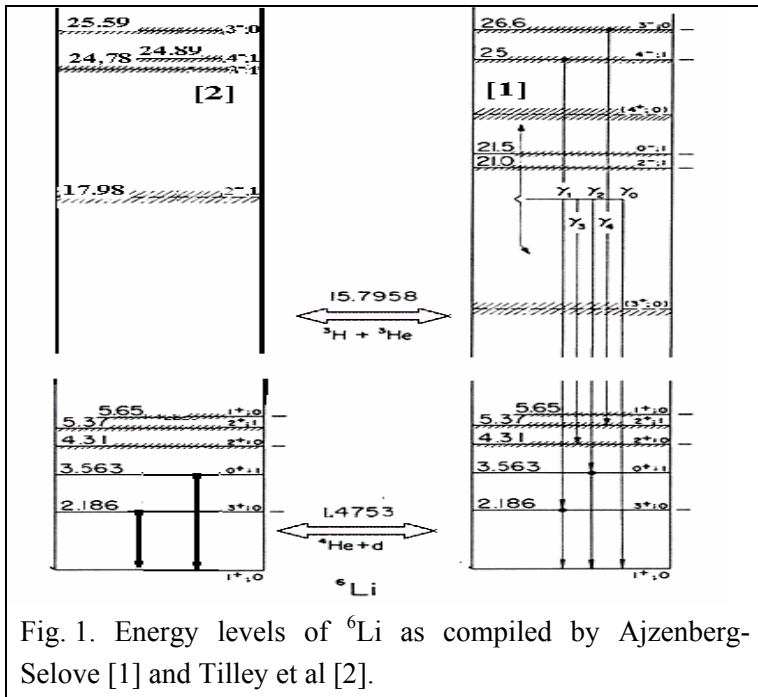


Fig. 1. Energy levels of  $^6\text{Li}$  as compiled by Ajzenberg-Selove [1] and Tilley et al [2].

Despite numerous investigations, the excitation spectrum of the  $^6\text{Li}$  nucleus is enough contradictory [1, 2], especially, at excitation energy above 6 MeV. But exact determination of excitation energy, time of life and modes of decay of unbound levels is very important for the more adequate understanding of nature of nuclear forces which cause their formation and decay.

The presented investigation is an analysis and generalization of our experiments directed to clarify the rather contradictory results of experimental studies of the structure of excitation spectrum of the  $^6\text{Li}$  nucleus. The most

widespread methods of determination of energy characteristics of unstable excited states are measurement and analysis of inclusive spectra from quasi- two particle reactions and study elastic scattering of decay components. The inclusive spectra frequently show a strong and continuous background from other states of the nucleus of interest, the decay of other nuclei produced in the competing reaction channels, and the statistical three-body break-up. But by investigating particle decay spectra in kinematical complete correlation experiment one can to obtain more specific and more exact information about unbound level of lightest nuclei

This work is a generalization of the cycle of research of  $^6\text{Li}$  nucleus [5-7]. using improved method particle decay [3,4] spectroscopy for study the numerous three and four body reaction channels caused by interaction  $\alpha$ -particle beams with hydrogen and helium isotopes

The subject of our research was the excited unbound levels of  $^6\text{Li}$  nucleus formed at the first stage of the interaction of beams of alpha particles with tritium and helium nuclei which at the second stage decayed through the emission  $\text{d} + \alpha$  or  $\text{t} + \tau$ . The resulting two-dimensional spectra  $E_p \times E_\alpha$ ,  $E_d \times E_\alpha$ , and  $E_t \times E_\tau$  were obtained from experimental kinematical complete study of three- body reactions:

For the first time, a kinematically complete study of the three-particle  $^3\text{He}(\alpha, \text{p}\alpha)\text{d}$  reaction on  $^3\text{He}$  nuclei of radiogenic origin accumulated in titanium-tritium targets was performed. The excitation energies obtained for the first observed 5 excited levels with energies of excitation less than 6 MeV and closed to presented in the compilation [2]. Energy widths are somewhat narrower.

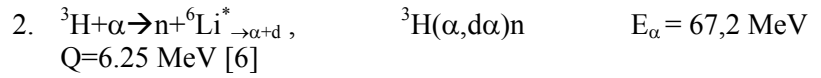
$$1. \quad ^3\text{He} + \alpha \rightarrow \text{p} + ^6\text{Li}^*_{\rightarrow \alpha + \text{d}}, \quad ^3\text{He}(\alpha, \text{p}\alpha)\text{d} \quad Q = 5.48 \text{ MeV} \quad (E_\alpha = 27,2 \text{ MeV}) [5]$$

In obtained from investigation of three-body  $^3\text{H}(\alpha, \text{d}\alpha)\text{n}$  reaction two-dimensional  $E_p \times E_\alpha$  spectra ( $E_\alpha = 67,2 \text{ MeV}$ ) [6] one can firstly observed three unbound excited levels in energy range of the excitation energy of the  $^6\text{Li}$  nucleus from 7 to 14 MeV. Obtained new experimental data about the excited states of  $^6\text{Li}$  are agreed with theoretical calculations [7-11] and also with experimental investigations of other authors [12,13].

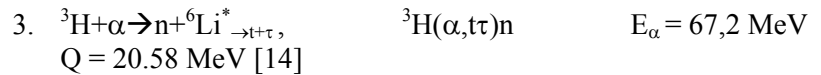
Table 1. Energy parameters of excited states  ${}^6\text{Li}$ 

$N\alpha$	$E^*, \text{MeV}$	$\Gamma, \text{MeV}$
1	2.22(0.20)	0.20(0.15)
2	3.50(0.25)	-
3	4.44(0.30)	0.40 (0.20)
4	5.15(0.25)	0.40 (0.25)
5	5.85(0.30)	0.72(0.20)
$E_\alpha=67,2 \text{ MeV } {}^3\text{H}(\alpha, \text{d}\alpha)\text{n}$		
${}^3\text{H}+\alpha \rightarrow \text{n}+{}^6\text{Li}^* \rightarrow \alpha+\text{d}$ [7]		
6	8.80(0.15)	1.85(0.70)
7	11.30(0.40)	1.30(1.10)
8	13.50 (0.40)	1.45(1.50)
$E_\alpha=67,2\text{MeV } {}^3\text{H}(\alpha, \text{t}\tau)\text{n}$		
${}^3\text{H}+\alpha \rightarrow \text{n}+{}^6\text{Li}^* \rightarrow \text{t}+\tau$ [8]		
9	21.30 (0.30)	0.25(0.30)
10	21.90 (0.40)	0.4 (0.2)

the three-particle channels.



As a result of the study of  ${}^3\text{H}(\alpha, \text{t}\tau)\text{n}$  in kinematically complete experiment at incident energy  $E_\alpha = 67.2 \text{ MeV}$  we have observed the excited  ${}^6\text{Li}$  levels at 21.30 and 21.90 MeV [14]. Two measured peaks of the  ${}^6\text{Li}$  levels are consistent with the theoretical calculations of Thompson and Tang [15] that have made a study on the cluster structure of excited  ${}^6\text{Li}$  and  ${}^6\text{He}$  levels. Besides, these results agree with the analysis coming from  $\text{t}+\tau$  elastic scattering reported by Ajzenberg-Selove [16] and also partly with the recent  ${}^7\text{Li}({}^3\text{He}, \alpha){}^6\text{Li}$  experiment because only one of the two above-mentioned  ${}^6\text{Li}$  levels was present [17].



In the table are presented the results of our studies devoted to determining the structure of the of  ${}^6\text{Li}$  nucleus excitation spectrum, which were performed through a kinematically complete study of the

1. Ajzenberg-Selove F. // Nucl. Phys. - 1988. - Vol. A490. - P.1 - 225.
2. Tilley D.R., Cheves C.M., Godwin J.L. et al. //Nucl. Phys. - 2002. - Vol. A708. - P. 3 - 163.
3. Povoroznyk O.M.//Nuclear Physics and Atomic Energy Kyiv. 2007.-No2(20)- C.131 - 139
4. Gorpnich O.K., Povoroznyk O.M. //  $\alpha+\text{t}$  three-body reactions and excited levels of lightest nuclei // Physics and Atomic Energy . Kyiv.- 2007.- No 1(19). - p. 53 - 60.
5. Povoroznyk O., Gorpnich O.K., Jachmenjov O.O.// Determination energy parameters of unbound states of  ${}^6\text{Li}$  to energy excitation 6MeV //Ukr.J.Phys.2004.V.50.№4.P. 327-333
6. Povoroznyk O., Gorpnich O.K., Jachmenjov O.O. //Investigation of excited levels of  ${}^6\text{Li}$  nucleus from the three-particle  ${}^3\text{H}(\alpha, \text{d}\alpha)\text{n}$  reaction //Ukr.J.Phys.2004.V.49.№1.P. 16-20
7. Zheng D.C., Barrett B.R., Vary J.P., Haxton W.C. and Song C.-L // Phys. Rev C. -1995.- 52.- P 2488.
8. Navratil P.and Barrett B.R. // Phys. Rev. C 54.- 1996.- P.2986.
9. Ershov S.N., Rogde T., Danilin B.V., Vaagen J.S., Thompson I.J. and Gareev F.A. // Phys. Rev. C. - 1997.-56.-P.1483.
10. Danilin B.V., Thompson I.J., Vaagen J.S. and Zhukov M.V. //Nucl. Phys.- 1998.- A632.- P.383.
11. Kato K., Aoyama S., Mukai S. and Ikeda K. //Nucl. Phys. A.- 1995.-588.-P.29;  
Aoyama S., Mukai S., Kato K and Ikeda K. //Prog. Theor. Phys. -1995.-94.- P.343.
12. Delbar T., Gregoire G.and Paic G. //Phys. Rev. C.- 1983.-27.- P.1887.
13. Jenny B., Græbler W., Kunig V. et al. // Nucl.Phys.-1983.-A397.- P.61
14. Povoroznyk O., Gorpnich O.K., Jachmenjov O.O., . et al.// J.Phys.Soc.Jpn. 80, 094204 (2011)
15. Thompson D.R. and Tang Y.C. Phys. Rev. Lett. **19**, 87 (1967)
16. Ajzenberg-Selove F.. Nucl. Phys. A **413**, 1 (1984)
17. Nakayama S., Yamagata T., Akimune H., et al. Phys. Rev. C **69**, 041304 (2004)

## COLOR STATISTICS FOR NUCLEAR MATTER: HOW DOES IT WORK?

**V. Maslyuk, O. Parlag, M. Romanyuk**

*Department of Photonuclear Processes, Institute of Electron Physics, Uzhhorod, Ukraine*

It has known well the importance of studying the creation, stability, and transformation of atomic nuclei for understanding the basics of matter structure [1]. The result of nuclei transformations is the mass/charge spectra of fission-fragment (MCSFF) of nuclei. The topology of MCSFF is determined by the factors of stability of nuclear matter. Now, there are different theoretical approaches to describe the formation of fission fragments yield and the topology of their MCSFF as a rule on various modifications of the liquid drop model. Such approaches form the basis for a pre scission approximation since the regularities of formation of fragments are deduced from the processes that precede nucleus fission. In [2-8], a new approach, post scission approximation was proposed, which investigate the thermodynamic ordering of the ensemble of fission fragment clusters formed after the scission of the fissile nucleus. Although the thermodynamic method has a powerful mathematical ability, its application to nuclear systems requires special justification. Firstly, because nuclei are small systems and the theory must take into account the statistical fluctuations of thermodynamic parameters - temperature, T, pressure, R. The role of the thermostat, which maintains these parameters unchanged for the ensemble of nuclei fragments, has plays exactly the initial (fissile) nucleus with atomic mass  $A_0$  and the charge  $Z_0$ . Another problem is that the binding energy of a nucleus is not additive on a number of their nucleons, both protons/neutrons. Moreover, the binding energies of a single nucleon are different for different fission fragments. The ordering of the nuclear clusters can not be described within the known particles statistics. This can be done within the color statistics, called by the combinatorics of colored balls, which able to account the statistical non-equivalency of fragments' nucleons [2]. Colour statistics can be used to describe the thermodynamic ordering, for example, of two-fragment clusters that forming the post scission ensemble. Moreover, the theory based on colour statistics can explain the transformation of the MCSFF after post fission emission of nuclear particles, neutrons, and  $\pm\beta$ . In the case of building the post scission ensemble of two fragment clusters, the two-boxes model can be used. The boxes filling shall take into account the following conservation conditions:

$$\sum_{j=1,2} N_{p,i}^{(j)} + N_{n,i}^{(j)} + m_i = A_0, \quad \sum_{j=1,2} N_{p,i}^{(j)} + n_i = Z_0; \quad (1)$$

Here, the i-number of the cluster containing protons, neutrons in the j-th fragments,  $j = 1, 2$  that are formed before or after the emission of the  $m_i$  -neutrons and n-beta particles. The theory allows one to expand the number of ensembles, each of which may be builds with fission fragments after postscission emission of different lengths' chains of nuclear particles. Consideration should also be given to work,  $P\Delta v_i$  must be in the same order as T [9]. To investigate the equilibrium condition of the ensemble of fission fragments and MCSFF one must use the Gibbs thermodynamic potential  $G = U - TS + PV$ , where U the internal energy for which the spectrum values  $\{\varepsilon_i(V)\}$  is determined from a summing of binding energies of fission fragments for volume V. The configurational entropy S is calculated through the degeneracy factor that accounts the formal "color" or statistical nonequivalence of nucleons with different specific binding energies in the fission fragments and the presence of fission neutrons. For i-th cluster  $S_{i\beta} = \ln(w_i)$ , where:

$$w_i = A_0! K(n_j) / \left( \prod_{j=1,p} (N_p^{(j)}! N_n^{(j)}! n_j! \right). \quad (2)$$

$K(n_j) = 1 / \left( \prod_{j=1,2} n_j! \right)$ ,  $\prod_{j=1,2} x_j! = x_1! x_2!$ . Such an approach allows one to calculate the probabilities of realization (yield) of nuclear clusters of j-th sorts []. The next step is going to the distribution function  $F(A_i)/F(Z_i)$  or the probability of the yield of a single fission fragment with the mass ( $A_i$ ) / charges ( $Z_i$ ), and therefore MCSFF.

It should be noted that proposed statistical method contains no adjustable parameters, but only those that can be obtained from experiment. For instance, the temperature T can be defined by analyzing the evaporation spectra of the fission neutrons/protons or fission fragments. The isobaric constant  $P\Delta v$  appearing in the Gibbs thermodynamic potential G can be evaluated from the condition  $P\Delta V = \Delta NT$  and if  $\Delta N \sim 1$  the value of  $P\Delta v$  must be in the same order as T. The binding energies are given, in the well-known systematics of mass formulas. Therefore, withing the post scission approximation, it can describe various

effects related to nucleus separation: the isobaric spectra of Kr, Xe, Rh, Rn at the fission of U, Np, Pu, Th [4]; function of neutron activity [2], MCSFF to both actinide and super-heavy nuclei [6,7]. Other examples of having been using of color statistics are shown in Fig. 1, 2.

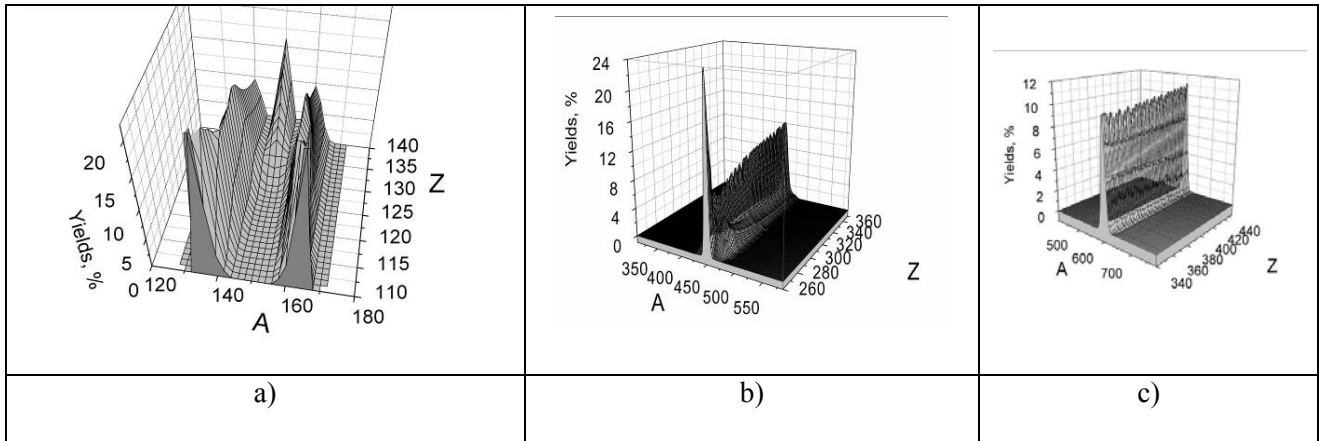


Fig. 1 Mass spectra of fission fragments of hypothetical nuclei with mass numbers:  $A=300$  - a),  $A=900$ - b) and  $A=1200$  c) [4].

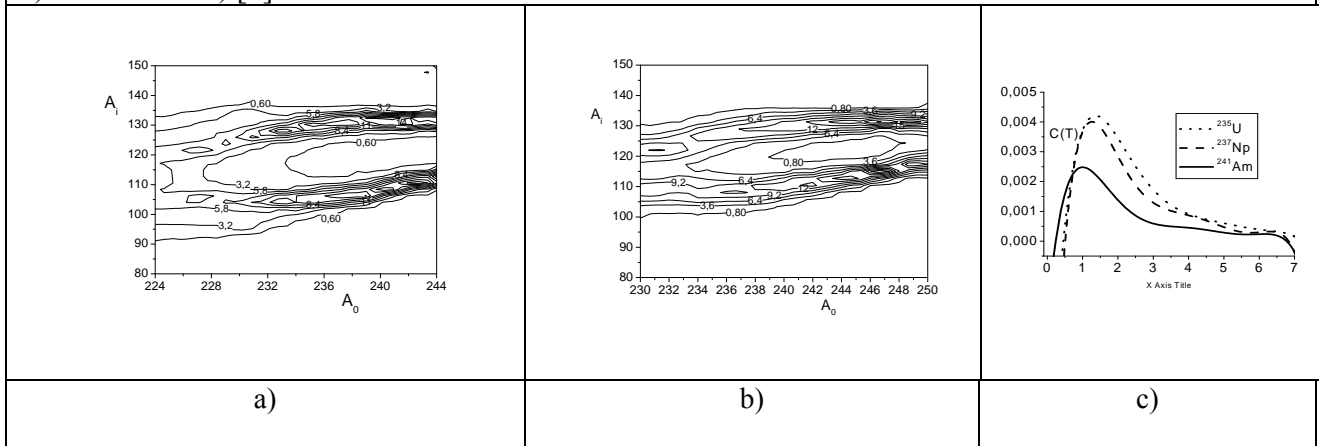


Fig. 2 Mass spectra of fission fragments of  $^{231-249}\text{Am}$ , - a),  $^{224-244}\text{Np}$  - b) and heat capacity  $C(T)$ , see [8] for  $^{235}\text{U}$ ,  $^{237}\text{Np}$ ,  $^{241}\text{Am}$  isotopes

1. V. Denisov, V. Plyuyko. Problems of nuclear physics and nuclear reactions: (K.: Kyiv, 2013) 430 p.
2. V.. Maslyuk, Ukr. Fiz. Zh. 41(11-12), 1029–1031 (1996).
3. V. Maslyuk et al, Intern. J. Phys 6(1-2), 1–8 (2000)
4. V. Maslyuk. NPAE-Kyiv2012. Proceedings. Part I and Part II P.308-311
5. V. Maslyuk et al, Phys. Part. Nuclei Lett., 2007, Vol. 4, No. 1, pp. 46–50.
6. V. Maslyuk et al, Nucl/Phys. A 955, 79 (2016)
7. V. Maslyuk, et al EPL 119, 12001 (2017).
8. V. Maslyuk, et al Phys. Rev. C, 98, 2018, 064608.
9. O.G. Sitenko, V.K. Tartakovsky. Theory of nucleus (K., Lebid', 2000) 607 p. (in Russian).<sup>1</sup>

## MICROSTRIP AND MICROPIXEL DETECTORS FOR STUDIES OF CALIX[4]ARENES MOLECULES RESPONSE TO EXCITATION BY UV AND VISBLE LIGHT

**A. Puhach<sup>1</sup>, M. Campbell<sup>2</sup>, V. Kyva<sup>3</sup>, X. Llopart<sup>2</sup>, V. Militsiya<sup>3</sup>, V. Pugatch<sup>3</sup>, D. Storozhyk<sup>3</sup>**

<sup>1</sup> Taras Shevchenko National University of Kyiv, Kyiv, Ukraine

<sup>2</sup> CERN, Geneva, Switzerland

<sup>3</sup> Institute for Nuclear Research , National Academy of Sciences of Ukraine, Kyiv, Ukraine

Calix[n]arenes are organic molecules, that contain phenol rings and can be characterised by a three-dimensional bucket-like shape. There is a vast array of calix[n]arenes and their properties can vary, depending on the number of phenol rings and the type of functional groups, which a certain calix[n]arene carries [1]. In this study, a specific type of calix[n]arene was used – thiacalix[4]arene C-800. Its main feature is the presence of 4 phosphate groups, which are responsible for binding various metals. Another important property of thiacalix[4]arene C-800 is its ability to fluorescence in the UV spectrum. Previous studies demonstrate, that thiacalix[4]arene can selectively bind Zinc cations. This binding results in significant elevation of fluorescence intensity level (Fig. 1). A maximum emission for thiacalix[4]arene C-800 is 385 nm, which can be achieved at 340 nm excitation wavelength.

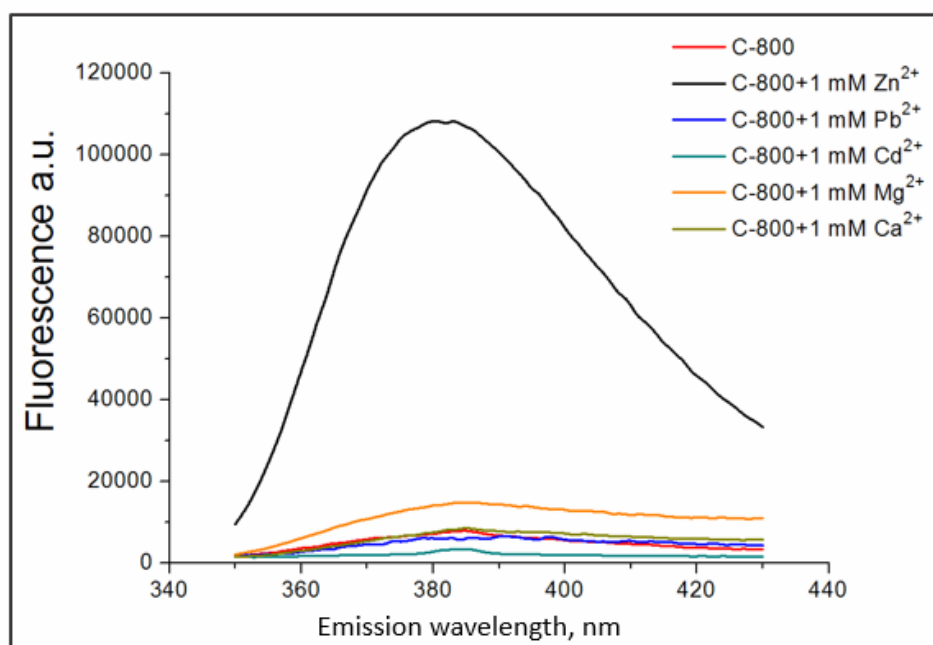


Fig. 1. Thiacalix[4]arene C-800 fluorescence emission spectra (excitation wavelength 340 nm) and the impact of various metals on thiacalix[4]arene C-800 fluorescence intensity.

Zinc is the second most abundant trace element (after iron) in most living organisms, including humans. It is considered important to gain a better understanding of Zn<sup>2+</sup> pathways of signaling and its penetration into the cells [2].

In this presentation we report on the experimental setup designed and built for studies of the calix[n]arenes molecules position and time resolved response to excitation by UV and visible light sources. The technical features of the setup have to match the fact that a size of the cells with calix[n]arenes molecules and absorbed Zn atom is in the range of few tens  $\mu\text{m}$ , while a fluorescence time for Zn<sup>2+</sup> does not exceed 20 ns.

The start up option of the setup is equipped with UV and visible light emitting sources, triggered by the pulse generator with 10 ns time duration. The size of the beam spot after focusing is in the range of 7  $\mu\text{m}$ .

Figure 2 illustrates a technical possibility of the setup to measure the intensity of the emitted light from few  $\mu\text{m}$  regions of interest (a size of the cells with calix[n]arenes molecules is about 25  $\mu\text{m}$ ). This result has been obtained by measuring coincident response of two adjacent strips of the Si microstrip detector with a pitch of 50  $\mu\text{m}$  irradiated with a 640 nm light diode moved over the interstrip gap in 5  $\mu\text{m}$  steps.

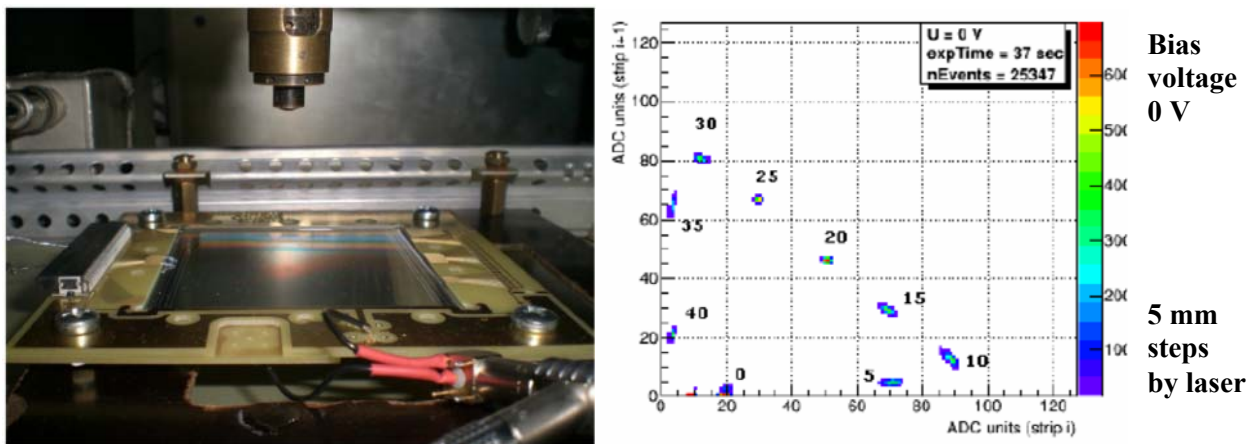


Fig. 2. *Left panel*: Photo of the experimental setup for studies with a Si (unbiased, 0V) microstrip detector irradiated by the focused laser beam on a movable platform.

*Right panel*: Coincident two-dimensional amplitude response of two adjacent strips (50  $\mu\text{m}$  gap) to a laser moved across the interstrip gap in a 5 mm steps.

Similar results will be presented for the irradiation by the UV light diode, measured also by means of a hybrid micropixel detector Timepix, developed at CERN [3]. With its 256 x 256 pixels (55 x 55  $\mu\text{m}^2$ ) structure it allows to allocate regions with UV light emitted from the regions of interest with a precision of 18  $\mu\text{m}$  [4]. In this study the data were obtained for water solutions with pure calix[n]arenes cells, as well as mixed with Zn atoms. The results indicate an enhancement of the emitted light for the second case. Further studies will be performed by measuring a time evolution of the emitted light applying the newest version of the micropixel detector Timepix4 with a time resolution of about 25 ps.

1. Gutsche C. D. Calixarenes // Cambridge: Royal Society of Chemistry. – 1989. – №3. – p. 210.
2. Maret W. Zinc in Cellular Regulation: The Nature and Significance of "Zinc Signals" // International journal of molecular sciences. – 2017. – № 18. – pp. 1 – 12.
3. Llopart X., Ballabriga R., Campbell M. et al. Timepix, a 65k programmable pixel readout chip // Nucl. Instr. and Meth. - 2007. - Vol. A581. - P. 485 - 489.
4. John Vallerga, Jason McPhate, Anton Tremsin, Oswald Siegmund High-resolution UV, alpha and neutron imaging with the Timepix CMOS readout. Nuclear Instruments and Methods in Physics Research A 591 (2008) 151–154

## ISOSCALAR DIPOLE RESPONSE OF HEAVY NUCLEI IN LOW-ENERGY REGION WITHIN KINETIC MODEL

**V.I. Abrosimov, O.I. Davydovska**

*Institute for Nuclear Research, National Academy of Sciences of Ukraine, Kyiv, Ukraine*

The isoscalar dipole response of heavy spherical nuclei in low-energy region is studied by using a translation-invariant kinetic model, based on the solution of the linearized Vlasov kinetic equation for finite Fermi systems [1]. In this model, a nucleus is treated as a gas of interacting fermions confined to a spherical cavity with moving surface. Within our kinetic model, one can find the explicit expression for the fluctuation of the phase-space distribution function related to the collective isoscalar dipole excitations. By using this function, one can calculate the response function [1] as well as the local dynamical quantities, in particular, the velocity field [2]. The velocity field describes the spatial distribution of the average nucleon velocity under a collective excitation and provides information on the nature of the excitation. In this paper, the velocity fields associated with low-energy collective isoscalar dipole excitations are studied [3].

Isoscalar dipole excitations in finite Fermi systems are an effect of the second order for the dipole moment (in the first order, they reduce to the center-of-mass motion). So, we consider the isoscalar dipole response of heavy nuclei to a weak external field of the kind

$$V(\vec{r}, t) = \beta \delta(t) Q^{(3)}(r) Y_{10}(\theta, \varphi), \quad (1)$$

where  $Q^{(3)}(r) = r^3$  is the second-order dipole moment,  $\delta(t)$  is the Dirac delta-function in time, and  $\beta$  ( $\beta = \text{const} \ll 1$ ) is a parameter that describes the external field strength. Since the external field (1) can also excite the center of mass, the problem arises of extracting spurious strength from the response function. Our translation-invariant model allows for a clear way to evaluating of the intrinsic response function associated with the field (1). By looking at the response of the center of mass induced by the external field (1), we can get [1]:

$$\tilde{R}_{c.m.}(\omega) = \frac{3}{4\pi} \frac{AR^4}{m\omega^2}, \quad (2)$$

where  $R$  is the equilibrium radius of the system, the value of  $\omega$  defines the excitation energy of the nucleus ( $E = \hbar\omega$ ) and  $m$  is the nucleon mass. Since this response function has no poles for  $\omega \neq 0$ , it does not give spurious dissipation at positive  $\omega$ . Then the internal response function that is related to the collective isoscalar dipole excitations can be determined as

$$\tilde{R}_{inv}(\omega) = \tilde{R}_{33}(\omega) - \tilde{R}_{c.m.}(\omega), \quad (3)$$

where  $\tilde{R}_{33}(s)$  is the collective dipole response function. An essential property of intrinsic response function (3) is that its limit for  $\omega \rightarrow 0$  is finite, so it has no pole in  $\omega = 0$ .

The low-energy part of the isoscalar dipole strength function  $S(E) = -(1/\pi) \text{Im} \tilde{R}_{inv}(E)$  is shown in Fig. 1.

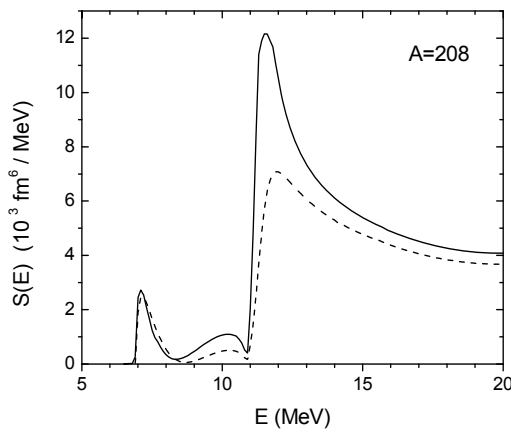


Fig. 1. Isoscalar dipole strength function in the low-energy region taking into account the residual interaction between nucleons (solid curve) and in the zero-order approximation (dashed curve). The system contains  $A=208$  nucleons.

We consider the isoscalar dipole response of a sample ‘nucleus’ of  $A=208$  nucleons. Dipole response functions calculated for other values of  $A$ , corresponding to other medium-heavy spherical nuclei, are qualitatively similar to the case shown in Fig. 1. The isoscalar dipole strength function displays three resonance structures in the low-energy region at the centroid energies of 11,5 MeV, 10,2 MeV, and 7,1 MeV, see the solid curve in Fig. 1.

Fourier-transform in time of the velocity field is determined as

$$\vec{u}(\vec{r}, \omega) = \frac{1}{m\rho_0} \int d\vec{p} \vec{p} \delta n(\vec{r}, \vec{p}, \omega), \quad (4)$$

where  $\delta n(\vec{r}, \vec{p}, \omega)$  is the (Fourier transformed in time) fluctuations of the phase-space particle distribution induced by a weak external field (1), and  $\rho_0$  is the nuclear equilibrium density. Choosing the  $Z$  axis in the direction of the external field, we consider the velocity field in the meridian plane  $XZ$ . In this representation, the radius-vector of particle is  $\vec{r} = (x, y=0, z)$  or  $\vec{r} = (r, \theta, \varphi=0)$  in the spherical coordinates and the velocity field (4) can be written as

$$\vec{u}(r, \theta, \varphi=0, \omega) = u_x(r, \theta, \omega) \vec{e}_x + u_z(r, \theta, \omega) \vec{e}_z, \quad (5)$$

where  $u_x(r, \theta, \omega)$  and  $u_z(r, \theta, \omega)$  are the projections of the velocity field vector into the  $X$  and  $Z$  axes, respectively, and  $\vec{e}_x, \vec{e}_z$  are unit vectors directed along these axes. The results of numerical calculations of the velocity fields associated with the low-energy resonance structures of the dipole strength function at centroid energies are shown in Fig. 2. Calculations display the vortex (toroidal) nature of two overlying

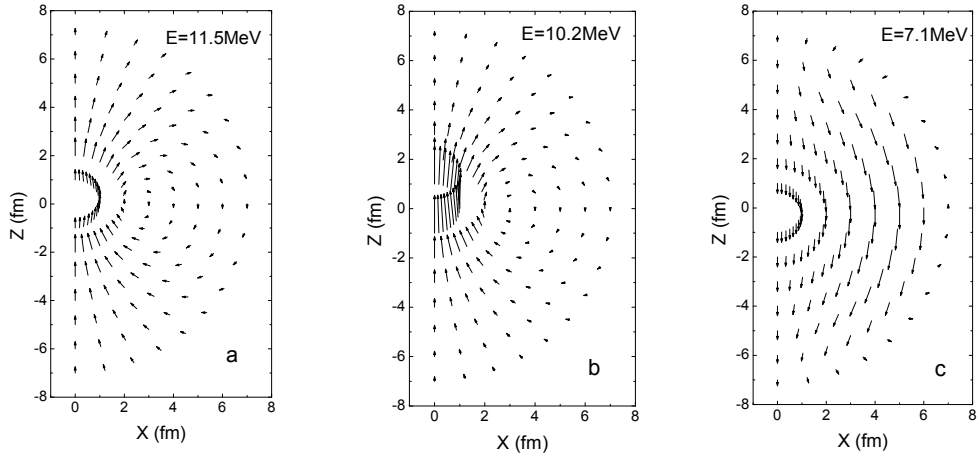


Fig. 2. Velocity fields in the  $XZ$ -plane associated the low-energy resonance structures of the dipole strength function at the centroid energies of 11,5 MeV, 10,2 MeV, and 7,1 MeV, see Figure 1 (solid curve). The system contains  $A=208$  nucleons.

resonances at the centroid energies of 11,5 MeV and 10,2 MeV, see Fig. 2(a and b). The main toroidal resonance at the centroid energy of 11,5 MeV gives a qualitative description of the low-energy isoscalar dipole resonance, which is observed in heavy spherical nuclei. The velocity field for the lowest isoscalar dipole resonance structure at the centroid energy of 7,1 MeV, see Fig. 2c, does not show vortex motion, however, taking into account the residual interaction leads to collectivity in this resonance, which may be due to dynamic deformation of the Fermi surface.

Our semiclassical approach makes it possible to obtain additional information on the nature of collective isoscalar dipole excitations in heavy nuclei. In particular, it would be interesting to study the nature of the momentum flux associated with collective isoscalar dipole excitations. This study could clearly show the effect of dynamic deformation of the Fermi surface on the formation of nuclear low-energy resonances.

1. V.I. Abrosimov, O.I. Davidovskaya. Ukr. J. Phys. 61 (2016) 565.
2. V.I. Abrosimov, O.I. Davydovska. Ukr. J. Phys. 63 (2018) 1043.
3. V.I. Abrosimov, O.I. Davydovska. arXiv: 1911.09759 [nucl-th]. 2019 (10 pages); Nucl. Phys. and At. Energy., accepted, 2020.

## EMPIRICAL RELATIONS FOR THE FUSION CROSS SECTIONS OF HEAVY IONS

**V. Yu. Denisov**<sup>1</sup>

<sup>1</sup>*Institute for Nuclear Research, National Academy of Sciences of Ukraine, Kyiv, Ukraine*

The goal is to find the simple formulas for quick evaluation of the fusion cross section around the barrier with smooth dependencies of parameters from one system to another. There is the database of the experimental data of heavy-ion fusion cross sections [1]. This database includes datasets for 1621 reactions measured for various heavy-ion systems at different collision energies. Using this database we select 85 heavy-ion reaction datasets, which related to the measurements of the fusion cross section around barrier at 1995 values of the collision energies measured in heavy-ion systems ranging from  $^{12}\text{C}+^{12}\text{C}$  with  $Z_1Z_2=36$  to  $^{58}\text{Ni}+^{124}\text{Sn}$  with  $Z_1Z_2=1400$ , where  $Z_i$  is the number of protons in nucleus  $i$ . We choose systems consisting of spherical or near spherical even-even nuclei. We select relatively modern data sets, which contain the cross-section values measured in a wide range of collision energies.

Our approach is based on the Wong formula for the fusion cross section of spherical nuclei [2]

$$\sigma(E) = 10 R^2 \square\omega / (2E) \ln[1 + \exp(2\pi(E-B)/(\square\omega))].$$

The Wong formula depends on the collision energy  $E$ , the height  $B$ , and curvature  $\square\omega$  of the barrier. Using selected datasets, we find the simple formulas [3] for the evaluation of the barrier radius

$$R = R_1 + R_2 + 1.5701, \quad R_i = 1.2932 A_i^{1/3} - 4.1615/A_i,$$

height

$$B = Z_1 Z_2 e^2 / R$$

and curvature

$$\square\omega = [153.23 Z_1 Z_2 (A_1 + A_2) / (A_1 A_2 R^3)^{1/2}] [1 + 2.5031 g_2 f(E) + 26.253 g_3 f(E) + 0.23335 Q_{1n} + 0.27863 Q_{2n}],$$

where

$$g_2 = A_1^{1/3} \beta_{21} / \varepsilon_{21} + A_2^{1/3} \beta_{22} / \varepsilon_{22}, \quad g_3 = A_1^{1/3} \beta_{31} / \varepsilon_{31} + A_2^{1/3} \beta_{32} / \varepsilon_{32}, \quad f(E) = (E/B)^3 [1 + \exp[-0.14215 (E-B)]].$$

Here  $\beta_{Li}$  and  $\varepsilon_{Li}$  are the vibration amplitude and energy of the low-energy multipole surface oscillation in nucleus  $i$ ,  $Q_{kn}$  is the Q-value of k-neutron transfer with positive value. The barrier radius and height do not depend on the collision energy, while the barrier curvature depends on the collision energy strongly in our approach. Substituting these formulas into the Wong formula, we can quickly calculate the fusion cross section of heavy ions [3]. Our parametrization is useful for the calculation of the astrophysical S-factor. The energy dependence of the astrophysical S-factor for reactions  $^{12}\text{C}+^{12}\text{C}$ ,  $^{12}\text{C}+^{14}\text{C}$ ,  $^{14}\text{C}+^{14}\text{C}$ ,  $^{12}\text{C}+^{18}\text{C}$ , and  $^{18}\text{C}+^{18}\text{C}$  is presented in Fig. 1. Note the values of S factor for reaction  $^{12}\text{C}+^{18}\text{C}$  are evaluated with and without the influence of  $1n$  and  $2n$  transfers. The neutron transfer is strongly enhanced the S-factor values for this system. The comparison of the energy dependence of the heavy-ion fusion cross section around barrier for some systems is presented in Fig.2.

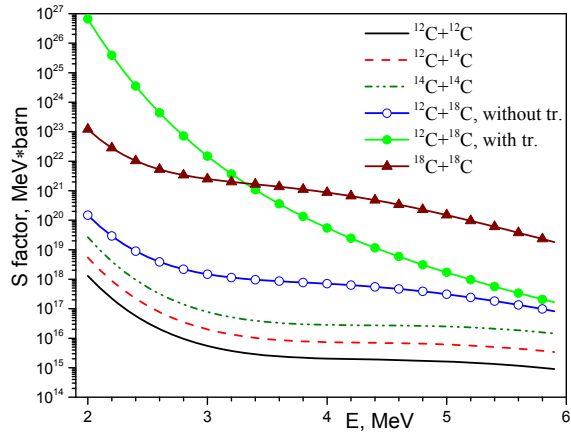


Fig. 1. The energy dependence of the astrophysical S-factor for reactions reactions  $^{12}\text{C}+^{12}\text{C}$ ,  $^{12}\text{C}+^{14}\text{C}$ ,  $^{14}\text{C}+^{14}\text{C}$ ,  $^{12}\text{C}+^{18}\text{C}$ , and  $^{18}\text{C}+^{18}\text{C}$ .

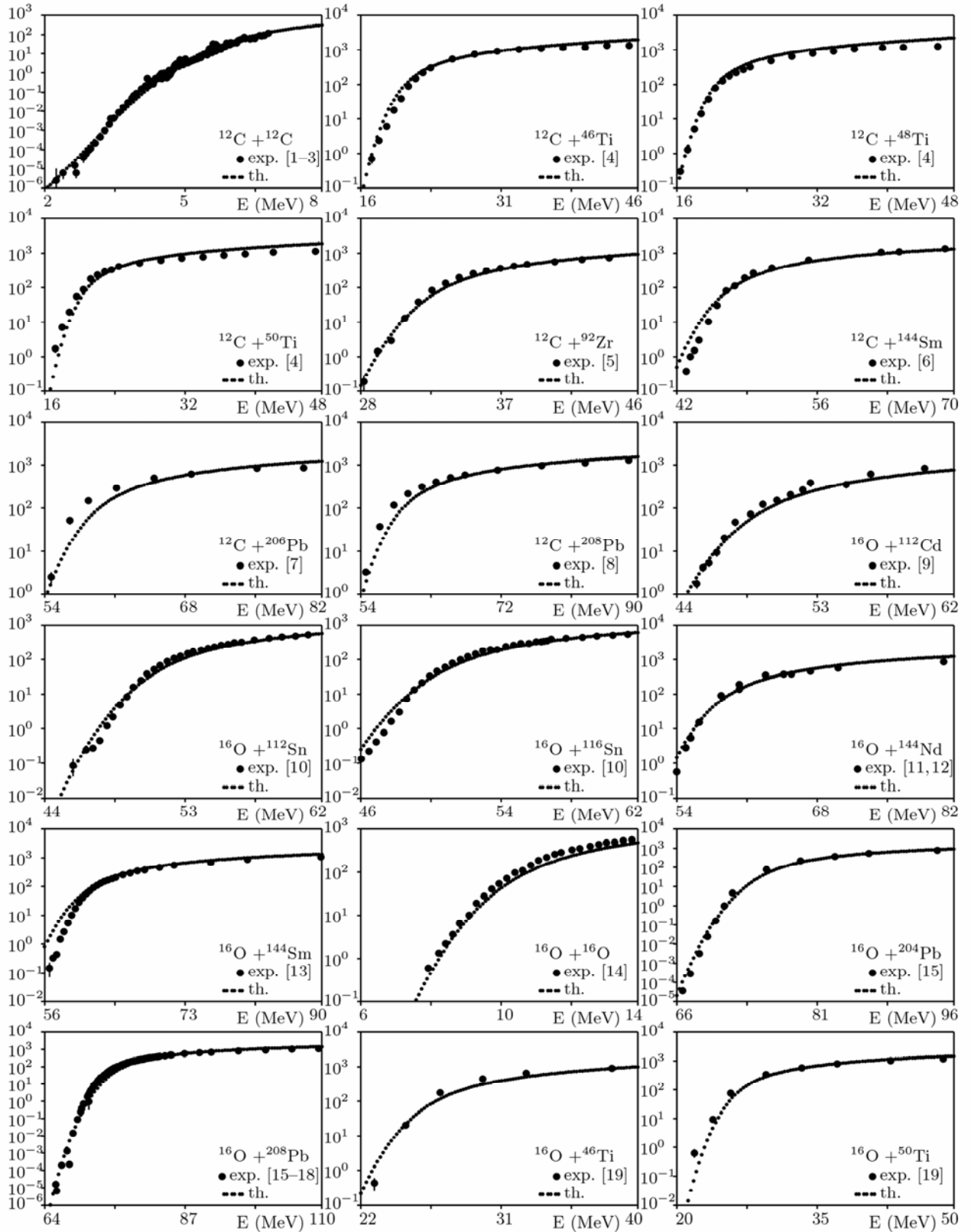


Fig. 1. The energy dependence of the heavy-ion fusion cross section around barrier.  $Y$ -axis in panels shows the fusion section in mb.

1. A. V. Karpov, et al., NIM A859 (2017) 112 (<http://nrv.jinr.ru/nrv/webnrv/fusion/reactions.php>).
2. C. Y. Wong, Phys. Rev. Lett. 31 (1973) 766.
3. V. Yu. Denisov, I. Yu. Sedykh, Eur. Phys. J. A 55 (2019) 152.

**FISSION OF SUPER-HEAVY ELEMENTS:  
<sup>132</sup>SN – PLUS – THE – REST, OR <sup>208</sup>Pb – PLUS – THE – REST ?**

**F.A. Ivanyuk<sup>1</sup>, M.D. Usang<sup>2</sup>, C. Ishizuka<sup>2</sup>, and S. Chiba<sup>2</sup>**

<sup>1</sup>*Institute for Nuclear Research of NAS of Ukraine, Kyiv, Ukraine*

<sup>2</sup>*Tokyo Institute of Technology, Tokyo, Japan*

The physics of super-heavy elements (SHE) has a long history. With the development of experimental facility it became possible not only fix the fact of formation of SHE, but accumulate so many super-heavy nuclei that it turned out possible to examine their properties. In the experiment of Itkis group [1,2] the nucleus <sup>132</sup>Sn was found out as the light fragment of all investigated nuclei. The theoretical calculation within the scission point model [3] also predict <sup>132</sup>Sn (or slightly heavier) as the most probably light fragment for fission of SHE. At the same time there are few very recent publications where formation of heavy fragment close to <sup>208</sup>Pb is predicted as a main fission mode. In [4] the heavy fragment close to <sup>208</sup>Pb was obtained in the super-heavy region, 106<Z<114.

In order to solve this contradiction and make it clear what kind of fission fragment mass distribution (FFMD) one could expect in the fission of SHEs, we have carried out the calculations of FFMD for a number of SHEs within the four-dimensional Langevin approach.

For this we have solved the system of first order differential equations (Langevin equations, see [5]) for the time dependence of collective variables  $q_\mu$  and the conjugated momenta  $p_\mu$ ,

$$\begin{aligned} dq_\mu / dt &= (m^{-1})_{\mu\nu} p_\nu, \\ dp_\mu / dt &= -\partial F(q, T) / \partial q_\mu - (1/2) \partial (m^{-1})_{\nu\sigma} / \partial q_\mu p_\nu p_\sigma - \gamma_{\mu\nu} (m^{-1})_{\nu\sigma} p_\sigma - g_{\mu\nu} R_\nu(t), \end{aligned} \quad (1)$$

where the sums over the repeated indices are assumed. In Eqs. (1) the  $F(q, T)$  is the temperature dependent free energy of the system, and  $\gamma_{\mu\nu}$  and  $(m^{-1})_{\mu\nu}$  are the friction and inverse of mass tensors,  $g_{\mu\nu} R(t)$  is the random force. The free energy  $F(q, T)$  was calculated as the sum of liquid drop deformation energy and the temperature dependent shell correction  $\delta F(q, T)$ . The collective inertia tensor  $m_{\mu\nu}$  was calculated within the Werner-Wheeler approximation and for the friction tensor  $\gamma_{\mu\nu}$  we used the wall-and-window formula. The random force  $g_{\mu\nu} R(t)$  is the product of white noise  $R(t)$  and the temperature dependent strength factor  $g_{\mu\nu}$ . The factor  $g_{\mu\nu}$  is related to the temperature and friction tensor via the modified Einstein relation,

$$g_{\mu\sigma} g_{\sigma\nu} = T^* \gamma_{\mu\nu}, \quad \text{with } T^* = (\hbar\omega/2) \coth(\hbar\omega/2T) \quad (2)$$

Parameter  $\omega$  is the local frequency of collective motion. The minimum of  $T^*$  is given by  $\hbar\omega/2$ . The temperature  $T$  here is related to the reaction energy the internal excitation energy  $E^*$  by,

$$E^* = E_{gs} + E_x - E_{kin} - V_{pot}(q, T=0) = aT^2, \quad (3)$$

where  $E_{gs}$  is the ground state energy of fissioning nucleus,  $V_{pot}$  – the potential energy, and  $a$  is the level density parameter.

Initially, the momenta  $p_\mu$  are set to zero, and calculations are started from the ground state deformation. Such calculations are continued until the trajectories reach the "scission point", which was defined as the

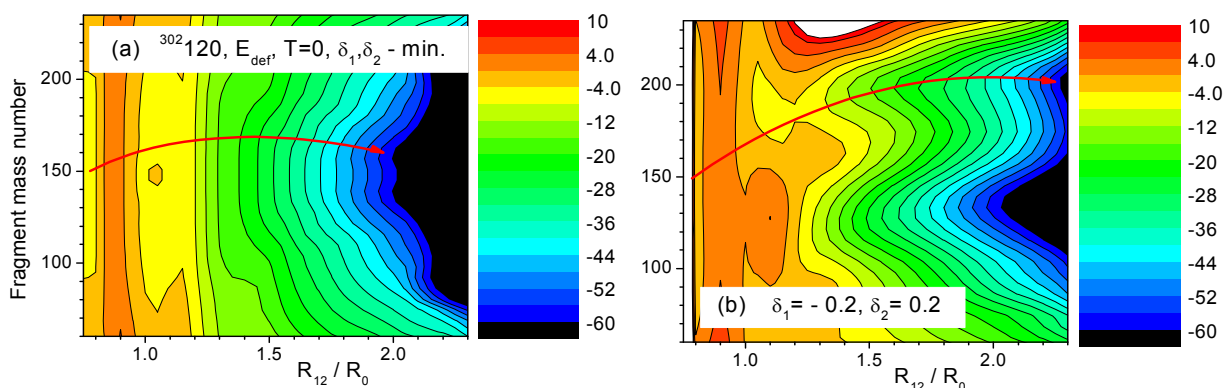


Fig. 1. (a) The potential energy of  $^{302}120$  at  $T=0$  minimized with respect to deformation parameters  $\delta_1$  and  $\delta_2$ .

(b) The potential energy of  $^{302}120$  at  $T=0$  at fixed values of  $\delta_1=-0.2$  and  $\delta_2=0.2$ .

point in deformation space where the neck radius attains the value  $r_{\text{neck}}=1$  fm.

At first we have looked at the potential energy of fissioning nuclei. Fig. 1 shows the potential energy  $E_{\text{def}}$  of nucleus with  $Z=120$  and  $A=302$  at zero temperature as function of the elongation (the distance  $R_{12}$  between the left and right parts of nucleus) and mass asymmetry. In Fig. 2(a) the energy was minimized with respect to the parameters of deformation of left and right fragments  $\delta_1$  and  $\delta_2$ .

One clearly sees the bottom of potential energy leading to almost symmetric mass splitting. There is also a hint on the mass asymmetric valley at  $A_F$  close to  $A_F=208$ . If the trajectories would follow the bottom of potential energy then the mass FFMD of  $^{302}120$  would be mass symmetric. However it is well known that due to dynamical effects the trajectories may deviate substantially from the bottom of potential valley. We calculate the trajectories in four-dimensional deformation space. In this space there could be the local minima leading away from the bottom of potential valley. An example is shown in Fig. 2(b). Here we show the potential energy for fixed  $\delta_1=-0.2$  and  $\delta_2=0.2$ . One can see that in this subspace the trajectories can easily be trapped in the higher in energy valley leading to highly asymmetric fission. The trajectories can not skip into deeper symmetric valley because of barrier between these two valleys. In this way the strongly mass asymmetric peak appears in the mass distribution of fission fragments.

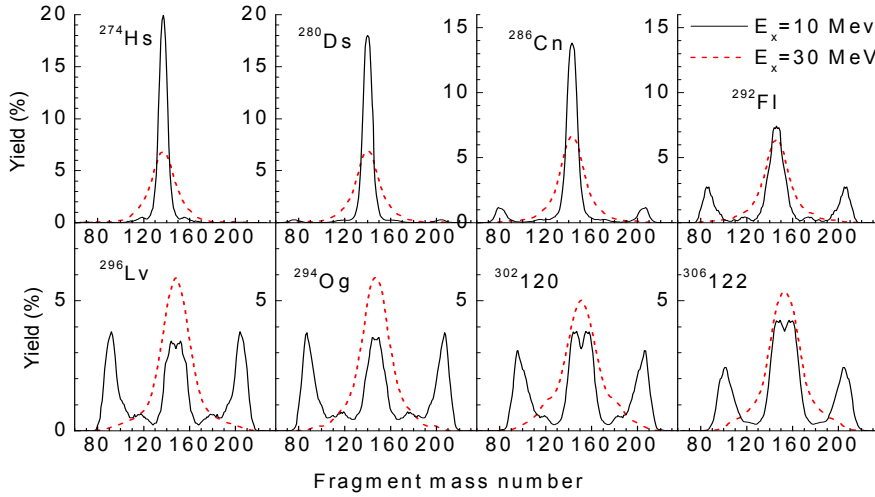


Fig. 2. The fission fragment mass distributions of super-heavy nuclei from  $^{274}\text{Hs}$  to  $^{306}122$  calculated for the excitation energy  $E_x=10$  MeV (black curves) and  $E_x=30$  MeV (red).

In Fig. 2 we show the fission fragment mass distributions of super-heavy nuclei from  $^{274}\text{Hs}$  to  $^{306}122$  as the function of fragment mass number. As one can see, at the excitation energy  $E_x=30$  MeV the shell structure is washed out and all considered here nuclei fission symmetrically. At  $E_x=10$  MeV the lighter superheavies Hs and Ds also undergo mass symmetric fission. The mass distributions of nuclei from  $^{286}\text{Cn}$  to  $^{306}122$  have three or four peak structure. Obviously, the multi-peak structure of SHEs is the result of the shell effects, which at  $E_x=10$  MeV are still large. One can also see the strongly asymmetric peak at the mass number close to  $A_F=208$ . The strength of the (almost) symmetric and asymmetric components in FFMD of SHEs depends on the proton and neutron numbers of the compound nucleus. For  $^{286}\text{Cn}$  the contribution of strongly asymmetric peak is very small. This contribution becomes larger for more heavy SHEs. In the element  $^{306}122$  the symmetric and mass asymmetric peaks are of the same magnitude. So, the answer to the question: ``Fission of super-heavy elements:  $^{132}\text{Sn}$ -plus-the-rest, or  $^{208}\text{Pb}$ -plus-the-rest? `` is: BOTH.

In fission process of super-heavy nuclei one would observe both, the fragment with the mass number close to  $^{132}\text{Sn}$ ,  $A_F \approx 140$  plus the rest, and almost spherical fragment with the mass number  $A_F \approx 208$  plus the rest. More details are given in [6].

- [1] M. G. Itkis, A. A. Bogatchev, I. M. Itkis, et al., J. Nucl. Rad. Sci. 3 (2002) 57.  
 [2] M. G. Itkis, E. Vardaci, I. M. Itkis, G. N. Knyazheva, et al, Nucl. Phys. A 944 (2015) 204.  
 [3] N. Carjan, F. A. Ivanyuk, and Yu. Ts. Oganessian, Phys. Rev. C 99 (2019) 064606.  
 [4] M. Albertsson, B. G. Carlsson, T. Dossing, et al, Eur. Phys. J. A 56 (2020) 46 [  
 [5] Y. Abe, S. Ayik, P.-G. Reinhard, and E. Suraud, Phys. Rep. 275, (1996) 49.  
 [6] C. Ishizuka, X. Zhang, M. D. Usang, F. A. Ivanyuk, and S. Chiba, Phys. Rev. C 101 (2020) 011601(R).

**SHELL AND COLLECTIVE EFFECTS  
 IN THE LEVEL DENSITY WITHIN A MICRO-MACROSCOPIC APPROACH**

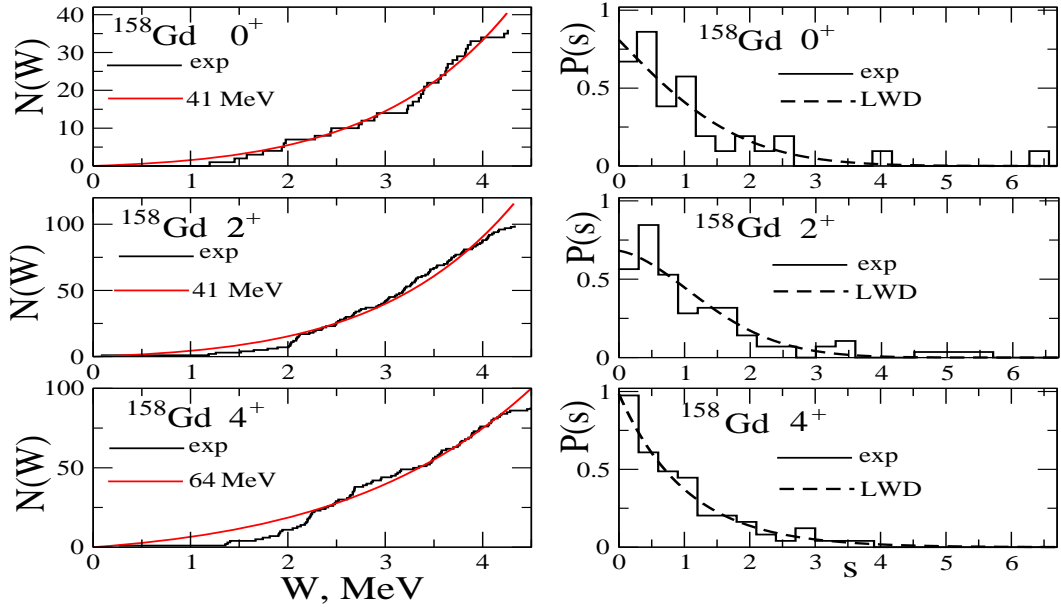
**A.G. Magner<sup>(1)</sup>, A.I. Sanzhur<sup>(1)</sup>, S.N. Fedotkin<sup>(1)</sup>, A.I. Levon<sup>(1)</sup>, and S. Shlomo<sup>(2)</sup>**

<sup>1)</sup>*Institute for Nuclear Research of the NAN Ukraine, Kyiv, Ukraine*

<sup>2)</sup>*Cyclotron Institute, Texas A&M University, College Station, Texas, 77843, USA*

Many nuclear properties can be described in terms of the statistical level density. We derived the nuclear level density in the micro-macroscopic approximation (MMA) beyond the saddle-point method (SPM),  $\rho \propto I_\nu(S)/S^\nu$ , where  $I_\nu(S)$  is the modified Bessel function of the entropy  $S$  of order  $\nu = (n+1)/2$ , where  $n$  is the number of integrals of motion. This level density goes to the well-known SPM grand-canonical ensemble limit  $\rho \propto \exp(S)$  for large entropy  $S$  and to the finite micro-canonical limit at low excitation energy. Including shell effects in the semiclassical level density parameter  $K = A/a$ , as function of the particle number  $A=N+Z$ , where  $N$  and  $Z$  are the neutron and proton numbers in nucleus, respectively, *leads to fairly good agreement with experimental data for the neutron resonances.*

The MMA expressions for the one-parametric cumulative level density,  $N = \int dW' \rho(W')$ , where the integral is taken from 0 to the excitation energy  $W$ , provides a good fit, using the standard mean-least-square (MLS) code, to the experimental two-neutron-transfer reaction data (left panels of the figure) for  $K$  values shown for different angular momenta  $I^\pi = 0^+, 2^+$  and  $4^+$ . The  $N(W)$  is used for the unfolding procedure by transferring the spectrum  $W_i$  to the uniform states  $w_i = \tilde{N}(W_i)$ , where the tilde means averaging over states  $i$ , and determining  $s_i = w_{i+1} - w_i$ . Using this result in the statistical analysis of the collective excitation states  $i$  in terms of the nearest neighbor spacing distribution  $P(s)$  (NNSD) we obtained the experimental NNSD (right panels of figure). From a good MLS fit to our one-parameter theoretical linear-repulsion-density NNSD within the Wigner-Dyson theory for  $^{158}\text{Gd}$ , as example, one finds the parameters of contributions of the Wigner chaos and Poisson order distributions for different angular momenta  $I^+$ . As seen from these plots, with increasing  $I^+$  there is an anomaly



behavior of the NNSD  $P(s)$  as a shift from the Poisson order with a sharp peak at zero spacing  $s$  to the side of the Wigner chaos distribution with the maximum at  $s > 0$  for the angular momentum  $2^+$  and, then, again for  $4^+$  to the Poisson order, in contrast of a monotonical  $I^+$  dependence found for the collective states in actinide nuclei. For perspectives, the moment of inertia for the collective rotational bands and K-symmetry breaking phenomenon is a challenge for study.

[1] A.I. Levon et al, *Phys. Rev. C* **97**, 044305 (2018); **C 100**, 034307 (2019).

[2] A.G. Magner, A.I. Levon, S.V. Radionov, *Eur. Phys. J.* **54**, 214 (2018).

## INVESTIGATION OF QUARK MATTER IN NUCLEI IN SCATTERING OF PROTONS OFF THEM BY MEANS OF ANALYSIS OF BREMSSTRAHLUNG PHOTONS

S. P. Maydanyuk

<sup>1</sup> *Institute for Nuclear Research NAN of Ukraine*

Bremsstrahlung photons is a powerful tool for the experimental study of the distribution of electromagnetic matter. According to the fundamental principles of quantum electrodynamics, the assumption that a proton (interacting with nucleus) contains a non-point-like distribution of electric charge and magnetic moment can be verified, in principle. Another motivation for the study is to explain the anomalous magnetic moment of a proton when it interacts with the nucleus.

We study emission of bremsstrahlung photons during proton scattering off light, middle and heavy nuclei at proton-beam energies ranging from zero to 1 GeV. A main focus of research is to try to see the internal structure of nucleons inside nucleus-target and the scattered proton in the bremsstrahlung spectra basing on our new model in the energy range from zero to intermediate. The report will present the results of our first such research.

The formalism of the new approach is based on the combination of the theory of deep inelastic collisions (DIS) [1] and our previously developed theory of bremsstrahlung emission in nuclear physics applied for proton-nucleus scattering [2]. In such a formalism, the bremsstrahlung spectra are sensitive to parameter  $Q^2$  of virtual photons (such photons are quanta of exchange of electromagnetic interaction between the scattered proton and one nucleon of the nucleus-target). This parameter is related to the distribution of electromagnetic charge in the scattered proton (see Fig. 1). A feature of this study is the inclusion of incoherent emission to the analysis, which was not done in our first work [3] and it is important.

In the paper, we present our first estimates of the bremsstrahlung emission in proton scattering on  $^{12}\text{Be}$ ,  $^{42,44,48}\text{Ca}$ ,  $^{54}\text{Fe}$ ,  $^{208}\text{Pb}$  nuclei (the most accurate experimental measurement for proton-nucleus scattering was

obtained for these nuclei, but without proton structure study).

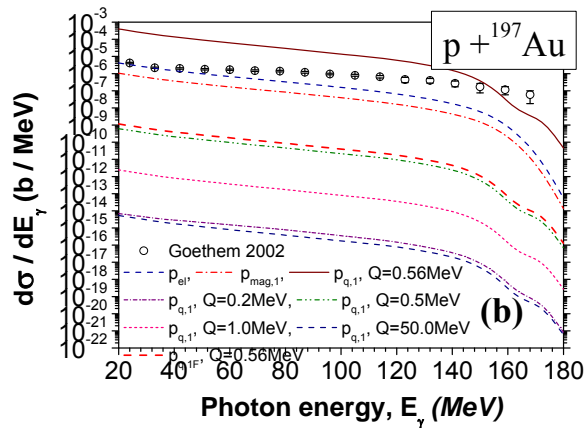


Fig.1. Spectra of bremsstrahlung photons after inclusion of internal structure of the scattered proton off nuclei  $^{197}\text{Au}$  in comparison with experimental data at energy of proton beam of 180 MeV.

1. W. Greiner, E. Stein, S. Schramm, *Quantum chromodynamics* (Springer, Second ed., 2002).
2. S. P. Maydanyuk, Phys. Rev. **C86**, 014618 (2012). S. P. Maydanyuk and P.-M. Zhang, Phys. Rev. **C91**, 024605 (2015).
3. S. P. Maydanyuk, P.-M. Zhang, L.-P. Zou, Phys. Rev. **C99**, 064602 (2019).

## CALCULATION OF THE CROSS-SECTIONS OF SUB-BARRIER FUSION AND ELASTIC SCATTERING OF HEAVY IONS IN THE FRAMEWORK OF THE MODIFIED THOMAS-FERMI APPROACH WITH THE SKYRME FORCE

**B. A. Nesterov, O. I. Davydovska, V. Yu. Denisov**

*Institute for Nuclear Research, National Academy of Sciences of Ukraine, Kyiv*

The potentials of nucleus-nucleus interaction are calculated within the extended Thomas-Fermi method for the  $^{16}\text{O} + ^{56}\text{Fe}$  and  $^{40}\text{Ca} + ^{40}\text{Ca}$  systems [1]. We take into account all terms up to terms of the second order in  $\hbar$  of the quasiclassical decomposition of kinetic energy [1-5]. The density-dependent Skyrme force is used as nucleon-nucleon interactions [1-5]. The nucleon densities of nuclei are obtained in the framework of the Hartree-Fock model with the Skyrme force and the BCS approximation for the nucleon pairing. We used the Skyrme force parameterization SkM\* for the calculation of both the potentials of nucleus-nucleus interaction and the nucleon densities. Note that the modified Thomas-Fermi approximation and Hartree-Fock-BCS theory with Skyrme forces well describe the binding energy of the nuclei, nucleon density distributions, root-mean-square radii and many other characteristics of the ground and excited states of nuclei.

The potentials were calculated in the approximation of "frozen densities", which can be applied at the collision energies around the barrier. This approximation makes it possible to study in detail the properties of nucleus-nucleus interaction around the point of contact of the nuclei.

Using the obtained potentials, the cross-sections of subbarrier nuclear fusion for the  $^{16}\text{O} + ^{56}\text{Fe}$  and  $^{40}\text{Ca} + ^{40}\text{Ca}$  systems were calculated. To calculate the cross sections, we used the CCFULL code, which take into account the coupling of channels with the low-lying multipole vibrating surface excitations in both nuclei. The nuclear part of the "frozen densities" nucleus-nucleus interaction potential is approximated by the Woods-Saxon potential around barrier distances (see Fig. 1). The CCFULL code also takes into account nonlinear effects of connection with the multiphonon multipole surface excitations. The excitation parameters  $2^+$  and  $3^-$  that are required to calculate the cross section using CCFULL were taken from the corresponding compilations of the experimental data. The cross-sections of subbarrier nuclear fusion, obtained using CCFULL, are satisfactory described the experimental data.

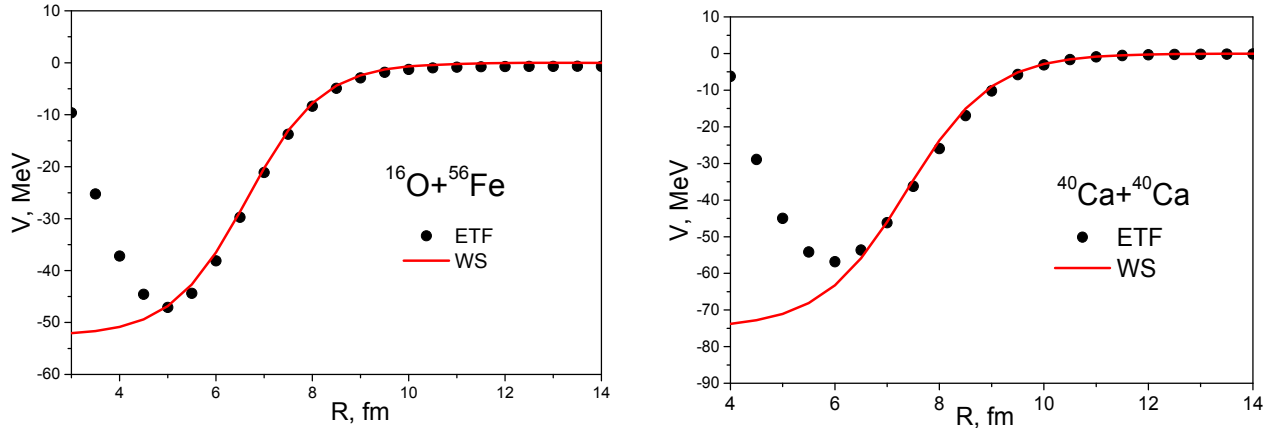


Fig. 1. The nuclear parts of the interaction potentials for the  $^{16}\text{O} + ^{56}\text{Fe}$  and  $^{40}\text{Ca} + ^{40}\text{Ca}$  systems evaluated in the extended Thomas–Fermi approximation (ETF), and its approximation by the Woods–Saxon potentials (WS).

Using the obtained Woods-Saxon potentials for the real part of the interaction, the cross sections of elastic scattering for  $^{16}\text{O} + ^{56}\text{Fe}$  and  $^{40}\text{Ca} + ^{40}\text{Ca}$  systems were obtained within the optical model. The results of the calculations of the elastic scattering cross sections for the system  $^{16}\text{O} + ^{56}\text{Fe}$  at the beam energy  $E_{lab} = 44$  MeV and for the system  $^{40}\text{Ca} + ^{40}\text{Ca}$  at the beam energy  $E_{cm} = 71.8$  MeV are presented in Fig. 3. As can be seen from the figure, the obtained cross sections of elastic scattering are in good agreement with the experimental data.

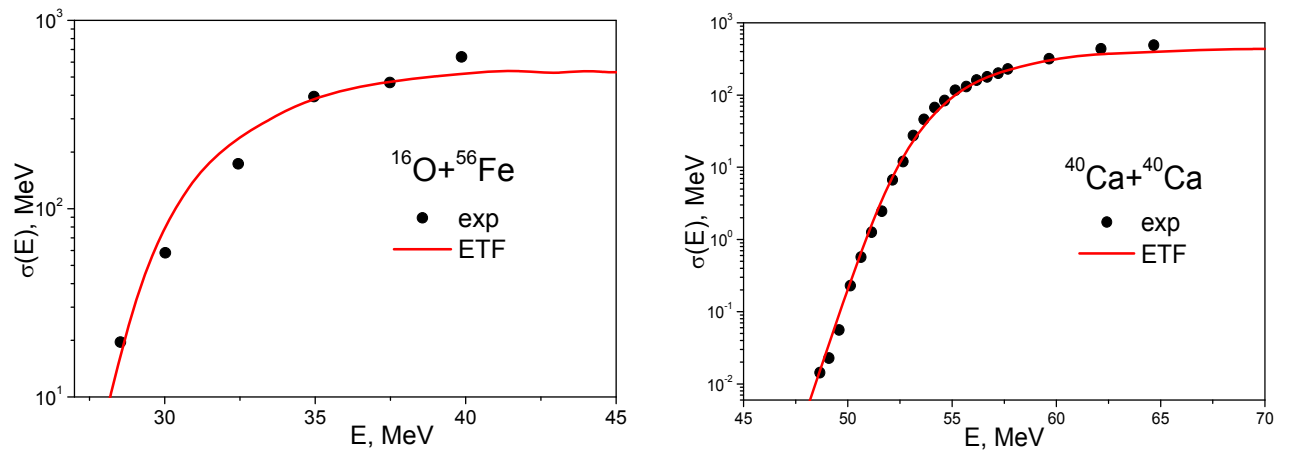


Fig. 3. The cross-sections of subbarrier nuclear fusion for the  $^{16}\text{O} + ^{56}\text{Fe}$  and  $^{40}\text{Ca} + ^{40}\text{Ca}$  systems obtained for the potentials evaluated in the extended Thomas–Fermi approximation (ETF).

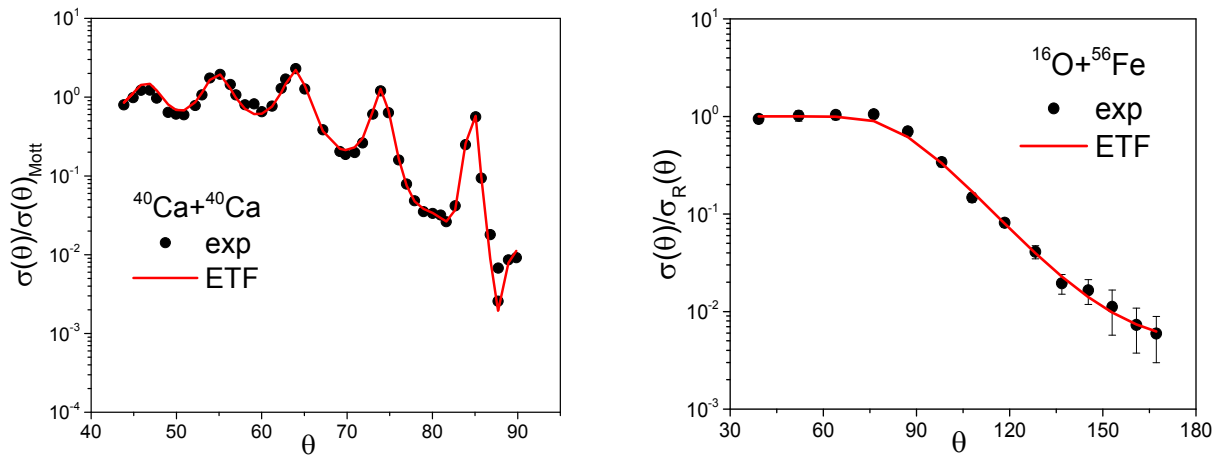


Fig. 4. The cross sections of elastic scattering for the  $^{16}\text{O} + ^{56}\text{Fe}$  and  $^{40}\text{Ca} + ^{40}\text{Ca}$  systems obtained for the potentials evaluated in the extended Thomas–Fermi approximation (ETF).

Thus, the nucleus-nucleus potentials for the  $^{16}\text{O} + ^{56}\text{Fe}$  and  $^{40}\text{Ca} + ^{40}\text{Ca}$  reactions were calculated within the extended Thomas-Fermi method. Using the obtained potentials, it was calculated the cross-sections of subbarrier nuclear fusion and elastic scattering, which in a good agreement with the experimental data.

1. V.O. Nesterov, O.I. Davidovskaya, V.Yu. Denisov. J. Nucl. Phys. Energ. 20, № 4 (2019) 349 (in Ukrainian).
2. O.I. Davidovskaya, V.Yu. Denisov, V.O. Nesterov. Ukr. J. Phys. 62, N6 (2017) 473.
3. O.I. Davidovskaya, V.Yu. Denisov, V.O. Nesterov. J. Nucl. Phys. Energ. 19, № 3 (2018) 203 (in Ukrainian).
4. O.I. Davydovska, V.Yu. Denisov, V.A. Nesterov. Nucl. Phys. A 989 (2019) 214.
5. O.I. Davidovskaya, V.Yu. Denisov, V.O. Nesterov. J. Nucl. Phys. Energ. 11, No. 1 (2010) 25 (in Ukrainian).

## COMPUTER MODELING OF PRODUCTION CROSS SECTIONS FOR BEYOND SM PARTICLES

**T. V. Obikhod, I. A. Petrenko**

*Institute for Nuclear Research, National Academy of Sciences of Ukraine, Kyiv, Ukraine*

We have considered the following processes:

- Di-jet processes;
- CP-odd A boson production process;
- Higgs boson production process in association with pair of top quarks;
- DM production processes.

These processes play the fundamental role for the searches of physics beyond the SM. With the help of computer program MCFM v.9.0 we have calculated differential production cross sections for invariant mass distribution and cinematic properties of the decay products at energy of 14 TeV. From the analysis of our results we made the following conclusions:

- the absence of a clear dependence on the Sudakov EW corrections both in the distribution in the invariant mass and in the momenta, but the need to take into account the angular distribution for the di-jet process;
- the largest values of momentum and angular differential production cross sections for A boson are for the decay into b quarks compared to decay into tau leptons for  $p_T > 80\text{GeV}$ . Thus the observation that A

boson prefers to decay into heavier particles is confirmed;

- complex decay chain of the Htt process, connected with leptonically decays of top quark and hadronically decays of anti-top quark is characterized by lower value of differential production cross section compared to the 640 process without any decays of Htt particles. Decay products of 640 process are oriented perpendicular to collision axis;

- momentum distribution for differential production cross section of DM mediators shows the maximal value at about 100 GeV and complete kinematic information indicates about the mass region of Scalar Mediator of about 200-400 GeV. The formation of this DM mediator is accompanied by high-energy jets in the direction perpendicular to the axis of collision. Our calculations for three processes of formation of DM mediators shows the predominance of the process with Gluonic DM operator and the absence of a clear resonance.

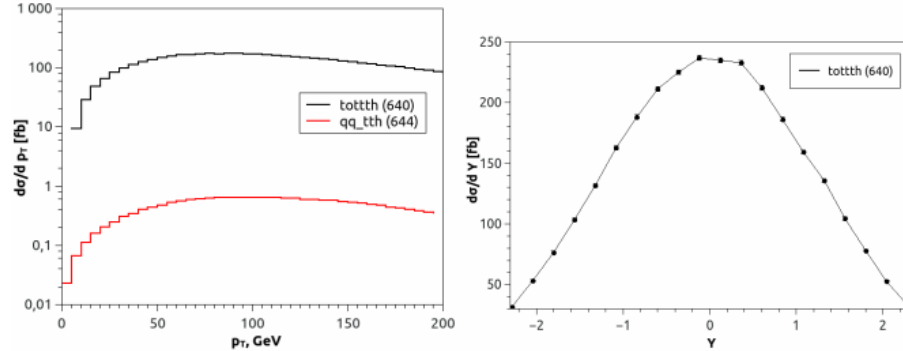


Fig. 1. Differential production cross sections with respect to: (left) - Higgs boson transverse momentum; (right) Higgs boson rapidity.

1. T.V. Obikhod, I.O. Petrenko. "Computer modeling of production cross sections for beyond SM particles," arXiv:2001.08648v1 [hep-ph] 8 Jan 2020.
2. P. J. Fox and C. Williams, "Next-to-leading order predictions for dark matter production at hadron colliders," Phys. Rev. D, vol. 87, p. 054030, Mar 2013.
3. J. M. Campbell, D. Wackerth, and J. Zhou, "Study of weak corrections to drell-yan, top-quark pair, and dijet production at high energies with MCFM," Phys. Rev. D, vol. 94, p. 093009, Nov 2016.

## INVESTIGATIONS OF ELECTROWEAK SYMMETRY BREAKING MECHANISM FOR HIGGS BOSON DECAYS INTO FOUR FERMIONS

**T. V. Obikhod, I. A. Petrenko**

*Institute for Nuclear Research, National Academy of Sciences of Ukraine, Kyiv, Ukraine*

The discovery in 2012 of the Higgs boson and the subsequent studies of its properties put its compatibility with the Standard Model (SM). However, as the SM Higgs boson is a scalar particle, it has sensitivity to possible new physics scales. So there are the arguments for expecting new physics, called supersymmetry (SUSY).

Models with extended Higgs boson sectors are of prime importance for investigating the mechanism of electroweak (EW) symmetry breaking for Higgs decays into four fermions and for Higgs-production in association with a vector bosons (VBF). In the framework of the Two-Higgs-Doublet Model (THDM) [1] using two scenarios obtained from the experimental measurements we presented next-to-leading-order results on the four-fermion decays of light CP-even Higgs boson,  $h \rightarrow 4f$ . With the help of Monte Carlo program Prophecy 4f 3.0 [2], we calculated the values  $\Gamma = \Gamma_{EW} / (\Gamma_{EW} + \Gamma_{SM})$  and  $\Gamma = \Gamma_{EW} + \Gamma_{QCD} / (\Gamma_{EW} + \Gamma_{QCD} + \Gamma_{SM})$  for Higgs boson decay channels  $H \rightarrow \nu_\mu \text{ anti-}\nu_e, \mu \text{ anti-}\mu e \text{ anti-}e, eeee, \mu\mu ee$ . We didn't find significant difference when accounting QCD corrections to EW processes in the decay modes of Higgs boson.

Using computer programs Pythia 8.2 and Softsusy [3] we calculated the following values:

$\sigma(ff \rightarrow H)BR(H \rightarrow ZZ)$  and  $\sigma(ff \rightarrow H)BR(H \rightarrow WW)$  for VBF processes and  $\sigma(ggH)BR(H \rightarrow WW)$  via  $t$   $\bar{t}$  fusion process at 13 and 14 TeV for understanding the nature of the deviation from SM of experimental data [4,5] and for further investigations of SUSY processes at the LHC. We concluded that the essential contribution to the computation is made by the magnitude of the BR compared to the production cross section one.

4. Ansgar Denner, Stefan Dittmaier, Jean-Nicolas Lang, Renormalization of mixing angles, arXiv:1808.03466 [hep-ph].
5. Ansgar Denner, Stefan Dittmaier, Alexander Mück, PROPHECY4F 3.0: A Monte Carlo program for Higgs-boson decays into four-fermion final states in and beyond the Standard Model, arXiv:1912.02010 [hep-ph].
6. Torbjörn Sjöstrand et al., An Introduction to PYTHIA 8.2, Comput. Phys. Commun. 191 (2015) 159; B. C. Allanach et al., The Inclusion of Two-Loop SUSYQCD Corrections to Gluino and Squark Pole Masses in the Minimal and Next-to-Minimal Supersymmetric Standard Model: SOFTSUSY3.7, Comput. Phys. Commun. 219 (2017) 339, arXiv:1601.06657.
4. The ATLAS Collaboration, Measurements of the Higgs boson production fiducial and differential cross sections in the 4l decay channel at  $\sqrt{s} = 13$  TeV with the ATLAS detector, ATLAS-CONF-2018-018.
5. The ATLAS Collaboration, Measurements of gluon–gluon fusion and vector-boson fusion Higgs boson production cross-sections in the  $H \rightarrow WW \rightarrow e\nu\mu\nu$  decay channel in pp collisions at  $\sqrt{s} = 13$  TeV with the ATLAS detector, Phys. Lett. B 789 (2019) 508.

## SHAPE OF FISSION BARRIER AND NON-MARKOVIAN FISSION DYNAMICS

*S. V. Radionov*

*Institute for Nuclear Research of National Academy of Sciences of Ukraine*

Within the non-Markovian Langevin approach to nuclear fission dynamics,

$$M\ddot{q} = -\frac{\partial E_{pot}}{\partial q} - \kappa_0 \int_0^t \exp\left(-\frac{|t-t'|}{\tau}\right) \dot{q}(t') dt' - \zeta(t) \quad (1)$$

the fission width has been investigated as a function of a shape of nuclear potential barrier  $E_{pot}$ . The possible shapes of  $E_{pot}$  have been chosen in terms of two jointly connected parabolas and seventh-order polynomial in collective coordinate  $q$  function. I have found that the value of fission width calculated for symmetric fission of  $^{236}\text{U}$  at high excitation energies significantly depends on internal structure of the fission potential barrier, see Fig. 1. It has also be found that such a dependence diminishes with the size  $\tau$  of memory effects in nuclear fission dynamics (1).

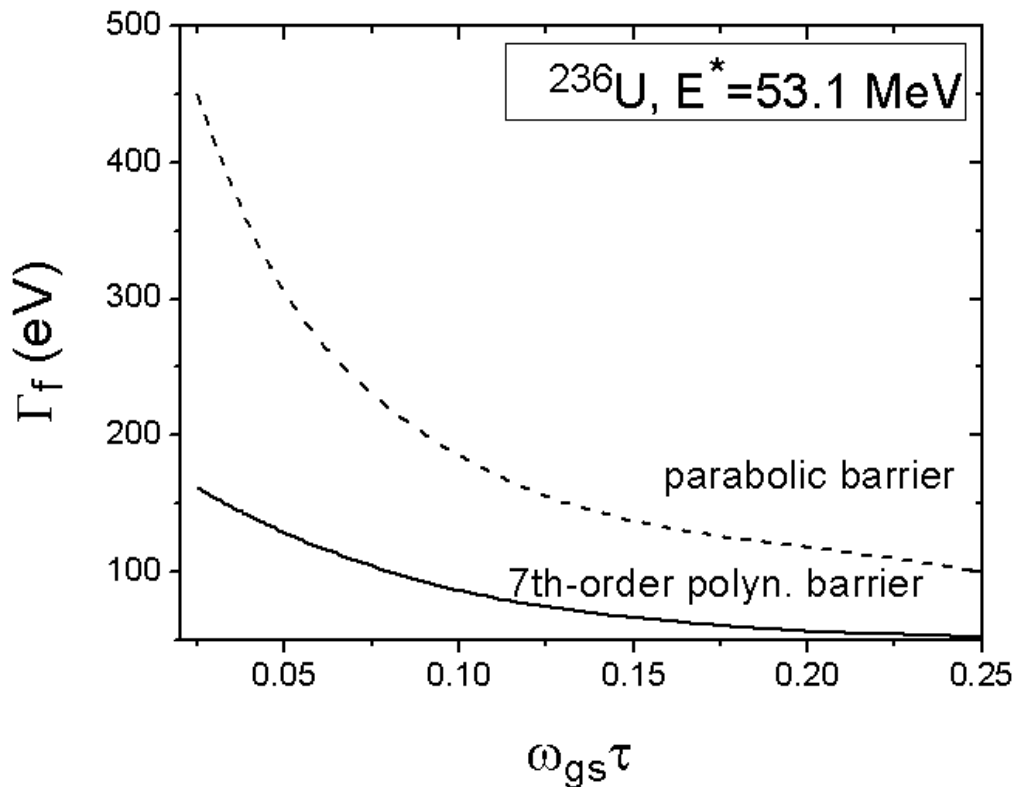


Fig. 1: Fission width of symmetric fission of  $^{236}\text{U}$  at initial excitation energy of 53.1 MeV as a function of the size  $\tau$  of memory effects at the non-Markovian fission dynamics (1). Different curves on the Figure correspond to different shapes of the nuclear potential barrier  $E_{pot}$  in (1).

## FLUCTUATIONS OF PARTICLE NUMBERS NEAR THE CRITICAL POINT OF NUCLEAR MATTER

S. N. Fedotkin, A. G. Magner, A. I. Sanzhur, U. V. Grygoriev

*Institute for Nuclear Research, National Academy of Sciences of Ukraine, Kyiv, Ukraine*

Equation of state with quantum statistics corrections was derived for gas of particles interacting through the repulsive and attractive van der Waals (vdW) forces up to the first order of small parameter  $\delta(T, n)$ ,

$$\delta(T, n) = \frac{\hbar^3 \pi^{3/2}}{2g(mT)^{3/2}} \frac{n}{(1-nb)}, \quad (1)$$

where  $n$  and  $T$  are, respectively, the particle number density and temperature of the system,  $m$  and  $g$  are the particle mass and degeneracy factor. The parameter  $b$  accounts for the vdW excluded volume of particles. The relative fluctuation of particle number  $\omega$  is given by

$$\omega(T, n) = \frac{\langle (\Delta N)^2 \rangle}{\langle N \rangle} = \frac{T(\partial n / \partial \mu)_T}{n}, \quad (2)$$

where  $\mu$  is the chemical potential and  $\chi = (\partial n / \partial \mu)_T$  is the isothermal susceptibility. Near the critical point  $n_c$  and  $T_c$ , the particle numbers fluctuations  $\omega(T, n)$  (2) for a fixed particle number density  $n = n_c$ , when they are valid, can be evaluated by

$$\omega(T_c(1+\tau), n_c) \approx \frac{T_c n_c}{P_c} G \tau^{-1}, \quad (3)$$

where

$$G = \left( \frac{P_c}{T_c n_c} \right) \frac{(1-n_c b)^2}{1 - \delta(T_c, n_c)}, \quad (4)$$

and the value of  $\tau$  indicates the distance from the critical temperature

$$\tau = \frac{T - T_c}{T_c}.$$

These approximate analytical results for  $\omega(T, n)$  (3) are in good agreement with the exact numerical calculations for interacting system of Fermi nucleons ( $g = 4$ ) [2]. However, these fluctuations  $\omega$  near the critical temperature  $T_c$  at the particle density  $n_c$  are divergent in the limit  $T \rightarrow T_c$ , in contrast to the assumption of small relative particle numbers fluctuations as compared to the corresponding statistically averaged quantity.

Relationships which lead to the restrictions to a temperature vicinity of the critical temperature  $T_c$ , where (3) is valid, for the phase transition in a medium were obtained in [3]:

$$\frac{T - T_c}{T_c} > \left( \frac{\bar{r}}{r_{corr}} \right)^6.$$

Here  $\bar{r}$  and  $r_{corr}$  are the mean interparticle distance and correlation length of the two-body interaction. The value of  $\tau$  for the considered system of nucleons is found preliminarily about 10%. More accurate evaluations of finite fluctuations  $\omega$  near the critical point can be obtained as the dispersion of the Gaussian-like Gibbs probability distribution.

4. S.N. Fedotkin, A.G. Magner, M.I. Gorenstein. Phys. Rev. C, **100**, 054334 (2019).
5. R.V.Poberezhnyuk, V.Vovchenko, D.Anchishkin, M.I. Gorenstein. Int. J. Mod.Phys. E26(2017) 1750061.
6. V.G.Vaks, A.I. Larkin, S.A. Pikin. Sov. Phys. JETP. 24 (1967) 240.

## INVESTIGATION OF NUCLEAR PROCESSES FOR LIGHT NUCLEI IN COMPACT STARS

**K. A. Shaulskiy<sup>1</sup>, S. P. Maydanyuk<sup>2</sup>**

<sup>1</sup> Taras Shevchenko National University of Kyiv, Ukraine

<sup>2</sup> Institute for Nuclear Research, National Academy of Sciences of Ukraine

One of the most important characteristics that is a manifestation of nuclear forces is the binding energy of nucleus. In research, we make focus on analysis of this characteristic for the lightest nuclei in medium of compact star [1]. We are interesting in the following questions. Whether can nuclear forces connect nucleons as a bound nuclear system, or such nucleus is separated on individual nucleons by gravitational forces? How is this effect manifested from white dwarfs to neutron stars?

In research, we obtain a formula of binding energy for the lightest nuclei within the framework of many-nucleon theory of nucleus [2, 3], with own additional formalism of influence of polytropic star medium on the nucleus [4]. It has been found that starting from some critical distance between the nucleus under study and center of the star, this nucleus is separated on nucleons. According to the calculations, this phenomenon of so-called *nucleation dissociation* does not occur in white dwarfs (i.e., gravitational forces cannot separate nucleus in such a star). But we observe this phenomenon in neutron stars.

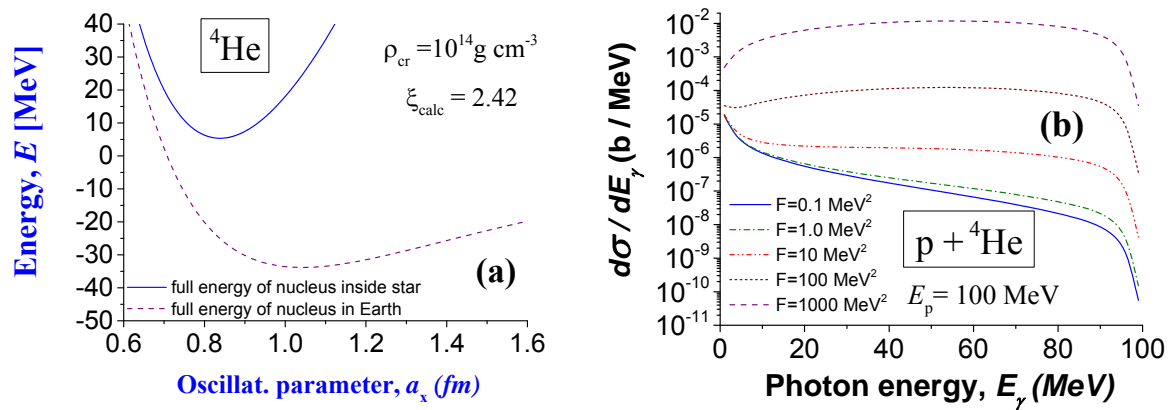


Fig. 1. Change in the binding energy of nucleus  ${}^4\text{He}$  (a) and emission of the bremsstrahlung photons in scattering of protons off  ${}^4\text{He}$  (b) on the Earth and inside compact stars (see [6], for explanations).

We determine a distance from center of neutron star, where dissociation of the lightest nuclei takes place. The first estimations of the bremsstrahlung photons, which are emitted during scattering of protons off such a nucleus, are obtained in conditions on Earth and inside environment of the compact star [see. Fig. 1].

1. А. Ю. Потехин, *Физика нейтронных звезд*, УФН **180**, 1279–1304 (2010).
2. K. Wildermuth, Y. C. Tang, *A Unified Theory of the Nucleus* (Vieweg, 1977).
3. Y. C. Tang, M. LeMere, D. R. Thompson, *Phys. Rep.* **47**, 167–223 (1978).
4. Г. С. Бисноватый-Коган, *Релятивистская астрофизика и физическая космология* (Москва, Красанд, 2011, 376 стр.).
5. А. И. Стешенко, Г. Ф. Филиппов, *Размеры и форма ядер с избытком нейтронов*, *Ядерная Физика* **14** (вып. 4), 715 (1971)].
6. S. P. Maydanyuk, K. A. Shaulskyi, *Bremsstrahlung emission from nuclear reactions in compact stars*, 16 p., arxiv:1912.12092.

## **RISKS TO THE NUCLEAR SECURITY OF NUCLEAR FACILITIES, NUCLEAR AND OTHER RADIOACTIVE MATERIALS**

**V. I. Gavryliuk, S. S. Drapey, B. V. Kaidyk, V. I. Kirischuk, V. V. Parkhomenko, O. P. Romanova, A. V. Samsonenko**

*George Kuzmycz Training Center for Physical Protection, Control and Accounting of Nuclear Material, Institute for Nuclear Research, National Academy of Sciences of Ukraine, Kyiv, Ukraine*

Risk is the potential undesirable outcome of nuclear security event, which is determined by the likelihood of such an event and its consequences, including consequences for humans, property and the environment. Risk is usually a function of three components: threat, vulnerability and consequences. Risk management is a prerequisite for prioritizing and developing appropriate nuclear security systems and measures. Threat and risk assessments enable the State to manage risks and prioritize the allocation of resources (such as human and financial) to organizations and nuclear security systems and measures.

In the case of the assessment of the vulnerability and consequences of the implementation of possible threats to nuclear facilities and other radiation hazardous sites, first of all Ukrainian nuclear power plants, everything is more or less clear - such assessments are carried out regularly according to the methodology already approved in Ukraine. The situation is more complicated with the quantitative assessment of threats. In order for such estimates to be correct, it is necessary to have as accurate as possible information about the situation in the State and all over the world. In most cases, such estimates are based on the conclusions of corresponding experts.

In this work the likelihoods of the following threats that could be implemented in Ukraine are considered:

- explosion of nuclear warheads
- explosion of improvised nuclear device
- committing a sabotage against a nuclear power plant or other radiation hazardous site of Ukraine
- theft or other unauthorized removal of an ionizing radiation source, radioactive waste
- capture of some vital places of radiation hazardous site in order to make certain requirements to the government, local authorities, administration of the facility
- information security threats to radiation hazardous sites of Ukraine

It also discusses in detail how and estimates quantitatively with which likelihoods these threats could be implemented. As a result, the likelihoods of implementation for the most threats in Ukraine are estimated to be from “extremely low” or  $<0.025$  per year (as in the case of an explosion of nuclear warheads) to “lower than the average” or  $0.25 \div 0.40$  per year (capture of some vital places of radiation hazardous site). The implementation of the information security threat to radiation hazardous sites in Ukraine has the highest (“higher than average” or  $0.60 \div 0.75$  per year) likelihood of all mentioned threats.

## **ANALYSIS OF SPATIALLY DISTRIBUTED INFORMATION IN THE DETERMINATION OF ATTRIBUTIVE SIGNS OF NUCLEAR AND OTHER RADIOACTIVE MATERIALS**

**O. Gaidar, V. Tryshyn, G. Gaidar**

*Institute for Nuclear Research, National Academy of Sciences of Ukraine, Kyiv, Ukraine*

Determining the attributive characteristics of nuclear and other radioactive materials requires the use of a wide range of measurement techniques, including spatial-distributed information: data on the surface of samples, the size of grains, their structure and color, the distribution of major and minor elements, surface contamination, etc.

Examples of metallic uranium samples, uranium ore samples and uranium ore concentrates show how to use a complex approach to the analysis of electron microscope images with energy dispersive analysis, optical metallographic microscope, camera with macro lens, allows you to determine the methods of processing the components of the studied components and their colors etc.

The scenario of a nuclear forensic study of two samples of metallic uranium was simulated (Fig. 1), which

resulted in a number of questions to be answered, in particular: what technical means were used to obtain these samples, or whether they would represent only part of a set of similar samples, whether they have common attribute characteristics that allow them to be linked.

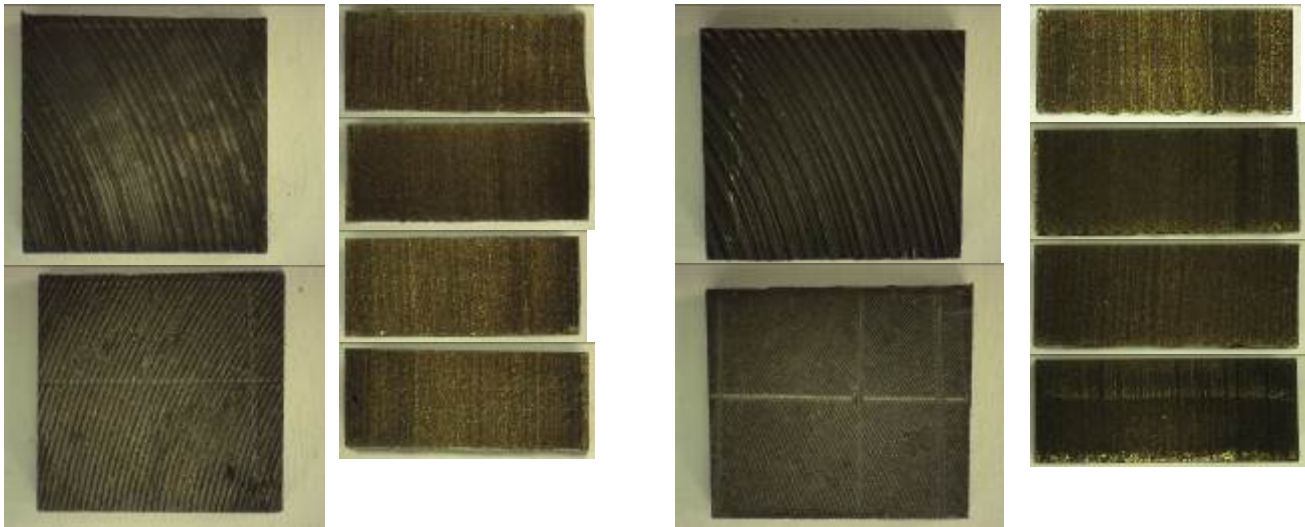


Fig. 1. Photos of the metal uranium sample met\_3 / 07 (left) and met\_6 / 08 (right).

Analysis of the end faces of the samples using MapInfo software has made it possible to determine that the samples were cut and processed on a lathe. The simulation (using Origin) of the spiral profile allowed us to determine the approximate radius of the mergers from which these samples were made. Due to this, it was concluded that the investigated materials are only part of a possible set of samples, and common to them is the technology of ingots from ingots of washers, from which later samples of rectangular shape were cut out. Analysis of the lateral surfaces only using a macrophotography (Fig. 1) does not allow to give a clear answer to the sharpening methods. However, surface investigations using a scanning electron microscope (Fig. 2) and comparison of the obtained images with the images contained in the nuclear forensic database created at the Institute of Nuclear Sciences of the NAS of Ukraine allowed us to establish that the electro-erosion method was used for sample sharpening. sharp. Analysis of surface contamination of samples indicates the use of brass wire for cutting.

The use of modern technologies for the spatial binding of images obtained by various methods has made it possible to establish a correspondence between the characteristics of the elemental composition of individual grains and their color for samples of the standard uranium concentrate CUP-2.

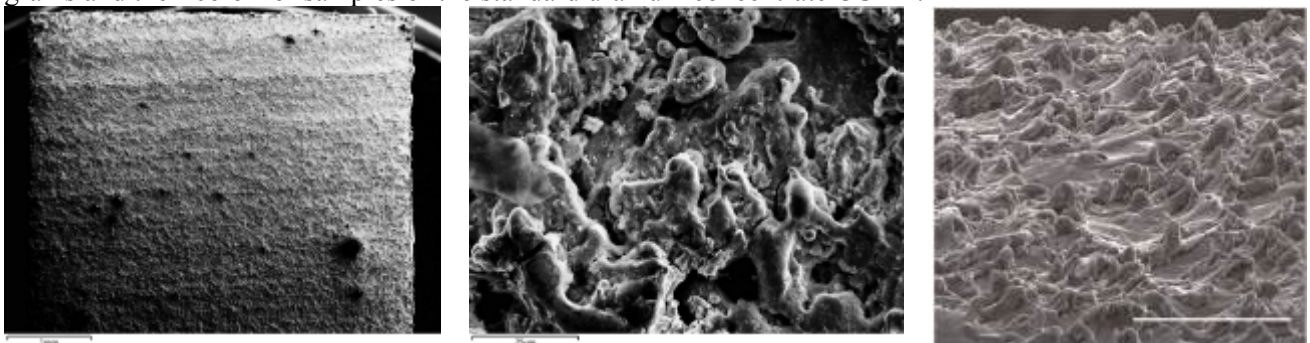
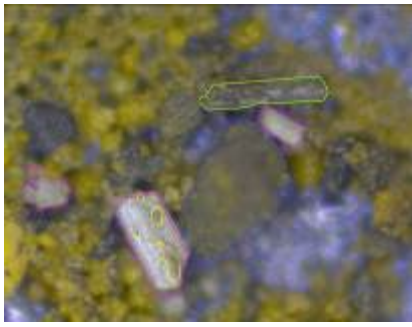
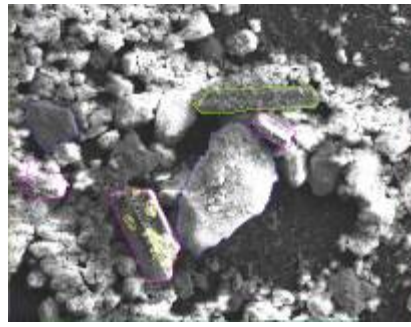


Fig. 2. Image of the lateral surface of metallic uranium samples obtained using a scanning electron microscope Carl Zeiss Research 18 and a sample of the surface after an erosion cut [1].

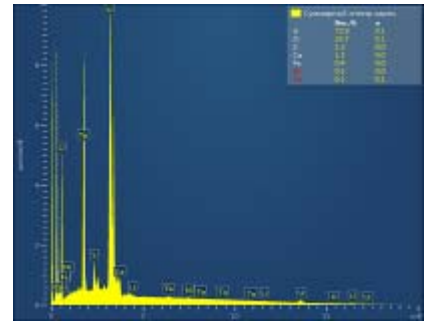
In Fig. 3 shows examples of the spatial binding (by the MapInfo software) images obtained using an optical metallographic microscope and a scanning microscope with an energy-dispersion analyzer.



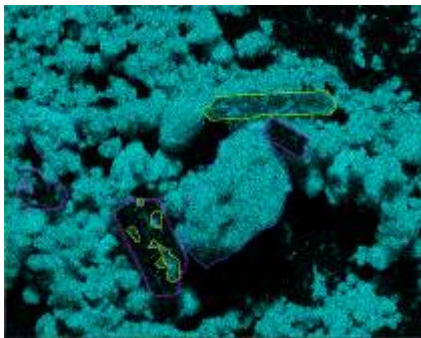
Axio-Vert A1 optical microscope image (10x magnification)



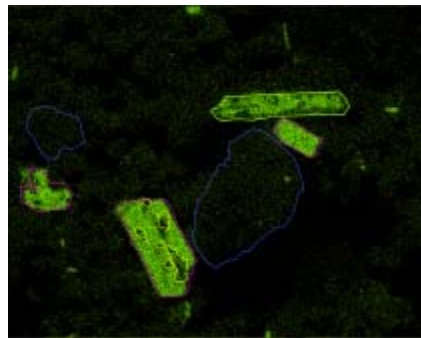
Scanning electron microscope image



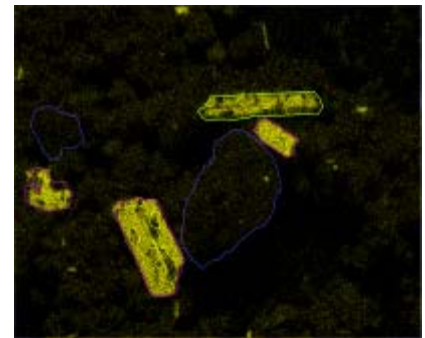
Element distribution spectra of the studied site



Map of the Uranium content distribution



Map of the Calcium content distribution



Map of the Calcium content distribution

Fig. 3. Images of the CUP-2 standard of uranium ore concentrate.

1. Electric discharge machining – A potential choice for surface modification of metallic implants for orthopedic applications: A review / [Prakash C., Kansal H.K, Pabla B.S. // DOI: 10.1177/0954405415579113.

## **PARTICIPATION OF UKRAINIAN EXPERTS IN INTERNATIONAL EXERCISES FOR DEVELOPERS OF NUCLEAR FORENSICS DATABASES "GALAXY SERPENT 4"**

**O. Gaidar, V. Tryshyn, V. Vitiuk, A. Prokopiuk, Ya. Deiun**

*Institute for Nuclear Research, Kyiv, Ukraine*

During 2019 specialists from the Centre for Ecological Problems of Atomic Energy (CEPAE) took participant in the International Exercises for the developers of nuclear forensics databases "GALAXY SERPENT-4. Nuclear Fuel Pellets Investigation and Respond to Investigator's Requests".

The first stage of the training was to create a database for the provided by the organizers a model set of attribute characteristics of various fuel pellets used in different types of reactors.

In the second stage, the results of model analytical studies were provided for 10 uranium fuel pellets from a set of more than 200, which were detected outside the regulatory control. The exercise's participants were asked a series of questions from investigators, in particular: whether there are analogs of the detected tablets in the database created at the first stage; what key parameters were used to establish the analogy; whether a sufficient number of tablets have been examined to characterize the entire set of detected pellets; whether a sufficient number of parameters have been identified in the laboratory and what other studies would be useful for the investigation, etc.

As a result of our analysis, we identified a potential model manufacturer of the studied fuel tablets. Using the Graded Decision Framework (GDF) and analyzing the relationships between uranium isotopes and trace element concentrations (Fig. 1), it was determined that all 10 tablets belong to different batches of nuclear fuel and the number of studied tablets is insufficient to characterize the entire set of detected tablets.

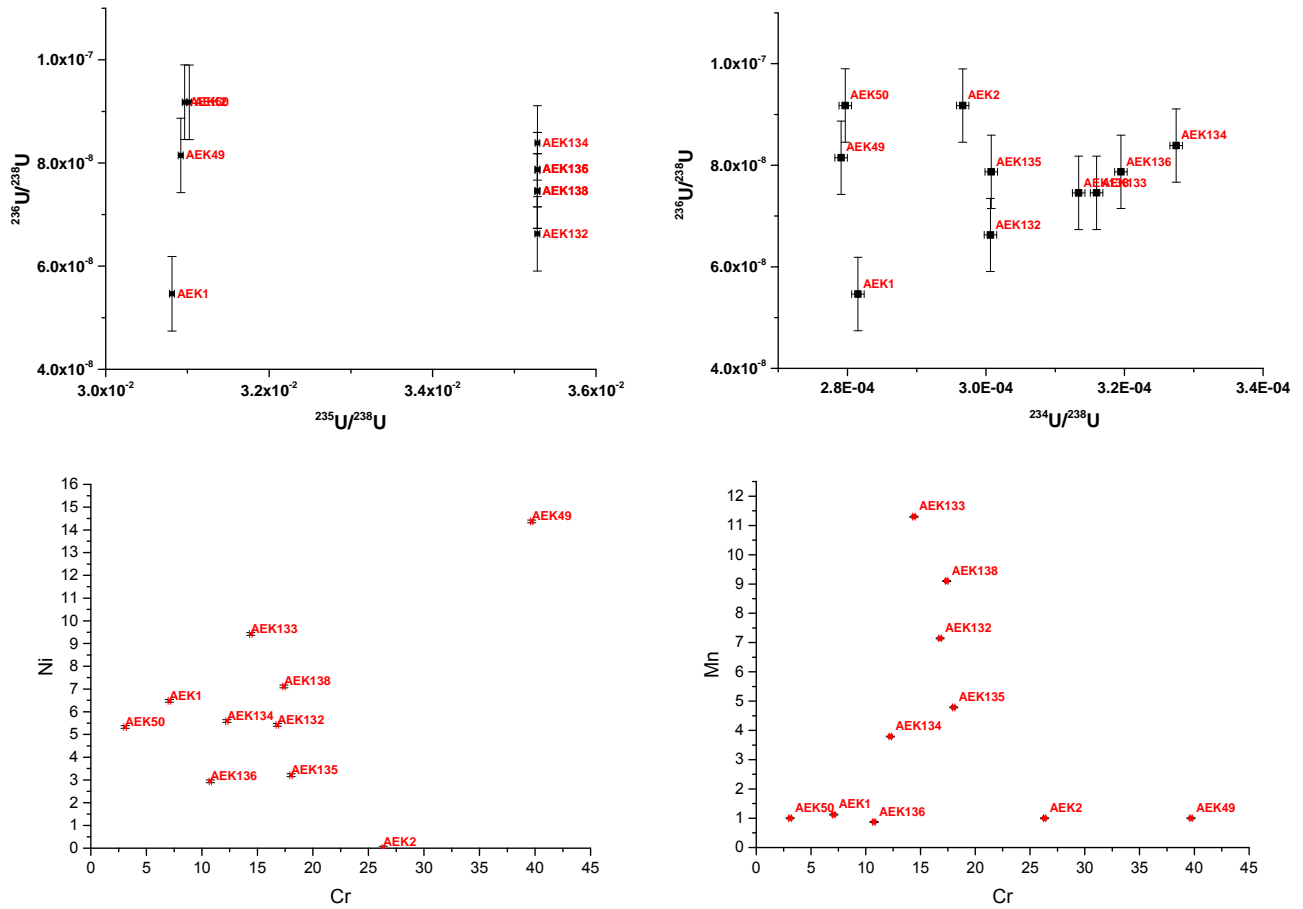


Fig. 1. Dependencies of uranium isotope ratios and trace element concentrations in the 10 fuel pellets

The analysis of the ratios of uranium isotopes to  $^{236}\text{U}$  content has raised several questions that could more clearly determine the origin of the source material, for example, whether the spent nuclear fuel was used in the manufacture of the pellets.

In the third stage, data on the powder sample of enriched uranium, which was found in an underground laboratory, were provided. On the basis of the comparison of the characteristics of the detected powder with the data from the database, it was necessary to answer the questions of investigators, which were generally similar to the previous ones. And in the last fourth stage, analytical data was provided on a sample of a uranium fuel tablet (MKC1) “purchased by investigators” on eBay. In addition to the questions already mentioned, it was additionally necessary to determine whether there was anything in common between all the material found and to determine the degree of reliability of these answers.

According to the results of the analysis (Fig. 2 and Fig.3), it was concluded that all materials probably have a common imaginary manufacturer of nuclear fuel, namely “Kawah Gap”. However, the completeness of the provided information does not allow us to give a more confident answer and fully apply the Graded Decision Framework to the investigator’s questions.

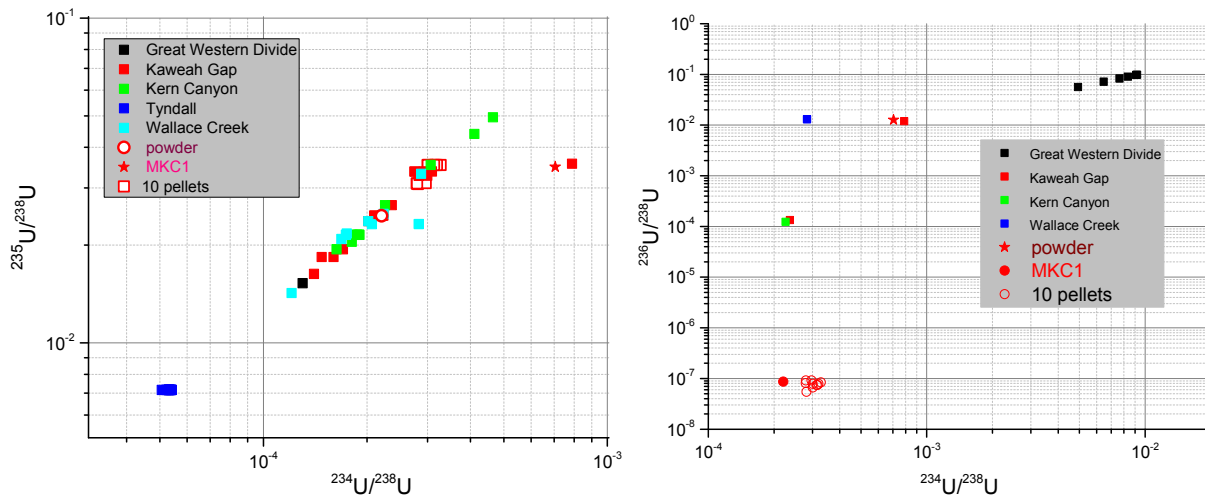


Fig. 2. Dependencies of uranium isotope ratios for “discovered materials” and a model set of tablets

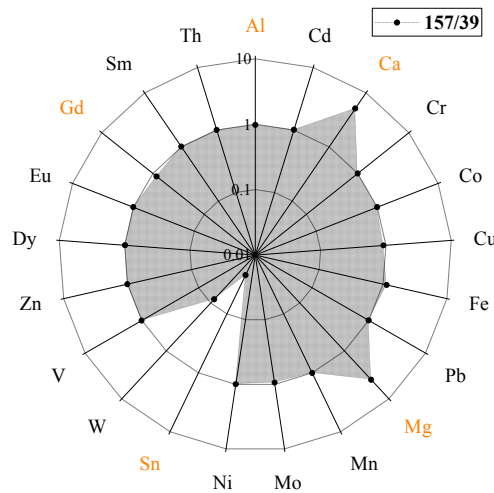


Fig. 3. Radar chart of the relative concentration of the trace element in studied MKC1 pellet (Id=157) and pellet from the Lyell 1 reactor (Id=39) from the known pellet datasheet

## CALCULATION OF SPECTRUM AND NEUTRON FLOW DENSITY IN EXPERIMENTAL CHANNELS OF WWR-M REACTOR

O.G.Diakov, I.A. Maliuk, D.P. Stratilat, M.V. Strilchuk, V.V. Tryshyn

*Institute for Nuclear Research, NAS of Ukraine, Kyiv, Ukraine*

To calculate the spectra and neutron flux densities in the experimental channels of the WWR-M reactor, the Phantom code that uses the Geant4-10-5 libraries was developed. During modeling nuclear interactions, the QGSP\_BERT\_HP library which includes high precision models of neutron processes with energies below 20 MeV was used. The ThermalNeutronScattering model was used to describe the elastic scattering of thermal neutrons with energies below 4 eV. Nuclear process data were taken from the ENDF / B-VIII.0 database (2018). The reactor model which was created is shown in Fig. 1. The configuration parameters of all reactor elements are stored in the database. The database also contains the results of modeling - energy release and density of neutron fluxes in elementary volumes of the core.

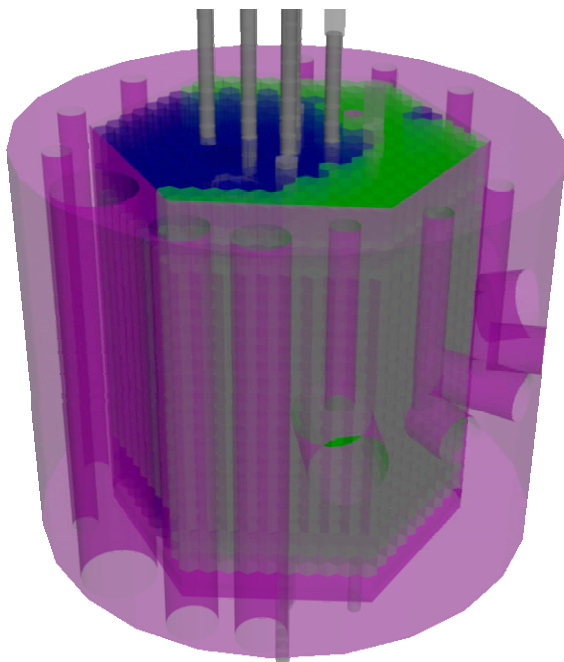


Fig. 1 WWR-M reactor model

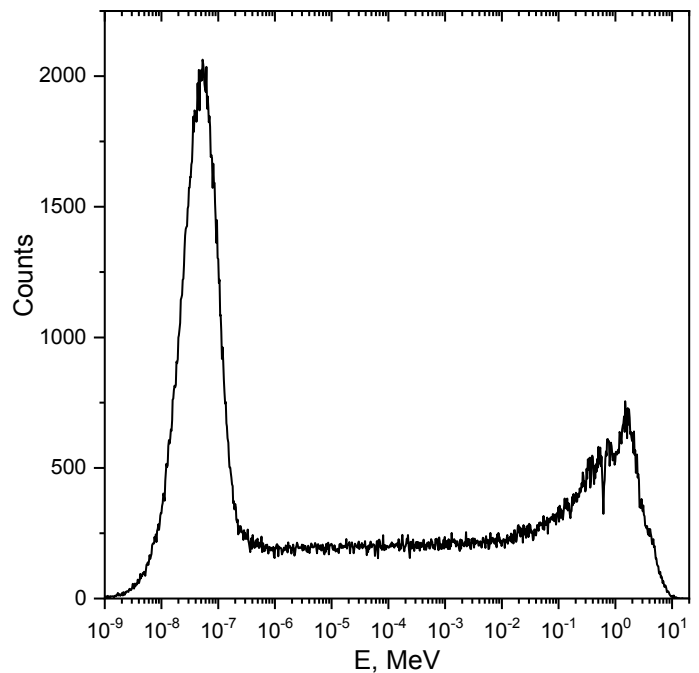


Fig. 2 Calculated neutron spectrum in the channel at a height of -15.6 mm from the center of the core

The code calculated the neutron multiplication factor  $K_{\text{eff}}$  as the ratio of the number of second-generation neutrons emitted to the previous. With the given configuration of the scram rods and the position of the control rods, the calculated value of the  $K_{\text{eff}}$  is close to 1, which is one of the arguments about the correctness of the core model.

Neutron spectra and flux densities were modeled for activation detectors installed in the experimental channel. One of the spectra is shown in Fig. 2.

Due to the small number of simulations ( $\sim 10^8$ ) that can be achieved realistically on a modern PC, only activation detectors with large cross-sections of reactions can be directly irradiated in the reactor model. Therefore, we have developed a model and code for the calculation of PhantomGun reaction rates, in which  $1 \text{ cm}^2$  activation detectors were irradiated with a neutron beam with a flux density and a spectrum calculated for the specific position of the detector and isotropic distribution over the angle of departure to reproduce real irradiation. For comparison, we performed simulations of Mn irradiation directly in the reactor model and with this program. The results of calculating the reaction rate of  $^{55}\text{Mn}(n,\gamma)^{56}\text{Mn}$  by two codes are consistent within the statistical uncertainty.

To verify the calculation of the fluxes and spectra of the neutrons by Phantom, we performed irradiation of activation detectors with different dependences of the cross sections of the reactions on the neutron energy - Mn, Au, Lu and Ni in the experimental channel. After irradiation, the gamma spectra of the activation detectors on the Canberra BE6530 detector were measured and the experimental reaction rates  $R$  per element nucleus were calculated. Figure 3 shows a comparison of the calculated and experimental reaction rates of  $^{176}\text{Lu}(n,\gamma)^{177}\text{Lu}$  through the height of the reactor core.

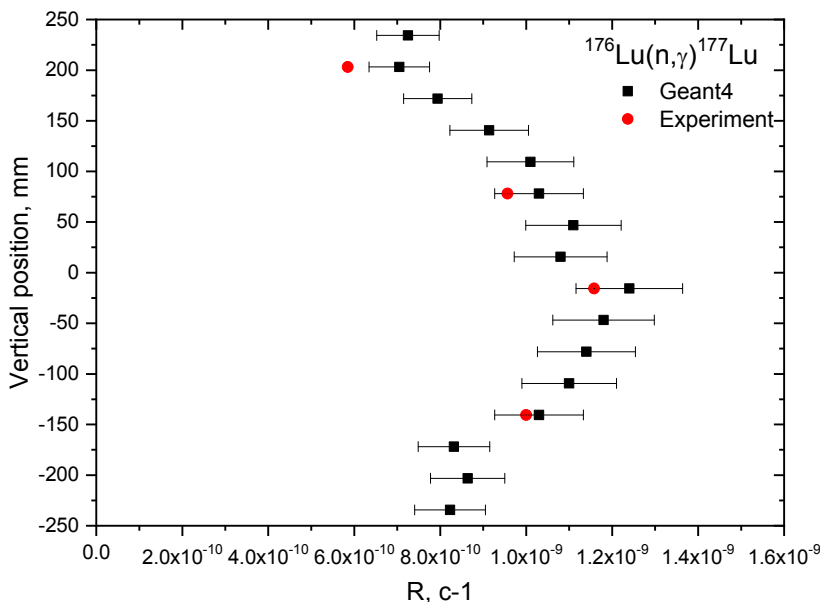


Fig. 3 Comparison of calculated and experimental reaction rates of  $^{176}\text{Lu}(n,\gamma)^{177}\text{Lu}$ , depending on the vertical position of the neutron detector.

The  $^{58}\text{Ni}(n,p)^{58,58\text{m}}\text{Co}$  reaction was used to compare the experimental and calculated values of the reaction rates at fast neutrons. It is impossible to experimentally separate the decomposition of the isomer and the ground state  $^{58}\text{Co}$  because of the low quantum yield of the isomer transition. Therefore, in the reaction simulation, we used the total cross section of two reactions -  $^{58}\text{Ni}(n,p)^{58}\text{Co}$  and  $^{58}\text{Ni}(n,p)^{58\text{m}}\text{Co}$ . Comparison of calculated and experimental values of reaction rates is shown in Fig. 4.

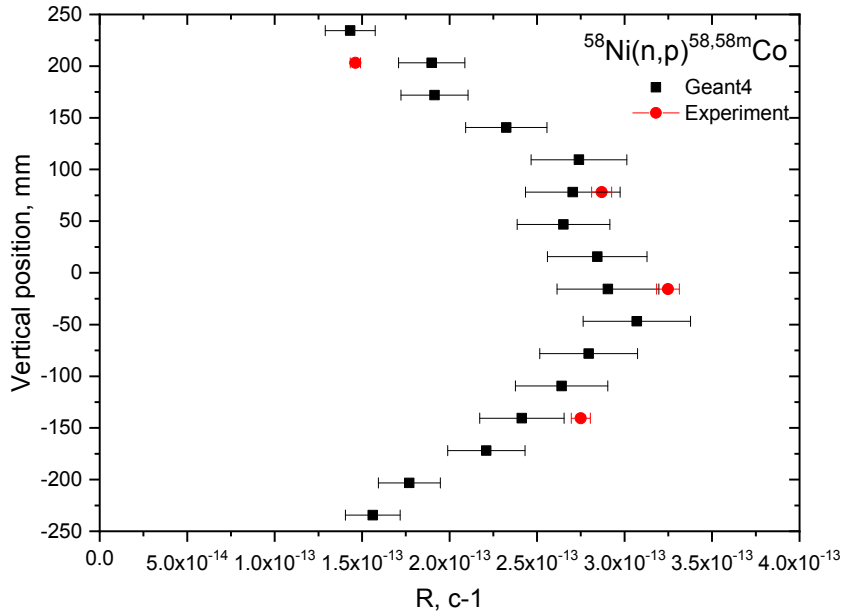


Fig. 4 Comparison of calculated and experimental reaction rates  $^{58}\text{Ni}(n,p)^{58,58\text{m}}\text{Co}$  depending on the vertical position of the detector

1. <https://geant4.web.cern.ch>

### Comparative analysis of signals of long-term gamma-background measurements in the Chernobyl Exclusion Zone by different detectors

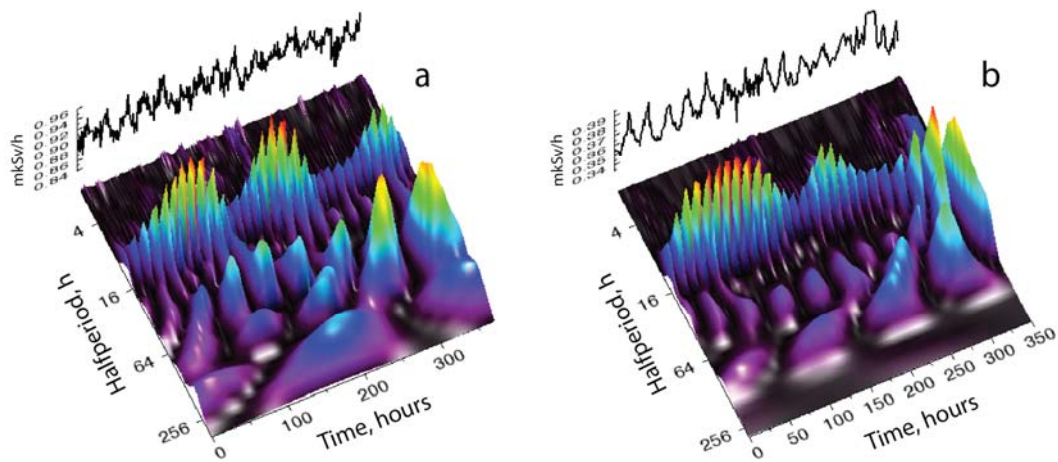
**A. D. Skorbun<sup>1</sup>, O. A. Kuchmagra<sup>1</sup>, B. M. Sploshnoy<sup>2</sup>**

<sup>1</sup>*Institute for Safety Problems of Nuclear Power Plants of the National Academy of Sciences of Ukraine, Kirova st., 36a, Chernobyl, 07270, Ukraine*

<sup>2</sup>*Metrology service of SE COTIS, Kirova st., 21, Chernobyl 07270, Ukraine*

Radioactive contamination of a vast territory is the result of the accident on Unit 4<sup>th</sup> of Chernobyl NPP (ChNPP). At a given time in the 30-km Exclusion zone around ChNPP, the Automated System for Control of Radiation State (ASCRS) is operating. The system consists of some dozens of detectors (observation posts), which are intended to work out-of-doors.

In regular sets of measurements of gamma-background dose power in the Exclusion zone around ChNPP, regular changings of gamma background intensities were discovered. Especially marked ones among them are diurnal, approximately 5-7 days, monthly and other periods.



Three-dimensional pattern of wavelet-transformation coefficients for regular measurements for May 2018: a) GammaTracer detector; b) BDMG-08 detector. The patterns are practically identical. In these patterns on a 12- hour half-period the series of diurnal peaks are seen, amplitudes of which is modulated with the period of 5-6 days

To prove that discovered changes are not connected to peculiarities of equipment work, the signals from two different subsystems of detecting, which work in parallel on ASCRS, have been analyzed. These systems are built on the base of constructively different detection blocks. The subsystems work entirely independently. In one subsystem, signals to auxiliary equipment are sent by cable. Another one has supplied by accumulators, and data are sent through radio channel. The results of measurements in May 2018 were taken to analyzing. In this period, daily modulation of the signals (count rate) was so high that it is seen by naked eyes (see Figure). Such changes exceed all possible changings of detectors characteristics due to meteorological conditions. Simultaneous observations of synchronous signal changes from different detecting systems exclude the possibility to assign them to equipment effects.

### Conclusions

1. Three reasons can cause the periodical changes of signals of ASCRS system in general. 1 – changing of equipment workability due to meteorological conditions; 2 – changing of the source state (screening by water or snow), because the source of gamma radiation is contaminated territory; 3 – receiving of additional or modulating signals from extraterrestrial space.

2. In our previous papers [1, 2] the different possible causes for arising of such effects have been analyzed: equipment work, power feeding, possibility of mistaken data analysis, and influence of meteorological conditions (temperature). The present work is the authors next attempt to discover trivial causes for appearing of the observed effects (periodicities).

3. Usually, the results of a gamma background measurements have a form of a noise-like signal, which is corrupted by season changes. Therefore, the question is arising about the reliability of these signals analyzing and, correspondingly, about the reliability of periodical changes discovering. In [1] by comparative analyzing of measurements from different observation posts, it was shown, that observed periodicities are not the result of random peculiarities of our signals.

4. Furthermore, from results, represented here, due to analyzing of particular time interval (May 2018), where the changes exceed  $\pm 10\%$ , it follows, that meteorological conditions cannot explain such significant changes: equipment is constructed to work in open air, is metrology checked, and its characteristics cannot be changed so profoundly. Besides, the influence of detectors heating was experimentally checked at it was shown, that heating give rise to only small (1-2 %) lowering of registration effectiveness. At the same time, experimental data are changed in phase with temperature changes and values of these changes are much more.

5. It is evident, that occurring of diurnal variations is connected with Earth rotation around its axis. If meteorological conditions (oscillations of temperature, humidity, etc.) are changed as a result of such rotation, then, as a result, observed effects must depend from the daylight hours' duration and the seasons. However, this is not observed. In all analyzed data minima of the diurnal oscillations are observed at 05-07 morning, and maxima at 17-19 evening. Moreover, from time to time, abrupt changes of time for maxima-minima occur, which relax to the norm during 2-3 days. Because this is not equipment failure, it is the most logically to explain these effects with assumption about strict changes in the external source, which modulate our signals.

6. Due to contaminated (mainly  $^{137}\text{Cs}$ ) surrounded territory is the source of gamma emission, it is possible to suppose, that such effect of periodical changes may be caused by humidity oscillations: flood the ground, where mainly radioactive  $^{137}\text{Cs}$  is buried, led to screening of emission. Observation of pointed periodicities in signals, received in the autumn-winter period, reject this cause, not to mention that moisture variations do not have such regular and big changes.

7. In addition to already published and showed in Figure peculiarities, in signals of ASCRS system there are many other regularities, which is impossible to assign to changing of measurement conditions due to rotation of the Earth around the axis. For instance, it was discovered periodical oscillations of signals dispersion with the period about 30 days, maxima and minima of which are appeared near new and full moon.

8. On the base of carried out investigations, we take to conclusion about displaying of cosmic factors in observed signals. Such conclusion is not too much revolutionary: regular changes in radioactive decay velocity were observed by many researchers (literature for this item counts tenth if not hundred papers and its review is not the subject of this report). And although this idea has many opponents, who believe, that all this is incorrect measurements, authors of the given work take to conclusion, that observed changes are the properties of signals, not the equipment effects.

9. However, the question remains open, if in our case the changes of  $^{137}\text{Cs}$  decay velocity under external factors are observed, or detectors of the ASCRS system receive an additional "secondary" emission, which is originated from the Sun or another cosmic sources. To note only, as the author's best knowledge, that secondary gamma emission, originated from cosmic rays, is only a small part of the natural gamma background. In the same time, we deal with signals on the contaminated territory, intensities of which can be in some orders higher, then on the "clean" territories. In this situation contribution of cosmic rays in their standard definition of this phenomenon, is expected to be small.

<sup>1</sup>. A. Skorbun, A. Doroshenko, B. Sploshnoy. Monitoring of gamma background in Chernobyl exclusion zone //XII International Scientific Conference "Monitoring of Geological Processes and Ecological Condition of the Environment", 13 - 16 November 2018, Kyiv, Ukraine  
[http://www.geol.univ.kiev.ua/docs/conf/Prog\\_Monitoring\\_2018\\_final.pdf](http://www.geol.univ.kiev.ua/docs/conf/Prog_Monitoring_2018_final.pdf)

<sup>2</sup>. A. D. Skorbun, O. A. Kuchmagra, B.M. Sploshnoy, A.O. Doroshenko. Periodicities in signals of long-time measurements of gamma-background in Chernobyl exclusion zone. // Yaderna energetyka ta dovykillya. 2019, № 2 (14), c.39-46. (Ukr) <http://npe.org.ua/uk/14-6/>

# LAUE DIFFRACTION OF MÖSSBAUER AND X-RAY PHOTONS BY PERFECT IRON BORATE CRYSTAL

A. Ya. Dzyublik, V. Yu. Spivak

*Institute for Nuclear Research, National Academy of Sciences of Ukraine, Kyiv, Ukraine*

The diffraction of x-rays, synchrotron radiation, Mössbauer rays and neutrons is widely used for analysis of crystal structure. In this way such unique phenomena were discovered as the pendellösung effect and the anomalous transmission of  $\gamma$  photons and neutrons through a perfect crystal in the Laue (transmission) geometry. In the x-ray optics the latter effect is frequently referred as the Borrmann effect [1-3]. The explanation of these phenomena has been given by the dynamical scattering theory [1-3]. In the two-wave case the incident plane x-ray wave generates inside the crystal two couples of waves, both of which are coherent superpositions of the transmitted and reflected waves. One such couple has nodes at the scattering atoms and is therefore anomalously weakly absorbed, whereas another, having antinodes, is strongly absorbed.

The dynamical scattering theory has been extended to the case of elastic diffraction of Mössbauer plane waves by Afanas'ev and Kagan. They predicted that it can be realized complete suppression of  $\gamma$ -quanta by Mössbauer nuclei in perfect crystals, that was confirmed in numerous experiments.

Multiple scattering of x-ray photons by crystals is always described by the Maxwell equations [1-3]. In the same quasi-classical manner Afanas'ev and Kagan [4] treated the resonant scattering of Mössbauer radiation by a crystal

In typical Laue-diffraction experiments the incident  $\gamma$ -quanta are first collimated by a slit, lying on the crystal surface and being parallel to the reflecting planes. And after that the radiation flows within the angular region, which forms a so-called Borrmann triangle (fan). The intensity distribution of the transmitted and reflected beams over the basis of the Borrmann triangle is analyzed with the aid of one more slit, which is also parallel to the reflecting crystal planes.

Standard plane-wave dynamical theory is not able to describe this situation. Therefore Kato considered the Laue diffraction of x-ray spherical waves, treating them like a superposition of the classical plane waves, which spread over the angle  $\theta$  about the Bragg angle  $\theta_B$ . Every such plane component independently of each other are scattered by atoms of the crystal, forming the refracted and diffracted wave packets, represented by the integrals over the angle  $\theta$ . In such a spherical-wave approximation it was silently believed that the dispersion of the incident rays over  $\theta$  much exceeds the characteristic angular interval  $\delta_\theta$ , where the diffraction proceeds. Kato found exact solution of the integral over  $\theta$  in terms of the Bessel function. Besides, these integrals can be estimated over  $\theta$  with the aid of the stationary-phase approximation if the crystal thickness  $D$  to be much larger than the pendellösung length. In other words, it can be applied only to weakly absorbing crystals.

At the same time, for the Mössbauer diffraction, when the resonant scattering amplitude of  $\gamma$ -quanta is already a complex number, the stationary-phase method is not applicable. In this case such integrals should be estimated in more general saddle-point approach. Previously we did this in the spherical-wave approximation, confining ourselves with the symmetric Laue diffraction of both Mössbauer radiation [5] and neutrons [6-7].

We developed general dynamical theory for the Laue diffraction of divergent beams of  $\gamma$ -quanta, taking into consideration both their scattering by atomic electrons and nuclei with low-lying excited levels. We confined ourselves by analysis of the two-wave case, allowing the analytical solution. The derived equations describe the refracted and diffracted beams for arbitrary orientation of the incident beam with respect to the Bragg resonance.

We performed numerical calculations for the symmetric Laue diffraction in the iron borate crystal  $^{54}\text{FeBO}_3$  film by (222) planes. Iron borate has the rhombohedral calcite structure with the spins of the iron atoms lie in the (111) plane and are antiferromagnetically ordered. We got crystal parameters, isotopic enrichment level, Lamb-Mössbauer factor and Rayleigh scattering amplitude from [8]. The calculated intensities of the refracted and diffracted beams are shown in Figure, as a function of the parameter  $p$ .

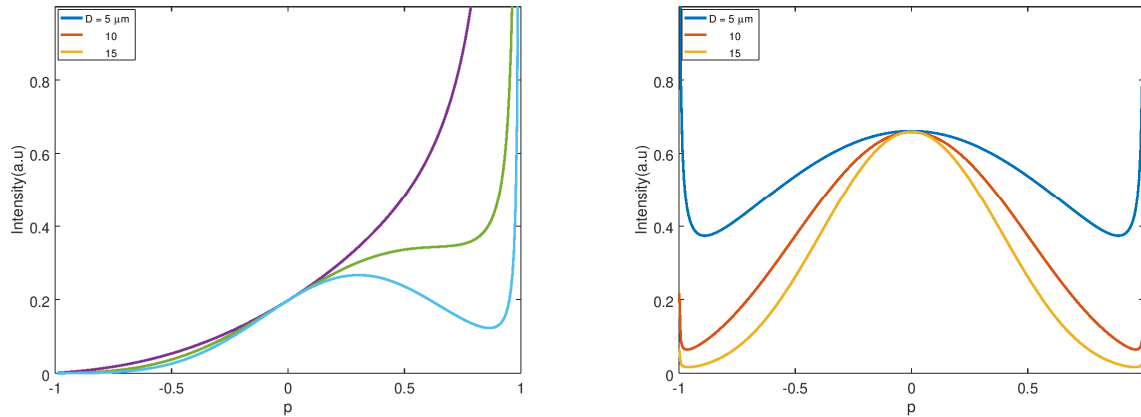


Fig. 1. *Left panel:* Distribution of the Mössbauer beam intensity, refracted in the thin film of different thickness, through the basis of the Borrmann triangle. *Right panel:* Same for the diffracted beam.

1. W.H.Zachariasen, *Theory of X-ray Diffraction in Crystals* (Wiley, New York, 1945).
2. B.W.Batterman, H.Cole, Dynamical diffraction of X Rays by perfect crystals, *Rev. Mod. Phys.* (1964), **36**, 681.
3. Andre Authier, *Dynamical Theory of X-ray Diffraction* (Oxford University Press Inc., New York, 2001).
4. A.M.Afnas'ev, Yu.Kagan, Suppression of inelastic channels in resonant nuclear scattering in crystals, *Sov. Phys. JETP* (1965), *21*.
5. A.Ya.Dzyublik, V.Yu.Spivak, Laue diffraction of spherical Mössbauer waves, *Ukr. J. Phys.* (2016), *61*, 826.
6. A.Ya.Dzyublik, V.I.Slisenko, V.V.Mykhaylovskyy, Symmetric Laue diffraction of spherical neutron waves in absorbing crystals, *Ukr. J. Phys.* (2018), 174.
7. A.Ya.Dzyublik, V.V.Mykhaylovskyy, V.Yu.Spivak, Peculiarities of Laue diffraction of neutrons in strongly absorbing crystals, *Zh. Eksp. Teor. Fiz.* (2019), *155*, 413.
8. U van Brück, G. V. Smirnov, R. L. Mössbauer, H. J. Maurus and N. A. Semiochkina, Enhanced nuclear resonance scattering in dynamical diffraction of gamma rays, *J. Phys. C.* (1980), 4511.

## FEATURES OF PHYSICAL PROPERTIES OF OPTICALLY ACTIVE CRYSTALS $ZnP_2$ , $CdP_2$ , $ZnGeP_2$ . THE EFFECT OF ELECTRON IRRADIATION

**I. Matiyuk<sup>1</sup>, R. Vernydub<sup>2</sup>, O. Kyrylenko<sup>2</sup>, O. Konoreva<sup>3</sup>, P. Litovchenko<sup>3</sup>, O. Radkevych<sup>4</sup>, V. Tartachnyk<sup>3</sup>**

<sup>1</sup>*V.E. Lashkaryov Institute of Semiconductor physics of NAS of Ukraine, Kyiv, Ukraine*

<sup>2</sup>*National Pedagogical Dragomanov University, Kyiv, Ukraine*

<sup>3</sup>*Institute for Nuclear Research of NAS of Ukraine, Kyiv, Ukraine*

<sup>4</sup>*SE "SRI of Microdevices" STC "Institute for Single Crystals" of the NAS of Ukraine, Kyiv, Ukraine*

Zinc diphosphate and cadmium diphosphate are noncentrosymmetric crystals of group  $A^{II}B_2^V$ , having a complex lattice, a large refractive index and being optically active, they can be used in nonlinear optics as frequency multipliers, converters infrared radiation on visible radiation, frequency mixers; based on  $ZnP_2$  Schottky diodes and heterojunctions are manufactured and operate.

The gyrotropic properties of  $ZnP_2$  and  $CdP_2$  are manifested in the rotation of the plane of polarization of the light wave, circular dichroism, elliptical double refraction of the ray and etc.

Among other optically active substances, they are distinguished by a large rotation constant. If in quartz it is 21 deg/mm, then in  $\text{ZnP}_2$  it is 350 deg/mm, in  $\text{CdP}_2$  it is 640 deg/mm. Of the 20 known inorganic gyrotropic objects, only 4 in the visible region have a dispersion of natural optical activity close to  $\text{ZnP}_2$ .

The Faraday interband effect in  $\text{ZnP}_2$  is a linear function of magnetic field induction up to 220 kHz for  $\lambda = 632,8$  nm, which distinguishes it from Ge, where  $\theta(V)$  is saturated at much smaller fields. The spectrum near the edge absorption of zinc diphosphate contains two groups of lines. At  $E \perp C$  the boundary line  $h\nu = 1,547$  eV; at  $E \parallel C$  with another series arises. There is a correlation between the respective lines of the two series. The spectrum character resembles a system of exciton lines in GaP doped with nitrogen [1].

Irradiation of  $\text{ZnP}_2$  crystals by electrons with  $E = 14$  MeV ( $F = 10^{17}$  cm $^{-2}$ ) is accompanied by an increase in the density of states in the bandgap. In the range of 1,55-2,05 eV, a monotonic increase in the absorption coefficient is observed, against which a selective band stands out  $h\nu = 1,74$  eV. Increased thermal stability violation of the structure of radiation origin, responsible for the occurrence of the strip, indicates the complexity of the structure of the center. It can be both a complex of a radiation defect with an admixture and a violation of the antistructural type.

The restoration of the shape of the absorption edge and the disappearance of the band  $h\nu = 1,74$  eV occurs after annealing at 400 °C; moreover, in comparison with the spectrum of the initial crystal, the fundamental absorption edge becomes more expressive, transmission in the impurity absorption zone increases, which indicates partial destruction of defects technological damage as a result of radiation-thermal treatment.

The introduction of radiation defects is also accompanied by a redistribution of the intensities of individual lines of the two-phonon absorption spectrum and the appearance of new frequencies. The destructive effect of radiation mainly concerns the frequencies inherent in the vibrations of phosphorus quasi molecules, so we conclude that phosphorus chains in  $\text{ZnP}_2$  are sensitive to radiation.

Features of cadmium diphosphate is the existence of phosphorus quasi molecules weakly bound to metal atoms. Cadmium ions in such a system are in a weak periodic potential of a phosphoric hydrate, which creates the conditions for stepwise ordering in the structure of coordination tetrahedral.

Irradiation by electrons with  $E = 14$  MeV, cadmium diphosphate, as in the case of  $\text{ZnP}_2$ , leads to initial deformation of the edge of the optical absorption due to the influence of the tails of the density of states – at low doses, and until its complete disappearance – at large doses ( $F = 1,2 \cdot 10^{18}$  cm $^{-2}$ ). The recovery as a result of isochronous annealing is also stepless, characteristic of crystals with a high concentration of defects of various types.

Diamond-like chalcopyrites  $A^{II}B^{IV}C_2^V$  are close analogs of elementary semiconductors Ge and Si, as well as binary semiconductors  $A^{III}B^V$ . The lattice  $A^{II}B^{IV}C_2^V$  can be obtained from  $A^{III}B^V$  compounds by replacing two atoms of the third group with atoms of the second and, accordingly, atoms of the fifth group with atoms of the fourth group. The ordered arrangement of the components in the metal sublattice implies a transition from the cubic structure of  $A^{III}B^V$  to the tetragonal structure  $A^{II}B^{IV}C_2^V$ .

Zinc-germanium diphosphate is a noncentrosymmetric crystal with all the signs of non-linear optical characteristics; its nonlinear coherence is 35-75  $\mu\text{m}/\text{V}$ , which is approximately 160 times higher than this value for binary  $\text{ZnP}_2$  and  $\text{CdP}_2$ . High optical transparency in the region of 0,74-12  $\mu\text{m}$ , a significant threshold of optical damage (50 MW/cm $^2$  at a wavelength of  $\lambda = 2,09$   $\mu\text{m}$  and 150 MW/cm $^2$ ,  $\lambda = 2,96$   $\mu\text{m}$ ) under the influence of high-power laser fields  $\text{ZnGeP}_2$  is indispensable as a frequency converter of the middle and infrared range, devices for suppressing guidance systems of self-guided weapons for hitting air targets, and precision surgical laser instruments.

In parametric radiation generators of the range  $\lambda = 3,5-8$   $\mu\text{m}$ , the power can reach 40 W with a conversion coefficient of 50 %. The creation of a terahertz frequency emitter based on  $\text{ZnGeP}_2$  is also promising.

In addition to the mentioned features, the main advantages of  $\text{ZnGeP}_2$  compared to other optically active materials are a wide transmission area, good mechanical and physical parameters, among which high thermal conductivity occupies an important place. Significant mechanical strength allows it to be used in conditions of elevated levels of vibration and the presence of aggressive environments.

Triple compounds  $A^{II}B^{IV}C_2^V$  with the structure of chalcopyrite can also be used as active converters of solar energy into electrical energy; be analogues of ferrites with appropriate doping.

The main problem of  $\text{ZnGeP}_2$  is the heterogeneity of the composition, which can reach 1-50  $\mu\text{m}$  and cause a spread of optical parameters [2]. Widespread use of  $\text{ZnGeP}_2$  is restrained by additional optical absorption in the range of 0,65-2,5  $\mu\text{m}$ . The authors of [3] associate it with point defects of the  $V_{\text{Zn}}$  or  $\text{Ge}_{\text{Zn}}$  type. The

results obtained on ZnGeP<sub>2</sub> crystals irradiated with electrons ( $E_e = 2$  MeV) suggested that the main influence on absorption is created by  $V_{Zn}$ .

At the same time, it was shown in [3] that upon electron irradiation of the same energy and subsequent annealing, the absorption coefficient in the region of 0,6-2  $\mu\text{m}$  decreases.

The question of the effect of radiation on the optical characteristics of ZnGeP<sub>2</sub> samples remains uncertain. No additional information on the effect of irradiation on optical absorption was found for this particular semiconductor.

The results of our work indicate that the level of influence of the tails of the density of states formed by radiation defects on the edge absorption of irradiated ZnGeP<sub>2</sub> is at least not lower than that of its analogue from the A<sup>III</sup>B<sup>V</sup> – GaP group [4]. If in the initial crystal, despite the presence of inhomogeneities, the position of the fundamental absorption edge can still be estimated ( $h\nu = 1,91$  eV), then in the irradiated with electrons ( $E = 14$  MeV,  $F = 1,2 \cdot 10^{18}$  cm<sup>-2</sup>), it could not be detected; measurements of large values of the  $\alpha$  coefficient require the use of superfine samples.

The restoration of optical transmission during isochronous annealing proceeds steplessly, which is a consequence of both a high concentration of damage caused by radiation and their active interaction with the initial structural damage, when the number of types of defects becomes much more diverse.

1. V.V. [Sobolev et al. JETP Letters](#) 34, No 3 (1981) 108.
2. A. Gribenyukov et al. *Quantum Electronics* 48, No 5 (2018) 491.
3. V. Voevodin et al. *Tomsk State University Journal. Physics* 285 (2005) 63-73 (In Russian).
4. E. Brailovsky. *Ukrainian Journal of Physics* 26, No 6 (1981) 973-977 (In Russian).

## THE INFLUENCE OF RADIATION-REPLACED ATOMS ON DOSIMETRIC CHARACTERISTICS OF DGT-4

**I.G. Megela, V.T. Maslyuk, T.O. Vieru-Vasilitsa, O.M. Pop**

*Institute of Electron Physics, Nat. Acad. Sci. of Ukraine, Uzhgorod*

It is known that thermoluminescent sensors use the effect of creating non-equilibrium charge carriers with ionizing radiation, which is partially trapped on the traps. After irradiation, the samples are heated, causing the trapped media to be trapped and reach the centers of radiated recombination, and the radiation intensity measured to be proportional to the absorbed dose. Usually, the process of elastic scattering on the lattice atoms of the bombarding particles, which leads to the formation of radiation defects such as displaced atoms. In the general case, they can be both centers of non-radiative recombination, which reduce the radiation output, and additional traps or centers of radiation, which increases the radiation output.

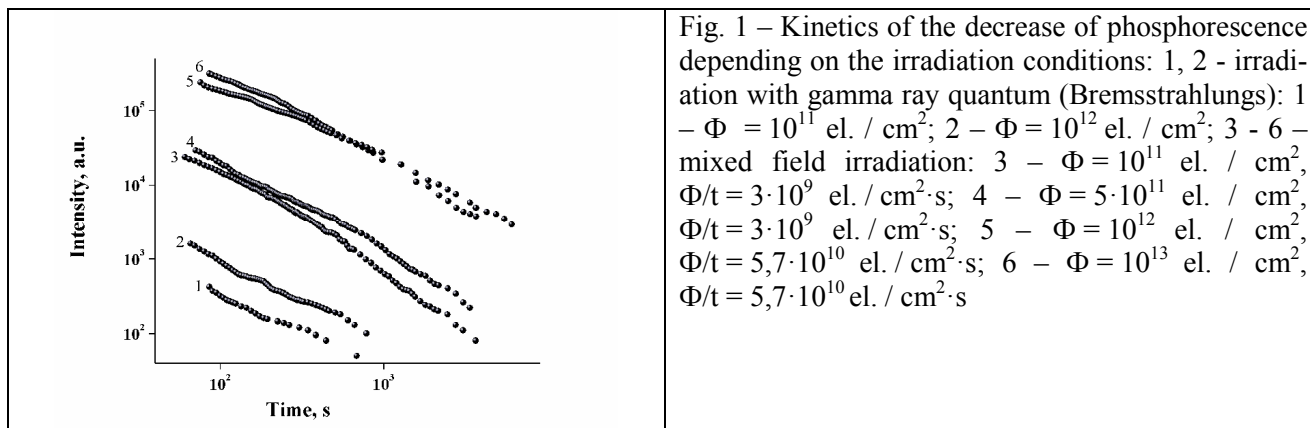
In this work, in order to study the role of radiation defects in thermoluminescent (TSL) dosimetry, irradiation of standard dosimeters DGT-4 with accelerated electrons with an energy of 10 MeV was performed. The irradiation was carried out similarly to the method of irradiation of cancer patients [1].

After output from the microtron, through the thin titanium foil window, the beam was scattered on another tantalum foil and formed by a collimator. The magnitude and heterogeneity of the formed field was measured by a Faraday absolute cylinder with a calibrated inlet and did not exceed 0.5% at the sampling point. The Faraday cylinder was calibrated by a passing translucent secondary emission monitor, which determined a given electron fluence. It is evident that electron irradiation was accompanied by inherent inhibitory gamma radiation, that is, electron irradiation is irradiation by a mixed electron-gamma beam. The irradiation was performed separately only from which its electrons were extracted by aluminum absorption 30 mm thick, similar to the method used by us [2, 3] to determine the Bremsstrahlung effect.

The yields of phosphorescence and TSL depending on the irradiation dose were measured. The technique of thermoluminescence measurements is described in [2, 3]. Thermoluminescence curves were obtained as a result of direct heating of the samples at a rate of 0,50C / sec to maximum temperature values of 3000C. Phosphorescence measurements were performed starting from the first minute after irradiation, and thermoluminescence output was measured after phosphorescence was reduced to near zero.

It was found that, as well in Li<sub>2</sub>B<sub>4</sub>O<sub>7</sub> crystals [4], NCP dosimeters [3], Al<sub>2</sub>O<sub>3</sub> [2], the long-term phosphorescence of irradiated DHT-4 dosimeters with high-intensity electron and gamma beams was observed. The obtained regularities are as follows: there is the dependence of the phosphorescence output both on flu-

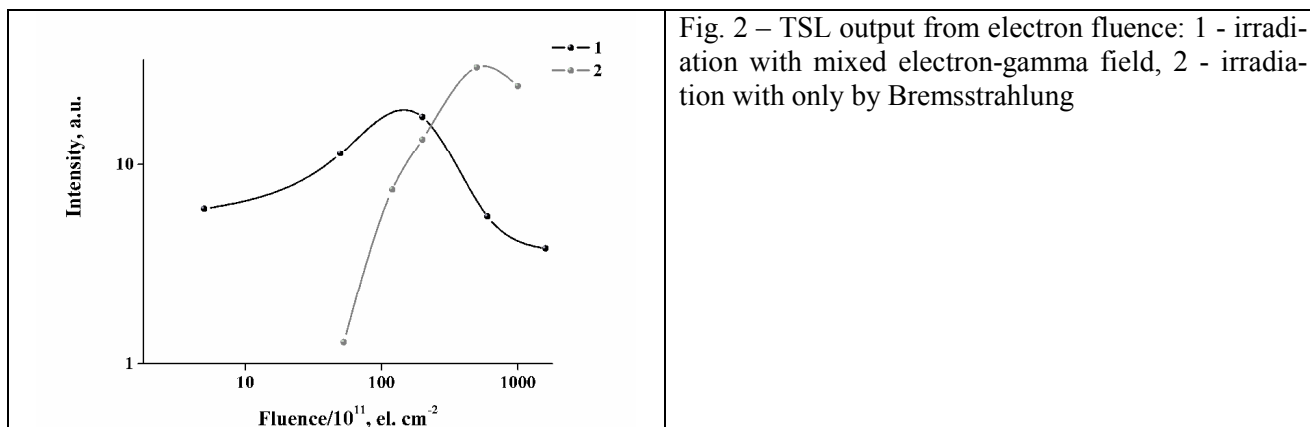
ence and on the intensity of irradiation; the saturation of the phosphorescence yield is observed for each intensity value. Thus, for the intensity of irradiation  $3 \cdot 10^9$  el. /  $\text{cm}^2 \cdot \text{s}$  saturation of phosphorescence output at fluences exceeding  $10^{11}$  el. /  $\text{cm}^2$  is observed, and at the intensity of  $5,7 \cdot 10^{10}$  el. /  $\text{cm}^2 \cdot \text{s}$  – at fluences greater than  $10^{12} - 10^{13}$  el. /  $\text{cm}^2$  (Fig.1). For comparison, in this figure, the output of phosphorescence of the Bremsstrahlung irradiated samples in the units of fluence of the electrons that caused it are also given.



As can be seen from the above data, the phosphorescence yield, in this case, is much smaller. These patterns indicate that in the crystals studied, in addition to the traps responsible for thermoluminescence, there are also small traps, the exit of trapped carriers from them occurs in the process of irradiation. Obviously, at high radiation intensities, the trapping rate of the traps of the carriers is greater than the rate of their release. If the rate of capture is equal to the rate of release, the saturation of the output of phosphorescence from the fluence is observed. The lower phosphorescence yield at gamma irradiation is explained, first of all, by the lower intensity of ionization

As was determined by our experiments with mixed electron-gamma fields and only Bremsstrahlung irradiation, typical TSL curves are observed for DGT-4 samples, in which the peak at  $225^\circ\text{C}$  is the main dosimetric peak. The peak area, or maximum yield, is proportional to the absorbed dose.

Figure 2 shows the dependence of the TSL output on electron fluence for two irradiation cases: a mixed electron-gamma field (curve 1) and an isolated Bremsstrahlung gamma field (curve 2). As can be seen from the figure, at the beginning of the irradiation, the contribution of Bremsstrahlung radiation in the formation of the TSL response is substantially smaller than the contribution of mixed irradiation. Starting with fluences greater than  $1 \cdot 10^{13}$ , the contribution of the Bremsstrahlung irradiation, which is only a fraction of the mixed, becomes more extensive because the TSL output decreases as the fluence increases. While the contribution of Bremsstrahlung radiation continues to increase.



The obtained results can be explained by the formation of more radiation defects, such as displaced atoms under mixed irradiation. Indeed, electron irradiation, in comparison with gamma irradiation defects, is formed as a result of elastic scattering of relativistic electrons atoms. In contrast, at gamma irradiation, the displacement of atoms can be formed only by secondary electrons arising from Compton-effect and photo

effects and the formation of electron-positron pairs. Obviously, from the obtained results, it follows that radiation defects are leading centers of non-radiative recombination, which reduces the TSL output.

1. Kovalev V.P. et al. Device for the formation of uniform dose fields with a maximum electron utilization coefficient // *Medical Radiology*. – №12. – 1974 г. – с.47 (in Russian).
2. Maslyuk V.T., Megela I.G., Okunieva T.O., Pekar J.M., Pekar V.J. Specific features of the influence of high-energy electron beams on the luminescent properties of undoped and Nb, Fe-doped  $Al_2O_3$  crystals // *Radiat. Prot. Dosim.* – 2014. – 162. – P. 34 - 37 (doi:10.1093/rpd/ncu213).
3. Maslyuk V.T., Megela I.G., Obryk B. & Vieru-Vasilitsa T. O. Luminescent properties of  $LiF:Mg,Cu,P$  detectors irradiated by the 10-MeV electrons // *Radiation effects & defects in solids*. – 2017 – V. 172, Is. 9-10. – P. 782-789 (<https://doi.org/10.1080/10420150.2017.1393425>).
4. Maslyuk V., Megela I., Okunieva T., Holovey V., Birov M. On the Possibility of the Use of the Long-Term Phosphorescence of the  $Li_2B_4O_7:Cu$  and  $Li_2B_4O_7:Mn$  Crystals for the High-Current Electron Beam Dosimetry. Proceedings of the Second International Conference on Radiation and Dosimetry in Various Fields of Research (RAD 2014), pp. 215–218 (Niš, Serbia: Nais Print), 2014, p 274.

## SELF-OSCILLATIONS IN RADIATION PHYSICS. CRYSTALLINE METHANE UNDER ELECTRON IRRADIATION

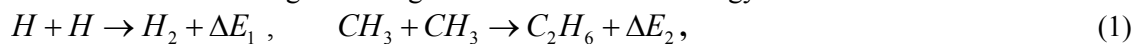
V.I. Sugakov

*Institute for Nuclear Research, National Academy of Science of Ukraine, Kyiv*

Self-oscillations (the appearance of a periodical time dependence of physical parameters in stationary conditions) are a widespread phenomenon in the nature. In the radiation physics, the thermoconcentrational self-oscillations develop at some conditions due to an accumulation of defects and energy in crystal under irradiation by high energy particles. A release of the accumulated energy may occur depending on the value of the energy and parameters of the crystal either gradually under heating of the crystal (under an annealing) or spontaneously as a result of an appearance of the instability. The instability may lead to the increase of temperature so much that the crystal is destroyed or to an appearance of the periodical oscillations of the temperature and the defect concentration, in other words, to the self-oscillations [1,2].

In the paper the self-oscillations in crystalline methane are investigated. Methane in the solid state (at the temperature lower 90K) is used as a moderator of neutrons [1] and it is an object of an investigations in cosmology [3]. The first observations of the self-oscillations were obtained in methane under neutron irradiation [1]. The authors of the paper [4] are revealed and studied two types of the self-oscillations at irradiation of methane by electrons of the energies (1-3)eV at low temperature. The results of theoretical investigations of self-oscillations in the methane under electron irradiations are given in the presented report.

During the irradiation of the crystal, the molecules of methane  $CH_4$  disintegrate to different radicals; the radical  $CH_3$  and hydrogen  $H$  are the most important for the explanation of the self-oscillation formation. These radicals react during a meeting with each other with energy emission



where  $\Delta E_1 = 218 \text{ kДж / моль}$ ,  $\Delta E_2 = 368 \text{ kДж / моль}$ . The release of the energy growths under activation nature of the radical movement and accumulation of the energy may causes temperature instability and an appearance of the self-oscillations.

The system of equations for the defect concentrations has the form

$$\frac{\partial n_1}{\partial t} = G_1 - K_{01} \exp(-E_{a1}/(\kappa T))n_1^2, \quad \frac{\partial n_2}{\partial t} = G_2 - K_{02} \exp(-E_{a2}/(\kappa T))n_2^2, \quad (2)$$

$$lc(T) \frac{\partial T}{\partial t} = P - E_1 K_{01} \exp(-E_{a1}/(\kappa T))n_1^2 l / v_0 - E_2 K_{02} \exp(-E_{a2}/(\kappa T))n_2^2 l / v_0 - B (T - T_b), \quad (3)$$

where  $n_1$  and  $n_2$  are concentrations of  $H$  and  $CH_3$  relatively to the concentration of  $CH_4$  in methane,  $G_1$  and  $G_2$  are the relative numbers of atoms H and molecule  $CH_3$ , created by the irradiation per unit time,

$c(T)$  is the volume heat capacity of the methane, the value of  $P$  describes the heating of the sample by the irradiation, the value of  $B$  is the energy transfer of the heat to thermostat,  $v_0$  is the volume per one molecule of the methane,  $E_{a1}$  and  $E_{a2}$  are activation energies of the radical diffusion.

As far as the energy incident electrons is small, the dissociation of the methane occurs as results of sub-threshold processes under the energy transfer to proton movement from excited states in particular from the triplet states, that have a large lifetime. Under calculations, the thin films of samples with the thickness of order of the lengths of the electron range (the value about tenth of micrometers) are considered. In this case the spatial distribution of defects in the film may be considered uniform. The calculations took into account the dependence of heat capacity on temperature.

The system of equations (2,3) has many solutions depending on the parameters of the systems. At some parameters, the solutions exist, in which the investigated values (the defect concentrations, temperature) are monotonic functions of time. There are solutions, which describe the oscillations with single frequency. From here we present the solutions of the equations (2,3), which describe the oscillations with two frequencies, that arises in the different periods of times. Namely such types of oscillations are observed in the experiments in the work [4].

In the presented work the solutions obtained, which describe two types vibrations, the vibrations of concentrations of  $CH_3$  radicals and the concentrations of hydrogen atoms  $H$ . Simultaneously, temperature oscillates with two frequencies. It is seen from Fig.1, that the growths of occurs in time according to linear law. At some value of  $CH_3$  concentration, the instability arises, the  $CH_3$  concentration drops sharply and the great outburst of temperature till 100K and higher is observed. Later on, the defects are accumulated again and the time dependence of the concentration repeats. At considered parameters the self-oscillations of the hydrogen atom concentration appears at the beginning of the irradiation and at the region of the time, at which the outburst of temperature takes place.

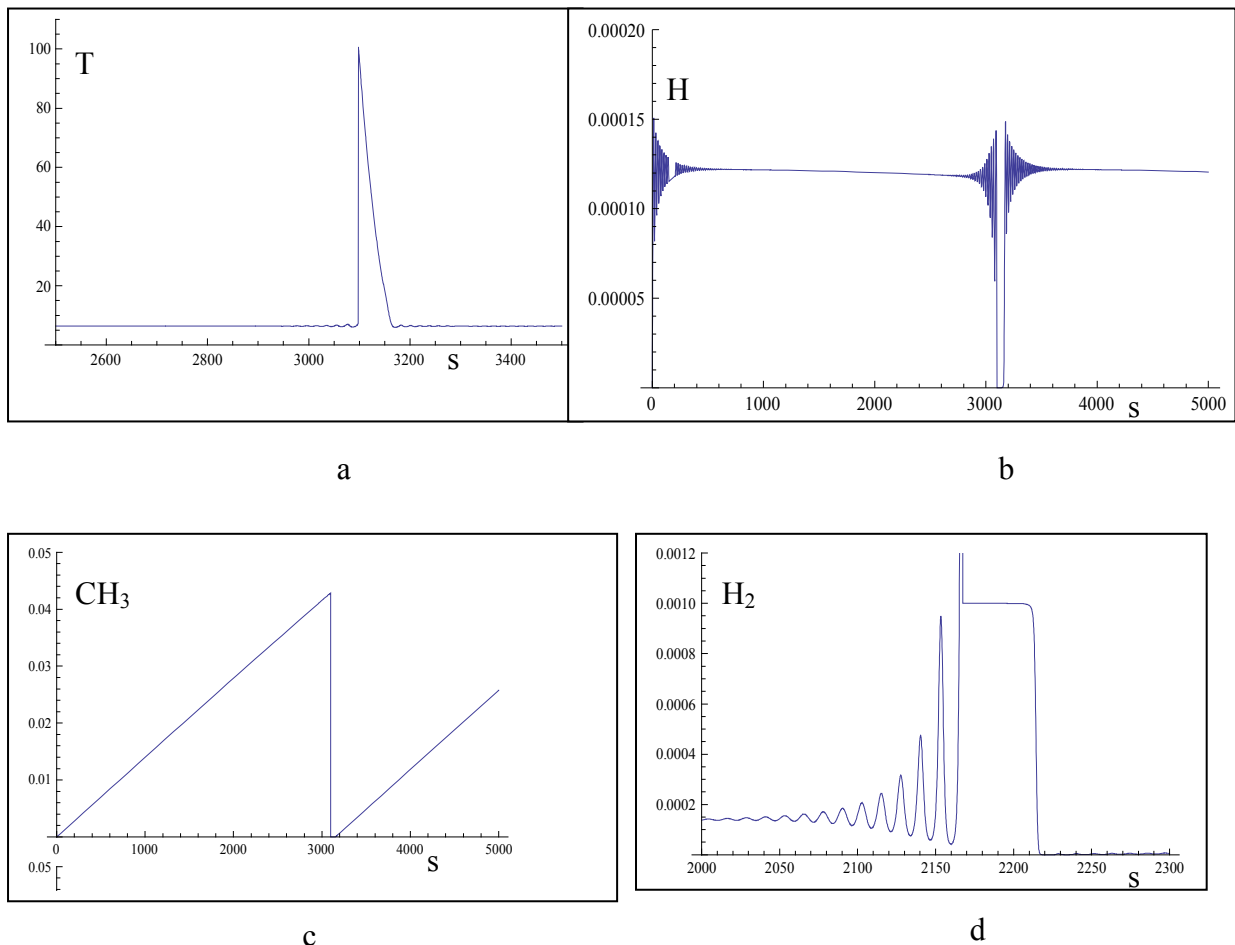


Fig.1. The time dependence of temperature a) , hydrogen atom concentration b), the radical  $CH_3$  concentration c) in the methane under irradiation, the hydrogen molecule intensity leaving from the methane film d).

The calculations show that the periods of the self-oscillations increases at decreases of the intensity of the irradiation. The large period has order of hour. The small period, which connected with oscillations of the hydrogen atom concentration, is the value of 10 second. These results agree with experimental data obtained in [4]. According to calculations, the oscillations and outburst of temperature are represented in the desorption of atoms and molecules from the film of irradiated methane, that observed in the experiment [4].

1. John M. Carperten. Nature **330** (1987) 358.
2. P. A. Selishchev, V. I. Sugakov . *Sov. Phys. Solid State* **30** (1988)1503.
3. O. Kirichek, C.R.Lawson, D.M. Jenkins, C.J.T. Ridley, D.J. Haynes. *Cryogenics* **88** (2017)10.
4. И.В. Хижный, С.А. Уютнов, М.А. Блудов, Е.В. Савченко. *Low Temperature Physics* **44** (2018)1565.

## **OPPORTUNIES FOR INCREASING LIFETIME OF NON-EQUILIBRIUM STATES**

**V. V. Ryazanov**

*Institute for Nuclear Research, National Academy of Sciences of Ukraine, Kyiv, Ukraine*

A distribution is introduced that contains the thermodynamic parameter of the lifetime. Operations with the average value of the logarithm of this distribution, non-equilibrium entropy, make it possible to obtain thermodynamic relations that contain the lifetime of the statistical system. The difference between equilibrium and non-equilibrium entropies is related to flows in the system. This change in entropy is expressed in terms of the thermodynamic parameter of non-equilibrium associated with the lifetime. The statistical sum, free energy, internal energy are divided into equilibrium and non-equilibrium parts. The non-equilibrium parts are expressed through the Laplace transform of the distribution of the lifetime. The possibilities for increasing the lifetime depend on the behavior of this distribution. So, for the exponential distribution of the lifetime and the case when the equilibrium entropy is larger than the non-equilibrium, the average lifetime does not increase for one stationary non-equilibrium state or for an ensemble of stationary non-equilibrium states. This behavior of the exponential distribution is explained by the fact that this is the limit distribution, in the limit of infinitely large times. And we consider the final times of life. For systems whose lifetime is described by the distributions of Weibull, Gompertz and others, there are possibilities for increasing the lifetime. Opportunities for describing the growth of average life time are also provided by the stochastic queuing theory. The general results for the distributions obtained using the maximum entropy method also allow a description of the increase in the lifetime.

## **THEORETICAL INVESTIGATION OF THE FEATURES OF THE CHARGE CARRIER TRANSPORT IN AMORPHOUS OXIDE SEMICONDUCTORS**

**I. I. Fishchuk**

*Institute for Nuclear Research, National Academy of Sciences of Ukraine, Kyiv, Ukraine*

In [1], a model of random fluctuation of the edge of a conduction band was proposed to describe the kinetic characteristics of amorphous oxide semiconductors with high charge carrier mobility. In [2] it is stated that the proposed model is the most suitable for the description of kinetic processes in these semiconductors. In [1], the effective medium approach was used to calculate the charge carrier mobility within the framework of the proposed model, and the percolation theory was used in [2]. Both approaches to calculating the effective charge carrier mobility in these semiconductors have been shown to produce similar results. However, in [1, 2] calculations of the mobility of charge carriers did not take into account the degeneration of charge carriers at their high concentration, which takes place in the study of kinetic characteristics in the scheme of thin field transistors. In this paper, we have performed the calculations of the mobility of charge carriers by method of the effective medium approach taking into account their degeneration. In the model proposed in [1], disorder is caused by the random fluctua-

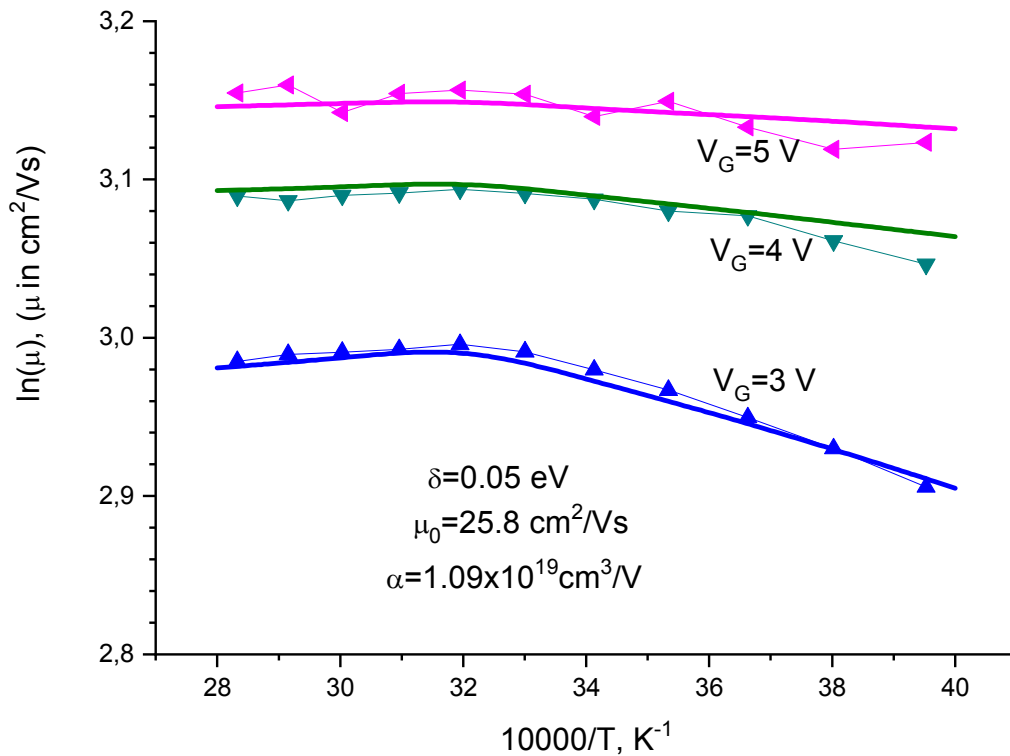
tions in the local edge of the conduction band  $\varepsilon_m$ , which is described by the Gaussian distribution  $g(\varepsilon_m)$  with width  $\delta$ . Density of band states at energy  $\varepsilon > \varepsilon_m$  was used as  $D_m(\varepsilon) = D_0 \sqrt{\varepsilon - \varepsilon_m}$  with  $D_0 = 1.4 \times 10^{21} \text{ cm}^{-3} \text{ eV}^{-3/2}$  for thin films of a-IGZO. For the total local charge carrier concentration we have  $n_m = \int_{\varepsilon_m}^{\infty} d\varepsilon D_m(\varepsilon) f(\varepsilon)$ , where  $f(\varepsilon) = 1 / \{1 + \exp[(\varepsilon - \varepsilon_F) / k_B T]\}$ ,  $\varepsilon_F$  is the Fermi level,  $T$  is the temperature. The local electroconductivity  $\sigma(\varepsilon_m)$  with taking into account the generation of charge carrier, as it follows from papers [3, 4], can be written as  $\sigma(\varepsilon_m) = e\mu(\varepsilon_m)n(\varepsilon_m)$ , where

$$\mu(\varepsilon_m) = \mu_0 (2/3) \langle \varepsilon \rangle_m / k_B T, \quad n(\varepsilon_m) = \int_{\varepsilon_m}^{\infty} d\varepsilon D_m(\varepsilon) f(\varepsilon) [1 - f(\varepsilon)], \quad (1)$$

$$\langle \varepsilon \rangle_m = \int_{\varepsilon_m}^{\infty} D_m(\varepsilon) (\varepsilon - \varepsilon_m) f(\varepsilon) [1 - f(\varepsilon)] d\varepsilon / \int_{\varepsilon_m}^{\infty} D_m(\varepsilon) f(\varepsilon) [1 - f(\varepsilon)] d\varepsilon. \quad (2)$$

For calculation of the effective electroconductivity  $\sigma_e$ , which describe the whole amorphous semiconductor we used, as in [1], the effective medium approach equation

$$\left\langle \frac{\sigma(\varepsilon_m) - \sigma_e}{\sigma(\varepsilon_m) + 2\sigma_e} \right\rangle = 0, \quad \langle Q_m \rangle = \int_{-\infty}^{\infty} d\varepsilon_m g(\varepsilon_m) Q_m. \quad (3)$$



Dependency of charge carrier mobility on temperature for SPINEL 200C sample, 80% (coupled symbols are experimental data [5], solid curves are theoretical results).

The total charge carrier concentration  $n$  in semiconductor can be calculated by expression  $n = \int_{-\infty}^{\infty} d\varepsilon_m g(\varepsilon_m) n_m$ . In scheme of the thin field transistor the concentration  $n$  in ohmic region can be measured as  $n = \alpha(V_G - V_{TH})$ , where  $\alpha$  is coefficient,  $V_G$  is the gate voltage,  $V_{TH}$  is the threshold voltage. For the value  $\mu$ , which describe the charge carrier mobility in whole semiconductor, we have  $\mu = \sigma_e / en$ . Note that the threshold voltage  $V_{TH}$  can be depend on the temperature, i.e.  $V_{TH} = V_{TH}(T)$ , which can significantly affect on mobility  $\mu$ .

The figure shows the dependence of charge carrier mobility on the temperature for the SPINEL 200.C sample, 80% [5] at the gate voltages  $V_G = 3, 4$  and  $5V$  and the experimentally obtained threshold voltage approximated by the expression

$$V_{TH}(T) = 1.9 - [0.06 \times (y - 28) \times \Theta(32 - y) - 0.03 \times (y - 40) \times \Theta(y - 32)] \quad (4)$$

Here  $\Theta(t) = 1$  for  $t \geq 0$ ,  $\Theta(t) = 0$  for  $t < 0$ ,  $y = 10000/T$ . This dependence has minimum at  $y = 32$ .

Thus, the specificity of the obtained temperature dependence of mobility is due to a certain kind of temperature dependence of the threshold voltage  $V_{TH}(T)$ . With a temperature-independent threshold voltage, we obtain the usual increase of mobility with increasing temperature over the entire temperature range, which is typical for disordered systems.

1. I. I. Fishchuk et al., Phys. Rev. B **93**, 195204 (2016).
2. A. V. Nenashev et. al., Phys. Rev. B **100**, 125202 (2019).
3. V. Palenskis, Wold Journal of Condensed Matter Physics, **3**, 73 (2013).
4. V. Palenskis, Wold Journal of Condensed Matter Physics, **4**, 123 (2014).
5. A. Glushkova, private communication.

## FAST MAGNETOACOUSTIC MODES IN INHOMOGENEOUS PLASMA

**O. S. Burdo, Ya. I. Kolesnichenko**

*Institute for Nuclear Research, National Academy of Sciences of Ukraine, Kyiv, Ukraine*

High frequency fast magnetoacoustic modes (FMM), i. e., the FMM modes with frequencies above or close to ion gyrofrequency, are considered.

The basic equation for FMM which was derived in the work has the form:

$$\frac{1}{r} \frac{d}{dr} r Q \frac{d \delta B_{\parallel}}{dr} + (1 - k_b^2 Q) \delta B_{\parallel} = 0, \quad (1)$$

where  $\delta B_{\parallel}$  is perturbed magnetic field,  $Q = Q(\varepsilon_+, \varepsilon_-, k_b, k_{\parallel})$ ,  $k_{\parallel}$  and  $k_b$  and are wavenumber components along the magnetic field and binormal to field line, respectively,  $\varepsilon_+$  and  $\varepsilon_-$  are dielectric permeability tensor components.

In WKBJ (Wentzel-Kramers-Brillouin-Jeffrey) approximation this equation reduces to

$$N_{\perp}^2 = (c^2 / \omega^2) Q^{-1}, \quad (2)$$

with  $N_{\perp} = c \sqrt{k_r^2 + k_b^2} / \omega$ . Eq. (2) is used in theory of Ion Cyclotron Resonance Heating (ICRH), but it is useful also for the eigenmode analysis due to the fact that eigenmodes can be considered as a superposition of two travelling waves, one of them moving outwards the plasma and another one moving inwards. It follows from Eq. (2) that there exist cut-off surfaces (where  $N_{\perp}^2 = 0$ ) determined by  $\varepsilon_{\pm} = N_{\parallel}^2$  and concomitant evanescence regions (where  $N_{\perp}^2 < 0$ ). In particular, an evanescence region exists at the plasma periphery where the particle density is small. This implies that the mode amplitude should be small at the periphery in the case when WKBJ approximation is applicable to radially travelling waves constituting the mode. A necessary condition for this is  $N_{\parallel}^2 > 1$ , which can be written as

$$\kappa_{\parallel}^2 > \tilde{\omega}^2 v_A^2 / c^2, \quad (3)$$

where  $\tilde{\omega} = \omega / \omega_B$ ,  $\kappa_{\parallel} = k_{\parallel} \rho_A$ ,  $\omega$  the mode frequency,  $\rho_A = V_A / \omega_B$ ,  $V_A$  Alfvén velocity,  $\omega_B$  the ion gyrofrequency. The cut-off radius  $r_1$  is determined by

$$\kappa_{\parallel,0}^2 \approx \eta(x_1) \tilde{\omega}^2 / (1 + \tilde{\omega}), \quad (4)$$

where  $\kappa_{\parallel,0} = \kappa_{\parallel}(0)$ ,  $\eta(x)$  describes plasma inhomogeneity and is defined by  $n_j = n_0 \eta(x)$ ,  $x_1 = r_1 / a$ ,  $a$  is the plasma radius  $j = e, i$ .

On the other hand, one can expect that the inhomogeneity will have a minor influence on FMMs when equation (3) is not satisfied, especially when  $\kappa_{\parallel} = 0$ . Then no evanescences are expected and, therefore, the modes having global radial structure with maximum amplitude far from the magnetic axis and edge-localized modes may exist. In particular, if both  $\kappa_r \equiv k_r \rho_A$  and  $\kappa_{\parallel}$  are small, so that  $\kappa_b$  dominates (and the poloidal mode number is large,  $m \gg 1$ ), plasma inhomogeneity may weakly affect the radial structure of FMM. This case is well studied in connection with conventional edge-localized ICE.

Numerical solution of Eq. (1) confirms this qualitative analysis, see Figs. 1 and 2 calculated for the cases when Eq. (3) is satisfied (Fig. 1) and not satisfied (Fig. 2). We observe in Fig. 1 that the plasma inhomogeneity suppress the mode amplitudes at the periphery, the effect being largest when plasma density

is strongly peaked. In contrast, no evanescence occurs and modes are located at the periphery in Fig. 2.

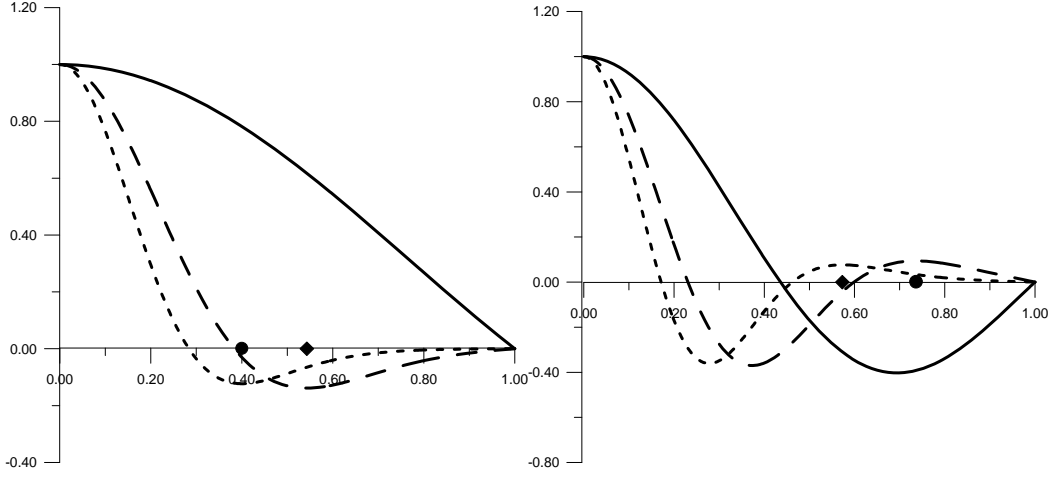


Fig. 1. Radial structure of FMMs with  $m = 0$ ,  $\tilde{\omega} = 2$  in homogeneous and inhomogeneous plasmas. *Left panel*: solid line, homogeneous plasma and  $\kappa_{\parallel,0} = 1.1454$ ; long-dashed curve,  $\eta^{(2)}(x) = \sqrt{1-x^2}$  and  $\kappa_{\parallel,0} = 1.0594$ , short-dashed curve,  $\eta^{(3)}(x) = (1-x^2)^2$  and  $\kappa_{\parallel,0} = 0.9702$ . *Right panel*: solid line, homogeneous plasma and  $\kappa_{\parallel,0} = 1.1012$ ; long-dashed curve,  $\eta^{(2)}(x) = \sqrt{1-x^2}$  and  $\kappa_{\parallel,0} = 0.9507$ ; short-dashed curve,  $\eta^{(3)}(x) = (1-x^2)^2$  and  $\kappa_{\parallel,0} = 0.7756$ . The cut-off radii are shown by diamonds and circles. We observe that the modes became more peaked at the magnetic axis due to plasma inhomogeneity.

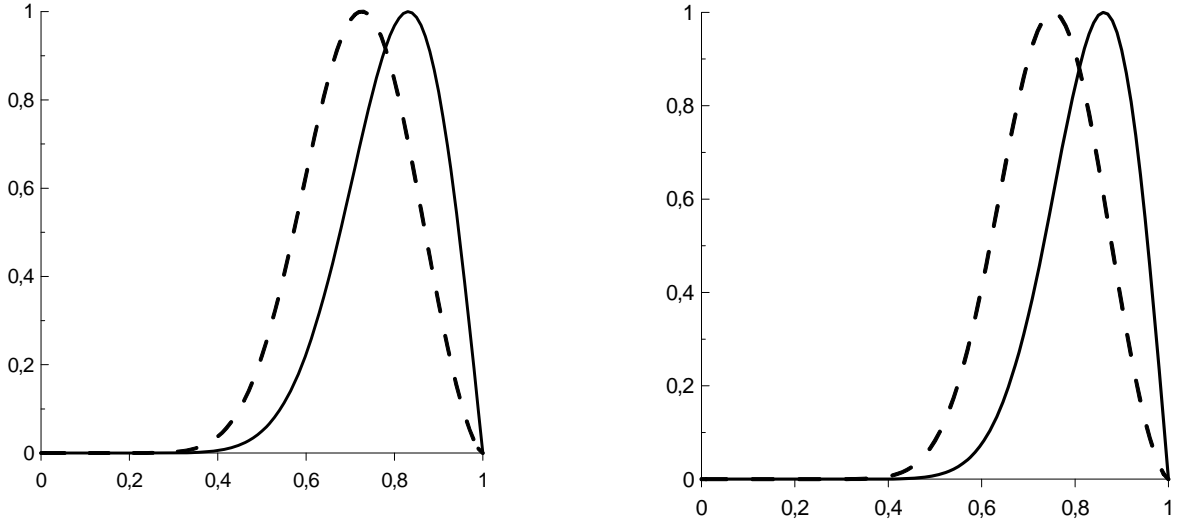


Fig. 2. Radial structure of FMMs with  $m \gg 1$  and  $\kappa_{\parallel,0} = 0$  in homogeneous and inhomogeneous plasmas. *Left panel*:  $m = 12$ , solid curve, homogeneous plasma and  $\tilde{\omega} = 1.5199$ ; dashed curve, inhomogeneous plasma and  $\tilde{\omega} = 2.0015$ . *Right panel*:  $m = 17$ , solid curve, homogeneous plasma and  $\tilde{\omega} = 2.0182$ ; dashed curve, inhomogeneous plasma and  $\tilde{\omega} = 2.7205$ .

## PARALLEL 2.5D ELECTROMAGNETIC PIC CODE FOR SIMULATIONS OF INTERACTION BETWEEN PLASMA AND CHARGED PARTICLE BUNCHES OR ITS SEQUENCES

**O. K. Vynnyk, I. O. Anisimov**

*Taras Shevchenko National University of Kyiv, Faculty of Radio Physics, Electronics and Computer Systems, Kyiv, Ukraine*

Parallel fully relativistic code for kinetic simulation of beam-plasma interaction, using particle-in-cell method proposed. The programming code, PiCOPIC, is a successor of PDP3[1] code. It expands capabilities of previous code, avoid its limitations and demonstrates much better performance on multicore/multiprocessor computers, as it designed for fully-parallel computing.

Requirement for a new code has arisen during the study of interaction between multi-bunch electron beams with a background plasma [2, 3]. In particular, better calculation algorithms and higher accuracy requires fully parallel calculation. It can not be achieved with PDP3 due to its single-threaded architecture.

The code consists of two parts: a high-performance application for plasma simulation and a library for data analysis and visualization with collection of ready-to-use tools, built on top of this library. The simulation application uses several alternative algorithms for the initial placement and velocities distribution of macroparticles, calculation of the equations of motion, temperature etc. Calculation algorithms selecting by specifying preprocessor directives before compilation. Preprocessor directive assignments are integrated into the compilation helper scripts.

The PiCOPIC code implements PIC loop with three basic stages: integration of the motion equations of macroparticles and moving it; extrapolation of charges, coordinates and velocities of macroparticles to the grid of current densities (an alternative to the direct solution of Poisson equation); calculating the electric and magnetic fields on the grid and fields gathering back to the macroparticles to prepare for next iteration. Each stage has several algorithms setting by specifying the preprocessor directives.

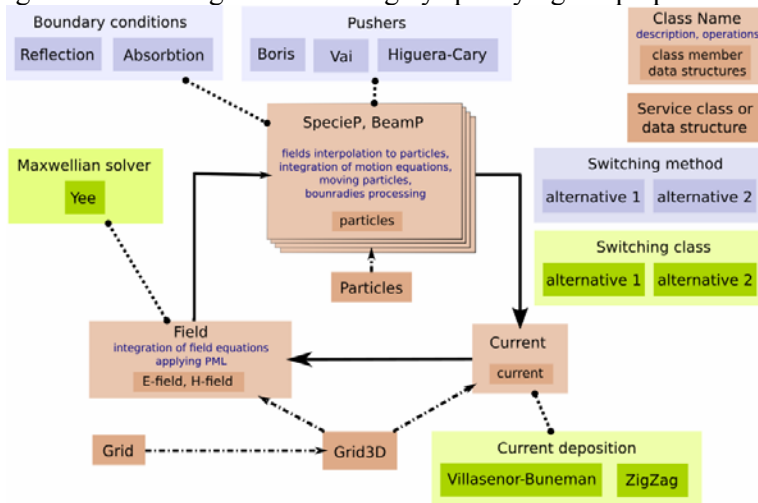


Fig. 1. PiCOPIC implementation of PIC loop (for single domain). Current and fields grids are implemented on top of “Grid3D” data structure — 3-component grid with overlay areas for domain overlaying. It also contains operators and methods for easy access to it.

Integration of equations of motion implemented with following schemes: Boris[5], Vay[6], or Higuera-Cary[7]. Vay or H-C schemes are more suitable for calculating long-term processes (comparing to the time step), as they do not have velocity-related numerical artifacts (Boris’s scheme is not energy converging). Current deposition can be altered between Willassenor-Bunemann[8] or ZigZag[9] schemes. Electric and magnetic fields implemented with FDTD (Yii)[10] scheme.

PiCOPIC, as well as its predecessor, uses so-called 2.5-dimensional (coordinates  $r$  and  $z$  and velocities  $v_r$ ,  $v_\varphi$  and  $v_z$ ) axisymmetric (cylindrical) geometry. The macroparticles are presented there as rings, symmetrical to the axis of the simulation area.

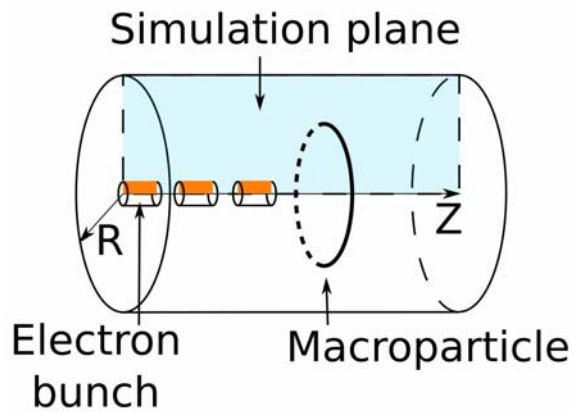


Fig. 2. Geometry of PDP3/PiCOPIC. Data output shape is “simulation plane” as the simulation area is axisymmetric

The simulation area is separated to independently running domains to obtain parallel execution. Domains synchronizes the values of fields, currents, and particles with neighboring domains when it needed, at the end of the simulation stage. Edges of each domain contains so called overlays that are synchronized to emulate a continuity effect. So, weighting/extrapolation procedure is smoothly for particles as well as for fields and currents.

New programming code for kinetic simulation of beam-plasma integration, optimized for multibunch particle beams developed. Code uses 2.5D geometry as well as its predecessor. Code is fully-parallel and allow to combine different calculation algorithms for each stage of simulation loop.

1. Y. M. Tolochkevych, T. E. Litoshenko, and I. O. Anisimov, “2.5d relativistic electromagnetic PIC code for simulation of the beam interaction with plasma in axial-symmetric geometry,” *Journal of Physics: Conference Series*, vol. 511, p. 012001, May 2014.
2. O. K. Vynnyk and I. O. Anisimov, “Wake wave excited by the sequence of relativistic electron bunches: Initial stage,” *Problems of Atomic Science and Technology*, vol. 6 (118), pp. 160–163, 2018.
3. O. K. Vynnyk and I. O. Anisimov, “Evolution of the wake wave excited by the sequence of the relativistic electron bunches,” *Problems of Atomic Science and Technology*, vol. 4 (122), pp. 55–58, 2019.
4. C. K. Birdsall and A. B. Langdon, *Plasma physics via computer simulation*. New York: Taylor and Francis, 2005.
5. J. P. Boris, “Relativistic plasma simulation-optimization of a hybrid code,” pp. 3–67, 1970.
6. J.-L. Vay, “Simulation of beams or plasmas crossing at relativistic velocity,” *Physics of Plasmas*, vol. 15, no. 5, p. 056701, 2008.
7. A. V. Higuera and J. R. Cary, “Structure-preserving second-order integration of relativistic charged particle trajectories in electromagnetic fields,” *Physics of Plasmas*, vol. 24, no. 5, p. 052104, 2017.
8. J. Villasenor and O. Buneman, “Rigorous charge conservation for local electromagnetic field solvers,” *Computer Physics Communications*, vol. 69, no. 2, pp. 306 – 316, 1992.
9. T. Umeda, Y. Omura, T. Tominaga, and H. Matsumoto, “A new charge conservation method in electromagnetic particle-in-cell simulations,” *Computer Physics Communications*, vol. 156, no. 1, pp. 73 – 85, 2003.
10. Yee, K, “Numerical solution of initial boundary value problems involving maxwell’s equations in isotropic media,” *IEEE Transactions on Antennas and Propagation*, vol. 14, pp. 302–307, May 1966.

## THE INFLUENCE OF HYDROGEN PLASMA TREATMENT ON PHOTOLUMINESCENT CHARACTERISTICS OF KESTERITE PHOTOELECTRIC ABSORBERS ( $\text{Cu}_2\text{ZnSnS}_4$ )

**V. V. Hladkovskyi<sup>1</sup>, R. A. Redko<sup>2,3</sup>, M. O. Semenenko<sup>2</sup>, O. V. Hladkovska<sup>1</sup>**

<sup>1</sup>*Institute for Nuclear Research, National Academy of Sciences of Ukraine, Kyiv, Ukraine*

<sup>2</sup>*Institute of Semiconductor Physics, National Academy of Sciences of Ukraine, Kyiv, Ukraine*

<sup>3</sup>*State University of Telecommunications, Kyiv, Ukraine*

$\text{Cu}_2\text{ZnSnS}_4$  (CZTS) is a promising material for creating, high-efficiency thin-film photoelectric converters (PCs). CZTS is characterized by a direct band gap, a high absorption coefficient, and the absence of toxic components in its manufacture, which are widespread in the earth's crust and are technologically and cost-effective.

Over the past decade, researchers have focused on the development of such materials using vacuum [1] or non-vacuum methods [2]. The best efficiency in PC was achieved on the basis of CZTS(Se) with a useful energy conversion factor of up to 12.6% [3]. At the same time, the effectiveness of such films is highly dependent on the state of the surface that is crucial to produce high quality films with good uniformity without secondary phases. In order to increase the efficiency of kesterite based devices, it is necessary to understand a number of mechanisms observed during the growth of such films. The purpose of this work is to investigate the features of the influence of hydrogen plasma generated in controlled magnetic fields on the photoluminescent characteristics of CZTS absorbers of PCs grown at different sulfurization pressures.

Photoluminescence (PL) is widely used as an informative method for detecting radiative/non-radiative recombination centers. For CZTS thin films intended for solar power, the high rates of radiative recombination and, accordingly, the search for methods of reducing the channel of irradiated recombination by passivation of dangling bonds, reduction of Auger recombination, and reducing the concentration of deep centers of non-radiative recombination, which invariably appear during the fabrication. The main problems encountered in the manufacture of films are the presence of primary significant internal mechanical stresses as well as dangling bonds, which leads to an increase in the effect of defects on the violation of the transport properties of films. An effective way of overcoming this problem is to passivate the dangling bonds with small diameter atoms, for example, by adding hydrogen atom to the structure. Due to the high reaction activity, hydrogen can attach to the dangling bonds, this result in a significant decrease in their concentration as it was discussed in Ref. [4].

Plasma treatment of CZTS took place in a plasma-chemical reactor (PCR) of planar geometry with a magnetic field that is oriented parallel to the surface of the RF electrodes. The reactor consists of a rectangular housing 465 mm long and 80 mm high, made of 12X18H10T non-magnetic stainless steel. Plasma is generated in a stream of hydrogen ( $\text{H}_2$ ) between the active and grounded electrodes (diameters 200 mm and 110 mm, respectively) by high frequency voltage at a frequency of 13.56 MHz. The current of the working gas into the discharge space of the chamber is carried out through the gas discharge systems (three independent channels), aligned parallel to the surface of the HF electrodes. Such configuration allows in addition to hydrogen to introduce other gases into the discharge system. The introduction of additional gas during processing may allow thin films to be doped, which may control the transport properties of thin film absorbers for the PCs and will have a positive effect on their efficiency.

During the CZTS processing, a controlled magnetic field of the cork configuration was used. This configuration allows us to increase the plasma density and to reduce its heterogeneity in the center of the PCR, which may result from drift instability. Another advantage of using controlled magnetic fields in materials processing is the ability to control the bias voltage (energy of reactive ions) at all other unchanged discharge parameters. The mechanism of reducing the self-bias voltage is due to the effect of the "magnetization" of the electrons, which plays a major role in reducing their diffusion to the surface of the electrodes [5]. The low energy of reactive ions is required to minimize the scattering and radiation damage of the surface of  $\text{Cu}_2\text{ZnSnS}_4$  due to ion bombardment.

The treatment parameters were as follows:  $I_d = 2$  A,  $W = 150$  W (RF generator output power)  $P = 0.08$  mbar,  $H \approx 1.2 \times 10^4$  A/m,  $U_{\text{bias, voltage}} = 60$  V,  $\Delta t = 10$  min. Hydrogen with a purity of 99.9999% was used for treatment. The reflected power was controlled and did not exceed more than 5 watts. Test samples were processed with  $\text{Cu}_2\text{ZnSnS}_4$  films obtained at different sulphurization pressures: 950 mbar, 460 mbar, and 50 mbar (named as A, B, and C, respectively) [1].

PL studies were performed at room temperature in the wavelength range from 550 nm to 1300 nm using a Perkin-Elmer LS55 PL spectrometer with a resolution of 0.5 nm. An excitation source with a wavelength of 500 nm and a power of  $5 \mu\text{W}/\text{cm}^2$  was used for the excitation of PL.

The results of the plasma treatment of the samples show quite interesting features of the bandwidth of about 900 nm. For samples A and C there is a decrease in intensity ( $\sim 50$  and  $\sim 30\%$ , respectively), and for sample C - an increase ( $\sim 45\%$ ). These features may indicate the passivation of dangling bonds during C sample processing, which results in a decrease in the surface centers of non-radiative recombination and, consequently, an increase in the PL intensity. At the same time, we see a different effect in samples A and C: plasma treatment leads to an increase in surface non-radiation centers and a decrease in the PL intensity. Such different experimental results are probably related to the different initial defective states of the surfaces of the samples. Different states of the surface are caused by different pressures during the sulfurization stage of the film's growth.

It can be assumed that samples A and B do not have dangling bonds (or their number is small enough), so there are no objects for passivation, and treatment with hydrogen plasma results in the formation of H-clusters on the surface of the semiconductor, which can be effective non-radiative centers. At the same time, many dangling bonds are formed at 50 mbar when the film is grown. Thus, H-plasma treatment results in the passivation of these bonds and an increase in PL intensity. However, even with the passivation of the dangling bonds, the intensity value is 3 times lower than the intensity of sample B before plasma treatment.

1. I.S. Babichuk et al., Solar Energy Materials and Solar Cells 200 (2019) 109915.
2. K. Wang et al., Applied Physics Letters 97 (2010) 143508.
3. W. Wang et al., Adv. Energy Mater 4 (2014) 1301465.
4. M.O. Semenenko et al., Nanoscale Research Letters 12 (2017) 408.
5. V.V. Hladkovskiy et al., Problems of atomic science and technology 1 (2015) 156.

## SIMULATION OF FAST IONS LOSS DISTRIBUTIONS ON THE FARADAY CUPS IN JET

**V.Ya. Goloborodko**

*Institute for Nuclear Research, National Academy of Sciences of Ukraine, Kyiv, Ukraine*

The report presents a numerical code designed to analyze the experimental data obtained on a tokamak JET reactor using Faraday detectors. These detectors are placed on five pillars three each on the outer edge of the torus below the equatorial area. The design of the detectors installed on each pylon is presented in Fig.1.

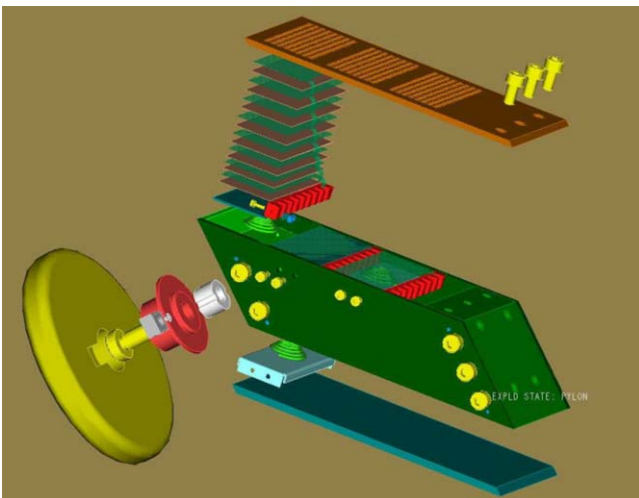


Fig. 1. Schematic illustration of a pylon with Faraday cups. Brown shows nickel foils, blue - mica plates in between, yellow - protective plate. The brown and-skin shows an ebonite cover with holes for penetration of fast lost ions.

Each Faraday detector consists of a set of nickel foils with mica layers in between. This allows us to measure the currents generated by lost fast ions with different energies because the current in each foil corresponds to the flux of ions in a specific energy range for a given type of fast ions. Each detector is

covered with a non-conductive plate in which 17x8 holes are made through which fast ions enter the foil. Each pylon is also equipped with a protective screen to counteract the heat fluxes of the main plasma. The developed numerical code takes into account the real geometry of all Faraday detectors, their position and orientation in space on the JET tokamak reactor. The code also takes into account the geometry and location of the wide poloid limiters inside the JET tokamak camera, as shown in Figure 2. The work of the code is based on the inverse of time integrating the trajectories of the orbits emanating from each hole on all detectors and pylons. As an example, the single orbit is shown in Fig. 2 and, enlarged, in Fig. 3.



Fig.2: Numerical reconstruction of the position and orientation of Faraday detectors in the JET tokamak. The position of the poloid limiters and the single trajectory are also shown

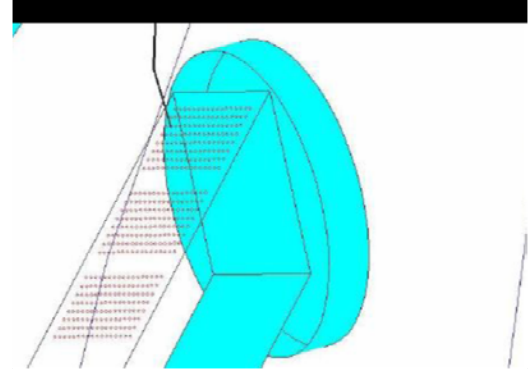
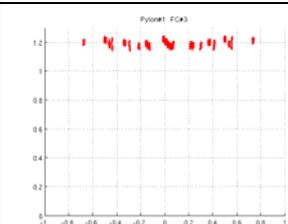
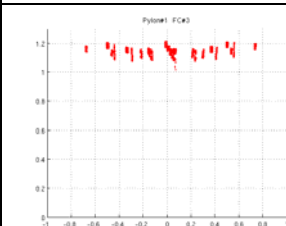
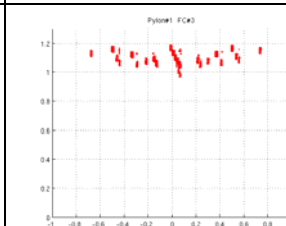
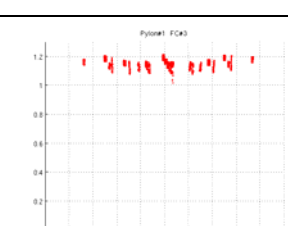
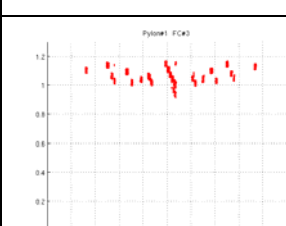
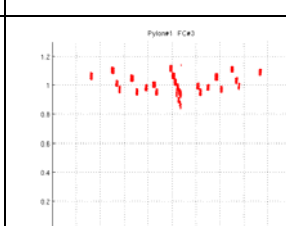


Fig. 3. Larger image of the third pylon with openings in the top cross and a single trajectory.

If the distribution of the fast ion source in the plasma is known, then by integrating it into the trajectories one can obtain streams on detectors and currents to be generated in the foils. On the other hand, if you measure the currents in the foils, you can qualitatively update the distribution of the ion source. At the same time, the question arises about the type of ions that are lost, because different types of fast ions can usually be present in the plasma. To resolve this issue, a qualitative analysis can be performed by adjusting the dependence of the minimum toroidal flow along the trajectories on the initial patch angle on the detector for different types of yo-ns. Some results of such calculations are presented in the figures in Table 1 for category # 96482,  $t = 52.4s$ , Pylon = 1, FC = 3.

E, MeV	H	D	T
0.5			
1.0			

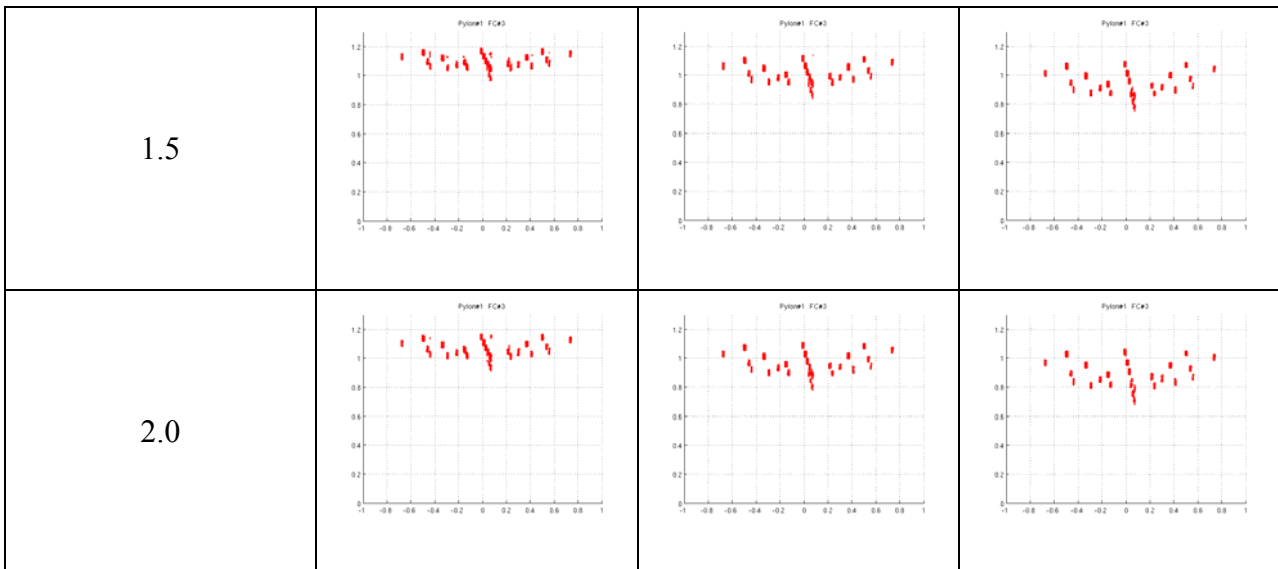


Table 1. The dependence of the minimum along the trajectories of root from the normalized toroidal flux versus the initial pitch angle for different types of fast ions at different energies in the discharge # 96482,  $t = 52.4s$  on the third Faraday detector located on the first pylon.

These figures show that trajectories with a minimum flux (red dots) greater than one do not enter the plasma and contact the structural elements. At the same time trajectories with the minimum flow are less than one enter the plasma and generate current in the foils. The more such trajectories, the more current is generated by this type of fast ions. This code was used in the analysis of the loss of fast ions on the tokamak JET, in particular, in the study of the influence of MHD perturbations on the loss of fast ions in [1, 2].

Author acknowledge for the support to V.Kiptily (CCFE) and P.Bonofiglo (PPPL).

1. V.G. Kiptily, M. Fitzgerald, V. Goloborodko et al., Nucl. Fusion **58** (1) 2018 114003.
2. V. Kiptily, P. Bonofiglo, V. Goloborodko, “Fast ion losses in high performance baseline discharges”, M18-01 meeting, 11 Feb. 2020, CCFE, Culham, UK.

## ION CYCLOTRON RESONANCE HEATING WITH SHIFTED SEPARATRIX

**Ya.I. Kolesnichenko<sup>1</sup>, H. Patten<sup>2,†</sup>, V.V. Lutsenko<sup>1</sup>, J. Graves<sup>2</sup>, T.S. Rudenko<sup>1</sup>,  
JET Contributors\***

<sup>1</sup>*Institute for Nuclear Research, Prospekt Nauky 47, Kyiv 03028, Ukraine*

<sup>2</sup>*Swiss Plasma Center, École Polytechnique Fédérale de Lausanne, CH-1015 Lausanne, Switzerland*

The Ion Cyclotron Resonance Heating (ICRH) is widely used for plasma heating in tokamaks and stellarators. During ICRH, the energy of generated waves with the frequency close to the ion gyrofrequency or its harmonic is absorbed by a group of resonant ions. This leads to acceleration of these ions and concomitant heating of the plasmadue to Coulomb collisions between the accelerated ions and thermal particles. The accelerated ions may increase fusion reactivity and can be used for studying physics of fast ions in toroidal plasmas. On the other hand, the production of accelerated ions is a drawback of ICRH. The matter is that the absorbed RF power increases mainly transverse energy of the ions, decreasing the ratio of  $V_{\parallel} / V$ , where  $V$  is the particle velocity and  $V_{\parallel}$  is its velocity along the magnetic field. This eventually leads to transformation of passing particles into trapped ones. The production of trapped energetic ions is especially a big disadvantage of ICRH for stellarators because the confinement of energetic ions with small  $V_{\parallel} / V$  is a weak point in these machines.

In connection with this, recently an idea to minimize the mentioned drawback of ICRH was advanced, and a possibility to implement it in the Wendelstein 7-X stellarator was considered [1]. A key finding in reference [1] is that there exists a simple relation between the frequency of a wave generated by antenna and the on-axis gyrofrequency of fast ions, for which trapped particles are transformed into passing ones during their acceleration, whereas passing particles do not undergo orbit transformation.

To understand the physics underlining this idea, one has to take into account that (i) the particle acceleration during ICRH occurs along characteristics in the space of Constants Of Motion (COM) of a quasilinear (QL) equation for the ion distribution function, (ii) there is a separatrix in this space, (iii) the particles approach to the separatrix during acceleration. Usually the separatrix is located in the region of trapped particles, therefore it is natural to refer to this heating as "conventional" ICRH. Passing particles moving along quasilinear characteristics can then cross the passing-trapped boundary, approaching the separatrix during their acceleration. In this case, passing particles undergo orbit transformation, becoming trapped ones. In order to avoid this, it was proposed in Ref. [1] to move the separatrix to the region of passing particles. We refer to this RF heating as *ICRH with Shifted Separatrix*, or *ICRH-SS*. During ICRH-SS the accelerated passing particles remain passing, whereas trapped particles may cross the passing-trapped boundary and become passing.

In this work, new features of ICRH-SS are revealed. The 3-D quasilinear routes of the particle acceleration and effects of Coulomb collisions are studied. A quasilinear equation for distribution function of NBI ions, which is convenient for analysis, is derived. Conditions for quasilinear flux prevailing over collisional flux caused by pitch scattering are obtained. Specific examples are considered, where parameters of the JET tokamak are used. Numerical simulations for a JET discharge are carried out using the SCENIC package, which demonstrate the formation of a population of fast ions with passing orbits during ICRH-SS, and trapped fast ion orbits for ICRH. Numerical results also indicate an increase in fast ion generation and core plasma heating performance using the ICRH-SS scheme.

‡ Present address: Department of Statistics, University of Oxford, OX1 3LB Oxford, United Kingdom

\*See the author list of "Overview of the JET preparation for Deuterium-Tritium Operation" by E. Jorin *et al* 2019 *Nucl. Fusion* **59** 112021

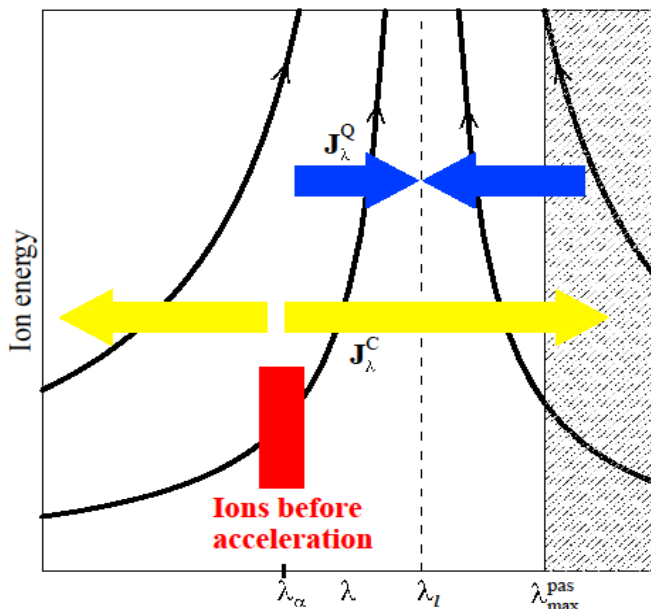


Fig.1 Sketch of quasilinear and collisional fluxes along pitch parameter  $\lambda$  during ICRH-D applied to NBI ions with the pitch parameters close to  $\lambda_\alpha$ . The separatrix is shown by dotted line. Red rectangle shows the region where fast ions are born due to NBI, arrows show directions of  $\lambda$  components of the QL flux (blue) and collisional flux (yellow). We observe these fluxes have different directions in the region  $\lambda > \lambda_l$ .

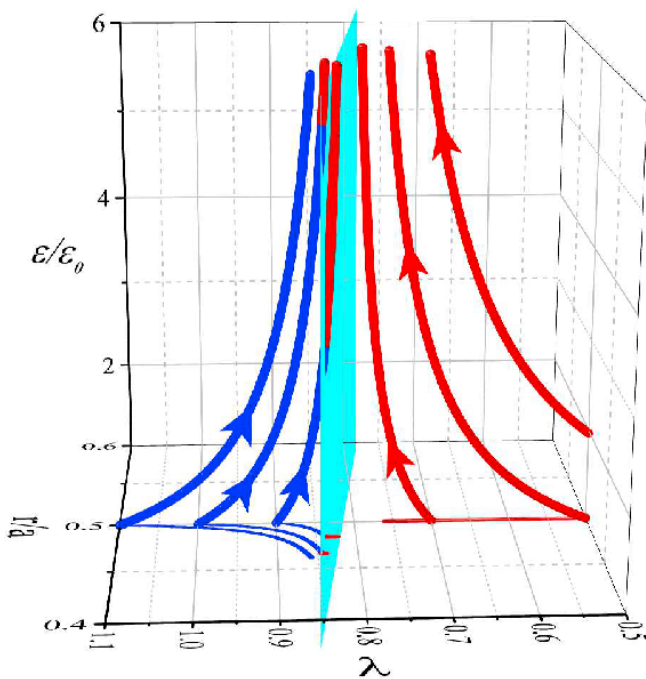


Fig.2 3-D routes of QL acceleration of particles with  $r_0/a = 0.5$ ,  $E_0 = 100$  keV, and various  $\lambda_0$ : 0.2, 0.5, 0.7 (passing particles) and 0.9, 1.0, 1.1 (trapped particles) in JET with the same parameters as in figure 1 and  $n = -27$ ,  $m = 0$  during ICRH-D. We observe that routes of trapped particles (thick blue curves) intersect the cyan plane representing trapped-passing border (except for deeply trapped particles,  $\lambda_0 = 1.1$ ) and then follow passing routes. Passing particles do not move radially, whereas trapped particles move inwards but their displacement is rather small; this is clearly seen due to shown projections of routes to the plane  $(r, \lambda)$  (red and blue thin lines for passing and trapped particles, respectively).

[1] Kolesnichenko Ya., Lutsenko V., Rudenko T., and Helander P. 2017 Nucl. Fusion **57** 066004

## NEW NONLINEAR EVOLUTION EQUATION AND ITS SOLITON SOLUTIONS IN ULTRARELATIVISTIC PLASMAS

V. M. Lashkin

*Institute for Nuclear Research, National Academy of Sciences of Ukraine, Kyiv, Ukraine*

The aim of the present work is to derive a novel evolution equation describing short-wavelength nonlinear waves in ultrarelativistic plasmas, i. e. when the plasma particle temperature significantly exceeds the particle rest mass. Despite the specific nature of the dispersion in the short-wave limit (the dispersion of "zero sound"), balance between the dispersion and nonlinearity lead to the formation of solitons. Ultrarelativistic plasmas exist in various astrophysical objects such as supernova remnants, pulsars, active galactic nuclei etc. [1], and also provide important insights about the early stage in the evolution of Universe. In laboratory conditions such plasmas can be produced in high-intensity laser fields. Most astrophysical and laboratory ultrarelativistic plasmas consist of electrons, positrons and ions (the latter, typically, are nonrelativistic).

In the short-wavelength limit, the dispersion relation for the longitudinal wave has the form

$$\omega_k = kc \left[ 1 + 2 \exp\left(-\frac{2k^2 c^2}{3\omega_p^2} - 2\right) \right] \quad (1)$$

The Landau damping is absent. There is no counterpart of the dispersion relation Eq. (1) in classical plasmas. We address a new type of nonlinear evolutional equation which is characterized by the linear dispersion (1). Obtaining of a nonlinear equation with the dispersion (1) requires an essentially kinetic description. In the Fourier space we finally get

$$\left[ \Omega - k \exp\left(-\frac{2}{3}k^2\right) \right] \Phi_{n,k} = k \exp\left(-\frac{2}{3}k^2\right) \int \Phi_{q_1} \Phi_{q_2} \delta(q - q_1 - q_2) \frac{dq_1}{(2\pi)^4} \frac{dq_2}{(2\pi)^4} \quad (2)$$

This equation strongly differs from previously known nonlinear evolution equations. Finding an analytical solution of Eq. (2) apparently does not seem possible but one can find soliton solutions numerically using the Petviashvili method. In physical variables, the soliton velocity should satisfy the condition  $v > 2 \exp(-2)c \approx 0.27c$ . The soliton amplitude grows linearly with increasing the velocity  $v$ . We note that, generally speaking,

collisions between solitons in nonintegrable models can be almost elastic under certain conditions, for instance, if the soliton amplitudes and velocities are sufficiently close to each other [2]. To study the time evolution of the solitons under their collisions, we numerically solve the nonlinear equation with the initial conditions given by a superposition of three soliton solutions with essentially different velocities. The solitons fully reconstruct their initial form without any emitting wakes of radiation, resulting only in phase shifts. The overall picture closely resembles the elastic soliton collisions in the integrable models. The elastic collisions between three solitons might suggest that equation (2) has exact  $N$ -soliton solutions and is completely integrable just like for KdV equation and some others, but this is most likely not the case. In the inverse scattering transform approach there exists a relationship between some function  $\omega(\lambda)$ , where  $\lambda$  is the spectral parameter, and the dispersion relation  $\omega(k)$  of the linearized equation. In all known cases  $\omega(\lambda)$  is the rational function of  $\lambda$  though the associated spectral problem may involve meromorphic functions of the spectral parameter  $\lambda$  like the elliptic Jacobi functions, as in the case of the Landau-Lifshitz equation. In any case, the integrability of equation (2) seems to be an open question.

6. M. H. Thoma Rev. Mod. Phys. 81 (2009) 959.
7. Yu. S. Kivshar and B. A. Malomed Rev. Mod. Phys. 61 (1989) 763.

## IMPURITY HOLES IN TOKAMAKS WITH ELECTRON CYCLOTRON HEATING OF THE HELICAL CORE

**V.S. Marchenko**

Institute for Nuclear Research, Kyiv, Ukraine, e-mail: [march@kinr.kiev.ua](mailto:march@kinr.kiev.ua)

Tungsten accumulation is one of the main challenges for successful operation of ITER and future reactors. For this reason, various techniques have been developed recently in order to mitigate such accumulation. One of such methods is the application of wave heating, in particular electron cyclotron resonance heating (ECRH) deposited close to the plasma center.

Recent 3D equilibrium calculations with central safety factor  $q \approx 1$  reveal that up to half of the ITER plasma can be helical [1]. Such helical cores with dominant mode numbers  $m/n = 1/1$  are routinely observed between sawtooth crashes in ASDEX Upgrade discharges with central ECRH [2]. The long-standing mystery of these shots, which motivated present work, is deeply hollow tungsten density profile between crashes manifested in the inverted sawteeth on the soft X-ray signals.

In the present work it is shown that ECRH-generated hot electrons can be responsible for the tungsten hole. Such electrons ‘run away’ along RF-induced quasi-linear diffusion path in velocity space and form strongly anisotropic population with banana tips accumulated at cyclotron resonance position on the magnetic surface. Equilibrium distribution function of this population can be approximated as follows:

$$f_{0e}^h \approx \frac{n_e^h}{1 + \ln(\varepsilon_{\max} / \varepsilon_{\min})} \delta(\kappa^2 - \kappa_{res}^2) (\varepsilon^{-3/2} - \varepsilon_{\max}^{-3/2}) H(\varepsilon - \varepsilon_{\min}) H(\varepsilon_{\max} - \varepsilon), \quad (1)$$

where  $\varepsilon(\kappa^2)$  is the energy (banana trapping parameter with  $\kappa_{res}^2$  corresponding to banana tip at the cyclotron resonance),  $\delta(H)$  is the Dirac (unit step) function,  $\varepsilon_{\min}$  is the runaway boundary given by  $\varepsilon_{\min} \approx T_e (v_c / v_{QL})^{2/3}$  with  $v_{c(QL)}$  thermal electron collision rate (quasi-linear diffusion rate),  $\varepsilon_{\max}$  is the high-energy cut-off due to relativistic effect [3], which is related with  $\varepsilon_{\min}$  by  $\gamma_{\max} = \gamma_{\min} + \sqrt{\gamma_{\min}^2 - 1}$ ,  $\gamma_{\min(\max)} = 1 + \varepsilon_{\min(\max)} / (m_e c^2)$ , and  $n_e^h$  is the hot electron density given by  $n_e^h \approx n_e \exp[-(v_c / v_{QL})^{2/3}]$ .

Internal kink induces  $n = 1$  toroidal ripple in the magnetic field [4], which in turn modifies the second adiabatic invariant  $J_b = \oint v_{\parallel} dl$ . This invariant serves as a Hamiltonian for super-banana motion of hot electrons

$$\begin{aligned} \frac{dr}{dt} &= \frac{q}{2\omega_{ce} r \tau_b} \frac{\partial J_b}{\partial \zeta_0} \approx v_d \frac{\xi_0}{r} \sin \zeta_0 \left[ \frac{2E(\kappa)}{K(\kappa)} - 1 \right], \\ \frac{d\zeta_0}{dt} &= -\frac{q}{2\omega_{ce} r \tau_b} \frac{\partial J_b}{\partial r} \approx -\frac{v_d}{r} \left[ \frac{2E(\kappa)}{K(\kappa)} - 1 \right] + \frac{c}{r} \frac{E_r}{B_0}, \end{aligned} \quad (2)$$

where  $v_d \approx v^2 / (2\omega_{ce} R_0) < 0$  is the electron magnetic drift velocity,  $\xi_0$  is the rigid kink displacement amplitude,  $\zeta_0$  is the field line label defined by  $\zeta = \zeta_0 + q\theta$  with  $\zeta(\theta)$  the toroidal (poloidal) angle,  $K(E)$  is the elliptic integral of the first (second) kind, and  $E_r$  is the radial electric field to be determined by ambipolarity condition  $\Gamma_e^h(E_r) = \Gamma_i$ , where  $\Gamma_i$  is the non-ambipolar kink-induced flux of thermal ions [4] and  $\Gamma_e^h$  is the flux of hot electrons, which can be calculated as follows.

Kink displacement induces perturbation of the hot electron distribution (1), which obeys banana drift kinetic equation

$$\frac{d\zeta_0}{dt} \frac{\partial f_{1e}^h}{\partial \zeta_0} + \frac{dr}{dt} \frac{\partial f_{0e}^h}{\partial r} = \langle Q(f_{1e}^h) + C(f_{1e}^h) \rangle, \quad (3)$$

where  $C(Q)$  is the collision (quasi-linear diffusion) operator, angular brackets denote bounce-average, and we have taken into account that for ‘runaways’  $\langle Q(f_{0e}^h) + C(f_{0e}^h) \rangle \approx \langle Q(f_{0e}^h) \rangle = 0$ , which yields Eq.(1). For the almost collisionless hot electrons, solution of Eq.(3) can be easily obtained replacing right-hand side by simple Krook operator with infinitesimal effective collision frequency,  $\langle Q(f_{1e}^h) + C(f_{1e}^h) \rangle \approx -\nu_{eff} f_{1e}^h$ , and taking the limit  $\nu_{eff} \rightarrow 0$

$$f_{1e}^h = -\lim_{\nu_{eff} \rightarrow 0} \text{Re} \left\{ \frac{1}{id\zeta_0/dt + \nu_{eff}} \frac{dr}{dt} \frac{\partial f_{0e}^h}{\partial r} \right\} = \pi \sin \zeta_0 \left| \frac{\beta}{\alpha} \right| \delta(\kappa^2 - \kappa_0^2) \xi_0 \frac{\partial f_{0e}^h}{\partial r}, \quad (4)$$

where  $\alpha = d\{2E(\kappa) - K(\kappa)\} / d\kappa^2 |_{\kappa^2 = \kappa_0^2}$ ,  $\beta = 2E(\kappa_0) / K(\kappa_0) - 1$ , and  $\kappa_0^2(\varepsilon, E_r)$  is the trapping parameter corresponding to resonance  $d\zeta_0/dt = 0$ , which arises due to cancellation between reversed (i.e. co-current) magnetic precession of hot electrons and positive electric drift in Eq.(2). Note that such resonance is possible only with high-field side ECRH, which is consistent with experiment [2]. Equation (4) yields for the hot electron flux [5]

$$\begin{aligned} \Gamma_e^h &= \frac{1}{(2\pi)^2} \int_0^{2\pi} d\zeta_0 \int_0^{2\pi} d\theta \int d^3v \frac{dr}{dt} f_e^h = \\ &= -\frac{\sqrt{\pi}}{2} \frac{cE_r}{B_0} \left( \frac{\xi_0}{r} \right)^2 r \frac{dn_e^h}{dr} \left( 1 + \ln \frac{\varepsilon_{\max}}{\varepsilon_{\min}} \right)^{-1} \left\{ 1 - \left[ \frac{eR_0 E_r}{|\beta(\kappa_{res})| \varepsilon_{\max}} \right]^{3/2} \right\} \end{aligned} \quad (5)$$

For parameters of the experiment [2],  $\Gamma_e^h(E_r)$  at its maximum exceeds the non-resonant thermal ion flux by more than an order of magnitude. Ambipolarity condition then reduces to  $\Gamma_e^h(E_r) = 0$ , which yields  $E_r = |\beta(\kappa_{res})| \varepsilon_{\max} / eR_0 \sim 30 \div 50 \text{ kV} / \text{m}$ . Trace tungsten must obey Boltzmann relation  $\nabla n_z / n_z = ZE_r / T_i > 0$ , which corresponds to the deep hole, consistent with experiment [2].

In summary, high-field side ECRH can be a viable option to prevent tungsten accumulation in the ITER discharges prone to spontaneous helical core formation [1].

1. A. Wingen *et al.*, Nucl. Fusion **58** (3), 036004 (2018).
2. M.Sertoli *et al.*, Nucl. Fusion **55**, 113029 (2015).
3. B. Hafizi and R.E. Aamodt, Phys. Fluids **30**, 3059 (1987).
4. S.V. Putvinskij, Nucl. Fusion **33**, 133 (1993).
5. V.S. Marchenko, Phys. Plasmas **27**, 022516 (2020).

## PECULIARITIES OF THE TRANSPORT PROPERTIES OF THERMAL PLASMA WITH IMPURITIES OF REFRACTORY METALS

**P. V. Porytsky, L. M. Sviata**

*Institute for Nuclear Research, National Academy of Sciences of Ukraine, Kyiv, Ukraine*

Refractory metals (titanium, tungsten, vanadium, tantalum, zirconium etc.) are known to widely use in a various of industrial and nuclear fusion technologies and add-ons for nuclear power plants. When operating plasma installations and building processes, the erosion process should lead to the release of metal houses into the discharge plasma.. It is more difficult to control plasma processes without an exact numerical model. Transport coefficients are the input for numerical modeling. In the case of weak ionization the Lorentzian theory it is necessary to apply for calculation of properties of multicomponent thermal plasmas [1]. But if you are in the process of ionization growth up, a number of processes will take place. These processes are needed to include into the calculations.

The calculation of transport properties of multicomponent plasma with refractory metals are provided on the base of Grad method [2,3]. It is shown that impurities have an influence on the transport properties of multicomponent plasma.

It is considered the plasma, that is in the state of a local thermodynamic equilibrium. It is possible to find the concentration of components and the rate of electronic processes in such a plasma. For low-temperature plasmas, where the local thermodynamic equilibrium is established, the concentration of electrons in this precise range is associated with the concentration of neutrals by the Saha's relations. The composition of the plasma is shown in Fig. 1. for the case of mixture of air with tantalum impurities.

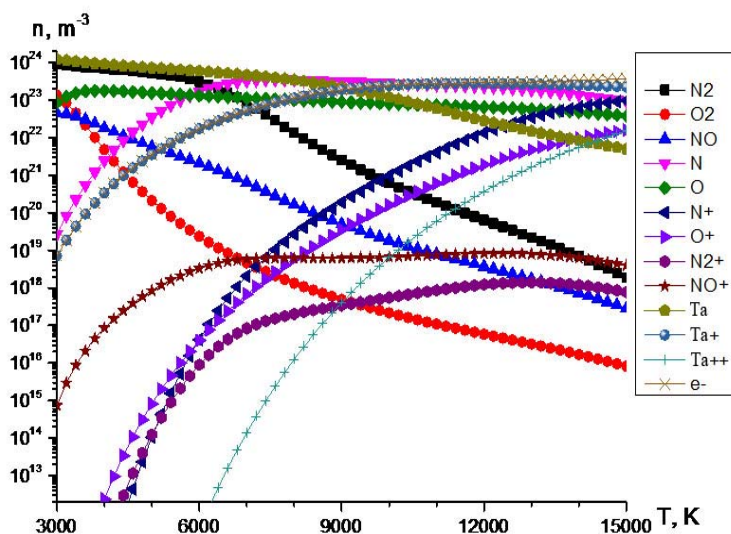


*Fig. 1. Plasma composition for the mixture of air with tantalum (molar parts is 99: 1). The others species are negligible.*

The knowledge of the plasma composition allows us to calculate the transport coefficient for a certain plasma mixture. The results of calculations for the mixture of air with tantalum are shown in Fig. 2. You can

see, that the small amount of the impurities leads to the increasable changing of plasma electronic coefficient.

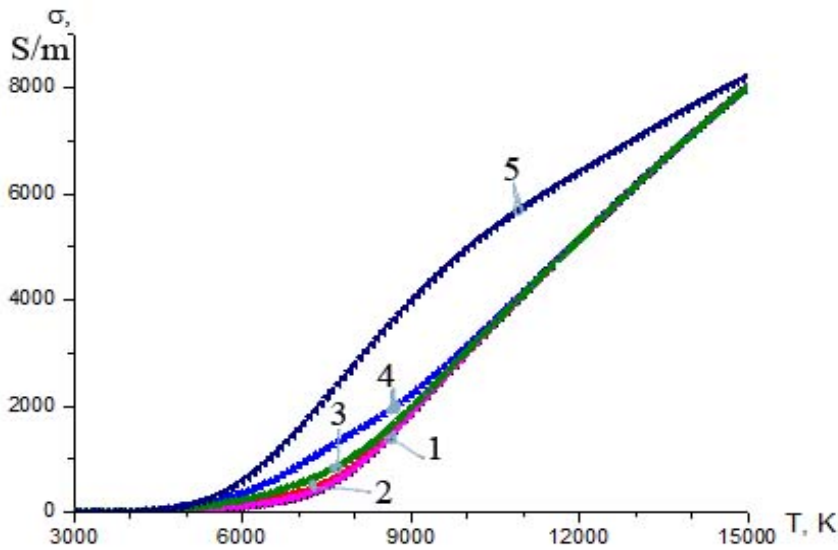


Fig. 2. Electrical conductivity of thermal plasma (pressure  $p=1$  atm) for the cases of pure air and for the cases of mixtures of air with tantalum. Curves: 1 is air, 2 is air and Ta (99,9: 0,1), 3 is air and Ta (95: 5), 4 is air and Ta (90:10), 5 is air and Ta (50 : 50).

The increase the concentration of metal in a plasma discharge are known to lead to the increasing of an electrical conductivity due to the lower value of an ionization potential of metal. However, in the case of refractory metal admixtures the increasing of metal amount in mixture can leads to corresponding decreasing of electrical conductivity. It is effect takes place due to a shape resonance at collision of electron with neutral atoms. Please note that, due to the fact that the change in electrical power is limited to metal with uncontrolled gas. In pure metal pairs, the effect is not realizable. From now on, there's a need, so that there's three offensive thinking of the change in multicomponent plasma. There are, the high concentration of metal, the ambient gas and the apparent of the shape resonance for electronic scattering on atoms.

Thus, the properties of multicomponent plasma, that having admixtures of refractory metals are determined by the character of a scattering of electrons on the metal atoms. The results of calculations are presented. It is studied the influence of the increasing of metal impurities concentration on the plasma properties. It has been shown that both the growth the plasma conductivity and the shut down of conductivity can take place in the plasma mixture. Next, it is studied the possibility the development of the control of the assigned process.

1. P. Porytsky, et al. *European Phys. Journ. D.* 57 (2010) 77..
8. H. Grad *Comm. Pure and Appl. Math* 2 (1949) 331.
9. V.M. Zhdanov. *Transport Processes in Multicomponent Plasma.* - NY: Taylor&Francis, 2002.

## ESTIMATION OF PLASMA HEATING BY ALPHA PARTICLES FROM ANALYSIS OF TEMPERATURE RECOVERY AFTER SAWTEETH CRASHES

**M. H. Tyshchenko<sup>1</sup>, Yu. V. Yakovenko<sup>1,2</sup>, H. Weisen<sup>3</sup>**

<sup>1</sup>*Institute for Nuclear Research, National Academy of Sciences of Ukraine, Kyiv, Ukraine*

<sup>2</sup>*National University of "Kyiv-Mohyla Academy", Kyiv, Ukraine*

<sup>3</sup>*Swiss Plasma Center, École Polytechnique Fédérale de Lausanne, Switzerland*

Alpha heating (heating of the bulk plasma by fusion-produced alpha particles) is seen as some kind of 'holy grail' of fusion because it demonstrates plasma self-heating by fusion reactions. 3.5 MeV alpha particles are produced primarily from the reaction  $D + T \rightarrow \alpha + n$  (14.1 MeV). The neutrons will leave the plasma and the alpha particles will be confined by the magnetic field and will heat the plasma species through collisions. The experiments to detect alpha heating were performed in the Joint European Torus (JET) in 1997 [1] during Deuterium-Tritium-Experiment campaign (DTE1). JET results were claimed to

show that alpha particle heating had been unambiguously observed.

Alpha heating detection experiments are planned during future JET DTE2 campaign. An important goal of DTE2 is to identify plasma conditions and develop scenarios allowing an unambiguous observation of alpha-particle heating. It is known that alpha heating is difficult to quantify experimentally. In order to help future attempts to demonstrate this heating in our work we will use the idea [2] of identifying a signature of alpha particle effects by looking at the recovery phase after a sawtooth crash. The aim of this work is to study the feasibility of this method, in particular, looking at deuterium discharges which had sawteeth and Ion Cyclotron Resonance Heating (ICRH) power equal to alpha particle heating and try to see whether one can recognize the contribution of the ICRH to the recovery phase after crash.

The core temperature profiles after sawtooth crash are usually flat, which reduces uncertainties (no heat transport), see Fig 1. Neglecting the Ohmic heating and the radiation loss, we can write the electron energy balance equation as follows:

$$n_e \frac{dT_e}{dt} + T_e \frac{dn_e}{dt} = q_e^{fast} + \nu_{ei}^{eq} n_e (T_i - T_e),$$

where  $T_e$  and  $n_e$  are the electron temperature and density,  $T_i$  is the ion temperature,  $q_e^{fast}$  is the power of electron heating by fast ions,  $\nu_{ei}^{eq}$  is the temperature equilibration frequency. Using experimental data, we can evaluate the contribution of fast particles to electron heating. To begin with something easy, we can start from shot #86459, with 4MW of NBI (Neutral Beam Injection) and 3MW of 3rd-harmonic D ICRH.

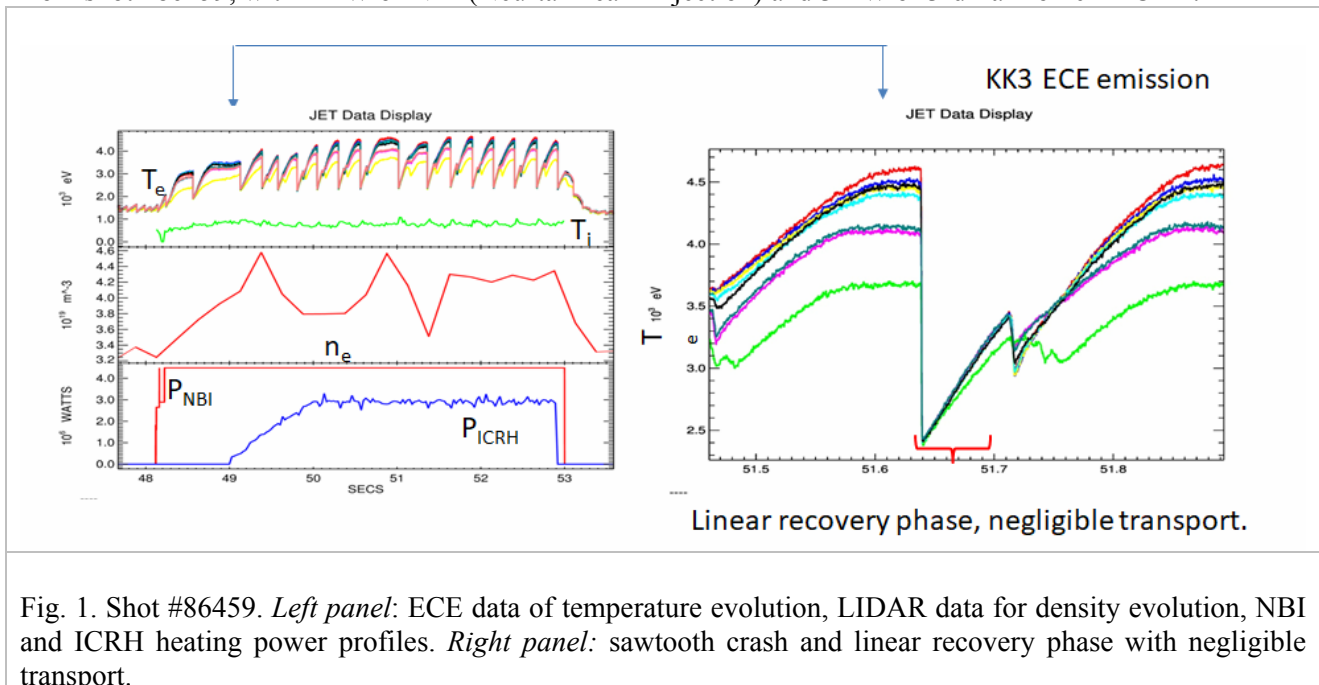


Fig. 1. Shot #86459. *Left panel*: ECE data of temperature evolution, LIDAR data for density evolution, NBI and ICRH heating power profiles. *Right panel*: sawtooth crash and linear recovery phase with negligible transport.

In this discharge the ICRH appears gradually after a brief period of NBI-only heating, which is convenient for comparison. ECE (electron cyclotron emission) data (KK3 diagnostics) was used to identify the sawtooth crash times and amplitudes. LIDAR diagnostic was used to density evaluation. For our analysis we assume that the electron and ion densities are equal. As we can see on left panel of Fig.1, from 48.2 sec to 49 sec only NBI heats the plasma, and from 49 sec to 52.9 sec both NBI and ICRH are switched on.  $T_i$  data are available only for the periphery. In our analysis we took  $T_i = T_e$ ,  $T_i = 1.2 T_e$ ,  $T_i = 0.8 T_e$ . Actually, the beam heating of electrons does not depend on  $T_i / T_e$ . But the results of our method do depend on our assumption about  $T_i$ . For different ion temperatures we estimated that reheat after switching on both NBI and ICRH is  $\sim 2.5$  times larger than after only NBI heating; and the total heating power is  $\sim 1.7$  times larger, see Fig .2.

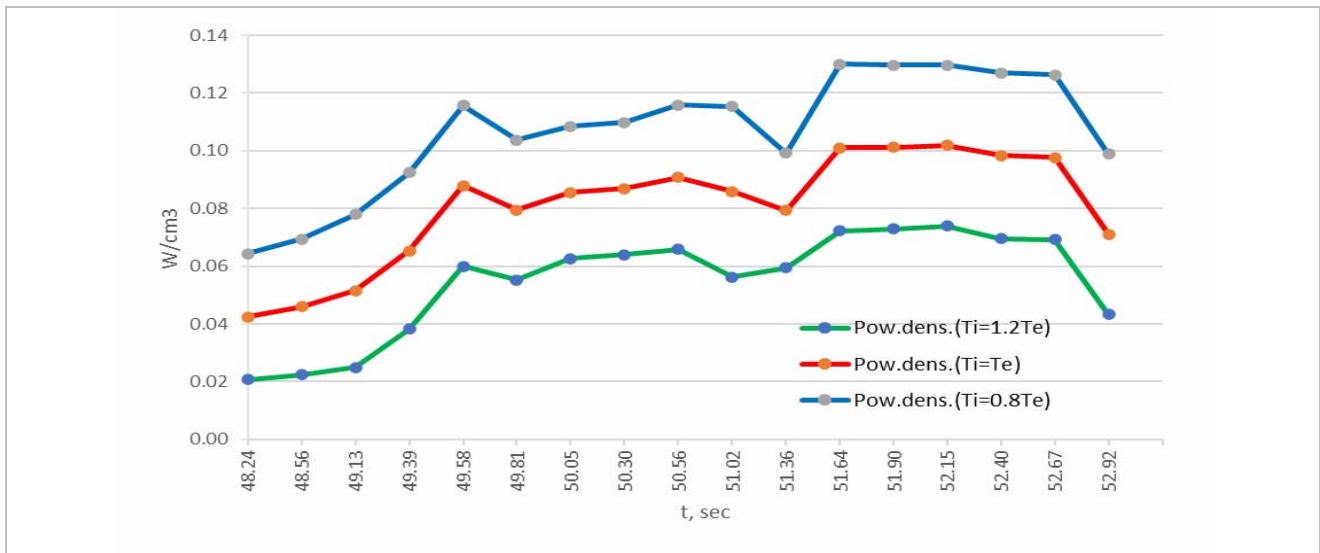


Fig .2. Power density, shot #86459; blue curve:  $T_i=0.8 T_e$  , red curve:  $T_i=T_e$  , green curve:  $T_i=1.2 T_e$

We have a qualitative agreement in discharge #86459 but  $T_i$  in the core is required for more reliable calculations. To have quantitative agreement, we need simulations with heating power not adjusted. It is worth to revisit DTE1 shots (TRANSP simulations should be available for this shoots) to see whether the proposed method of estimation of alpha heating from the plasma reheat phase after a sawtooth crash will give reliable results. The sensitivity to errors of quantities other than  $T_i$  (in particular,  $n_i$  and  $n_e$ ) and to inaccuracies in simulating the fast-ion sawtooth-induced mixing are yet to be evaluated.

1. P.R. Thomas et al. Phys. Rev. Lett. 80 (1998) 5548.
2. H.Weisen. Meeting T17-07 D8: Conditions for alpha physics, 15.03.2018.

## KINETICS OF PLASMA CHEMICAL PROCESSES IN AIR PLASMA

V.Ya.Chernyak, O.M.Tsybalyuk, O.I.Fentisova, O.D.Belenko

*Taras Shevchenko National University of Kyiv*

Today, discharges in gas flows transverse to the current channel are of particular interest. Since these discharges can generate large-aperture high-pressure non-equilibrium plasma streams for hybrid plasma catalysis of high-scale transformation of substances (sliding and rotational sliding discharges), and low-power plasma flows for small electron energies for plasma-medicine (micro discharge in vortex flow of gas).

The data used for processing was obtained using a computational package called Zero-Dimensional Plasma Kinetics solver, abbreviated ZDPlasKin, and its extension Electron Boltzmann equation solver, respectively - BOLSIG +.

The simulation was performed for dry and humid air (1% of absolute concentration) at three combinations of temperature and field strength: 1000 K and  $10^6$  V/m, taking into account reactions with vibrationally excited molecules; 1000 K and  $10^6$  V/m and 1000 K and  $2.5 \cdot 10^6$  V/m (excluding reactions with vibrationally excited molecules). The simulation time step was  $10^{-8}$  s, the simulation included 1437 reactions. They determine the change in concentrations from the time interval of  $10^{-8} \div 1$  s for 121 compounds, among which 16 negative and 13 positive ions, the electron concentration at P = 1 atm was also calculated.

The simulation was obtained using a database of chemical reactions and reaction rates of processes that take into account vibrationally excited molecules according to the Macharet-Friedman theorem [1]. The list of possible processes consisted of elementary processes of interaction of electrons with  $N_2$ ,  $O_2$  [2], and N, O, NO,  $NO_2$ ,  $O_3$  [3]; chemical reactions involving  $N_2$  [4],  $O_2$  [5]; with the participation of  $N_2O$ ,  $NO_2$ ,  $NO_3$ ,  $N_2O_5$ ,  $N_2O^+$ ,  $NO_2^+$ ,  $N_2O^-$ ,  $NO_2^-$ ,  $NO_3^-$  [6]. The list of possible processes was supplemented by

processes including H<sub>2</sub>O, H, OH, taking into account humidity. As a result of modeling, dependences of the concentration of the components on the time, as well as the rate of the reactions were obtained.

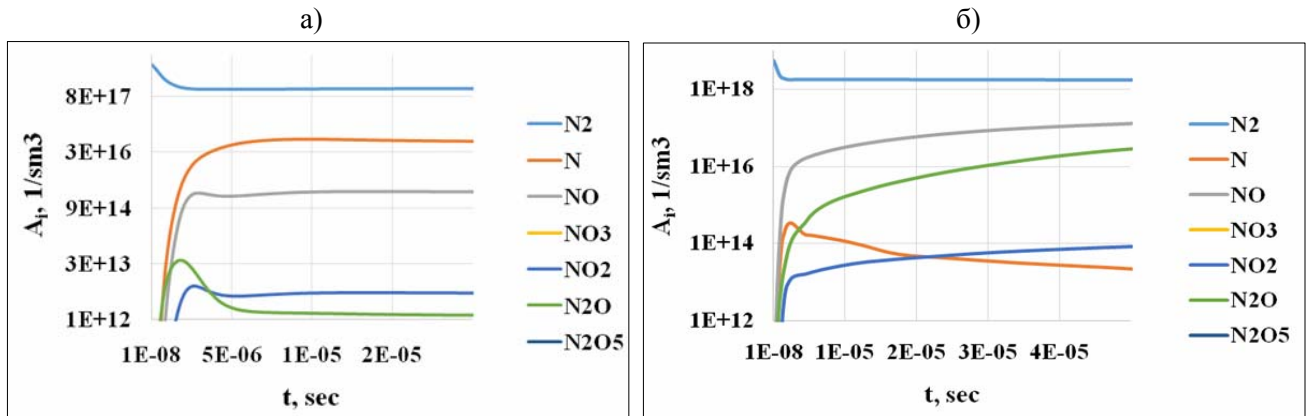


Fig. 1 Dependence of concentrations of nitrogen and its oxides on the simulation time in dry air (a) and in air with humidity of 1% at  $E = 1000 \text{ V / cm}$  and  $T = 1000\text{K}$

Numerical modeling of the kinetics of elementary processes in the plasma of dry and humid air showed that at typical values of the electric field in the plasma of micro-discharge in a rotating gas stream, the presence in the air of water leads to an increase in the concentration of nitrogen oxides in comparison with the dry air and significantly changes their kinetics. This, in turn, leads to significant changes in their composition and significantly reduces the concentration of nitrogen atoms (Fig. 1).

Researching of the settlement character of the lower vibrational levels of nitrogen molecules ( $v = 0 - 8$ ) and oxygen ( $v = 0 - 4$ ) have found that the equilibrium concentration distribution of oscillately excited oxygen molecules is much smaller than that of nitrogen molecules. In addition, this time for nitrogen molecules increases with the presence of water vapor.

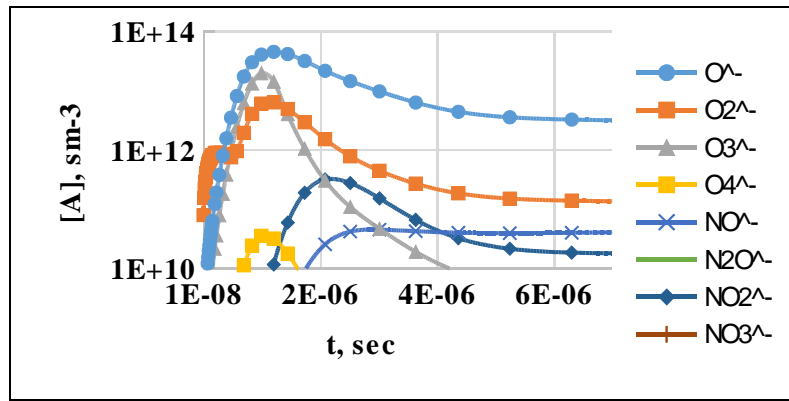
The results of the data processing showed that the amplification of the field leads to a characteristic and quantitative composition of the plasma.

Establishing a constant concentration for all plasma compounds was significantly accelerated. With a smaller field ( $10^6 \text{ V/m}$ ), some of the compounds did not even have time to reach a time when their concentration would become constant. As a result of increasing the field strength from  $10^6 \text{ V/m}$  to  $2.5 \cdot 10^6 \text{ V/m}$ , all highly concentrated compounds had a constant concentration for  $\sim 10^{-4}$  seconds of the experiment.

The results of simulations with the exclusion of reactions involving vibrationally excited molecules led to changes similar to the weakening of the electric field.

The appearance of water in the plasma-forming gas also leads to significant changes in the charged components of the plasma (Fig. 2). So in the plasma of dry air, the concentration of negative ions is substantially lower than the concentration of electrons. But the situation changes substantially in the humid air. The main charge carriers are negative ions in humid air at a time in excess of  $5 \cdot 10^{-6}$  seconds. The ratio of the electron concentration to the total ion concentration is significantly below one. The main ions in the dry air are  $\text{O}^-$ ,  $\text{O}_2^-$ ,  $\text{NO}^-$ ,  $\text{O}_3^-$  and  $\text{NO}_2^-$ , in the humid -  $\text{H}_2\text{O}_2^-$ ,  $\text{H}_2\text{O}_3^-$ ,  $\text{H}_3\text{O}_2^-$ ,  $\text{H}_2\text{O}_4^-$ ,  $\text{NO}_2^-$ ,  $\text{O}^-$  and  $\text{O}_2^-$ .

a)



b)

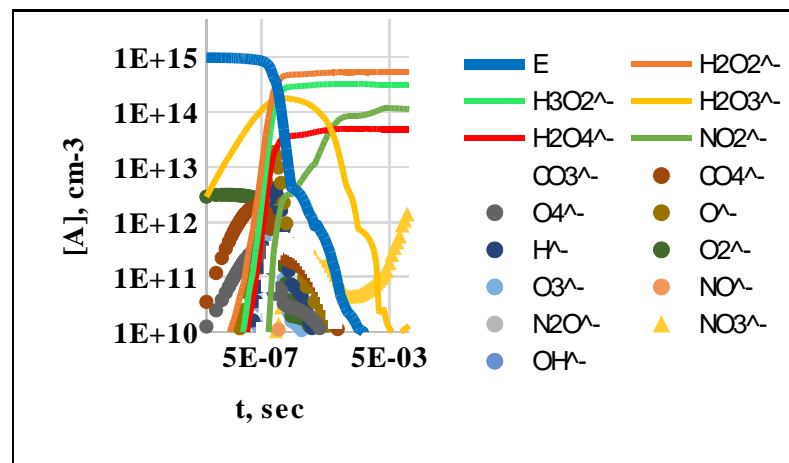


Fig. 2 Dependence of electron and negative ion concentrations on simulation time in dry air (a) and in air with humidity of 1% at  $E = 1000 \text{ V/cm}$  and  $T = 1000\text{K}$ .

1. A. Fridman, Plasma Chemistry. Cambridge: Cambridge University Press, 2008
2. M. Capitelli, C.M. Ferreira, B.F. Gordiet et al. "Plasma Kinetics in Atmospheric Gases" (2000)
3. [www.lxcat.net/Morgan](http://www.lxcat.net/Morgan)
4. <http://jilawww.colorado.edu/~avp/>
5. [www.lxcat.net/Biagi](http://www.lxcat.net/Biagi)
6. A. Flitti and S. Pancheshniy (2009) "Gas heating in fast pulsed discharges in  $\text{N}_2\text{-O}_2$  mixtures" European Physical journal of Appl. Physics 45 21001

## OPTIMISATION OF THE ION CYCLOTRON HEATING OF FUEL IONS WITH THE AIM OF ENHANCING NUCLEAR FUSION REACTIONS

**Yu. V. Yakovenko<sup>1,2</sup>**

<sup>1</sup> Institute for Nuclear Research, National Academy of Sciences of Ukraine, Kyiv, Ukraine

<sup>2</sup> National University of the Kyiv Mohyla Academy, Kyiv, Ukraine

As the cross-sections of the fusion reactions reach their maxima at suprathreshold energies, the fast ion populations produced by the neutral beam injection (NBI) and the ion cyclotron resonance heating (ICRH) in a fusion plasma can affect the burn intensity in the fusion reactor. Although the fusion reactor is to be in the regime of self-sustained fusion burn, it is assumed that some methods of additional heating will be used in the

reactor (NBI or radio frequency heating), in particular, to provide a possibility to control the burn. Natural questions arise: Is it worthwhile to use the presence of the suprathermal beams for enhancing the energetic efficiency of the reactor? What is the limit ability of this enhancement? These questions are of even more interest for sub-reactor devices, such as JET, where, in particular, a synergic effect of NBI and ICRH on the DD reaction rate was observed [1]. In earlier works the possibility to increase the reactor efficiency by applying NBI was studied [2, 3].

In this work, an optimization problem is considered, the aim of which is to find the limits of possible enhancement of the energetic efficiency of a reactor when ICRH is applied to fuel ions, or when ICRH and NBI are applied simultaneously. At present, many ICRH methods with very different properties have been developed. Therefore, it seems reasonable at the initial stage to seek the optimal heating strategy without taking its technical feasibility into account. This idea leads to the following optimisation problem: find that distribution of the quasilinear diffusion (QLD) coefficient in the fuel ion phase space, which maximally increases the reaction power at a given power absorbed by ions. As a first step, we consider a one-dimensional problem, assuming that both the distribution function of the fuel ions and the QLD coefficient depend only the particle energy (i.e., we neglect the spatial and pitch-angle inhomogeneities of these quantities).

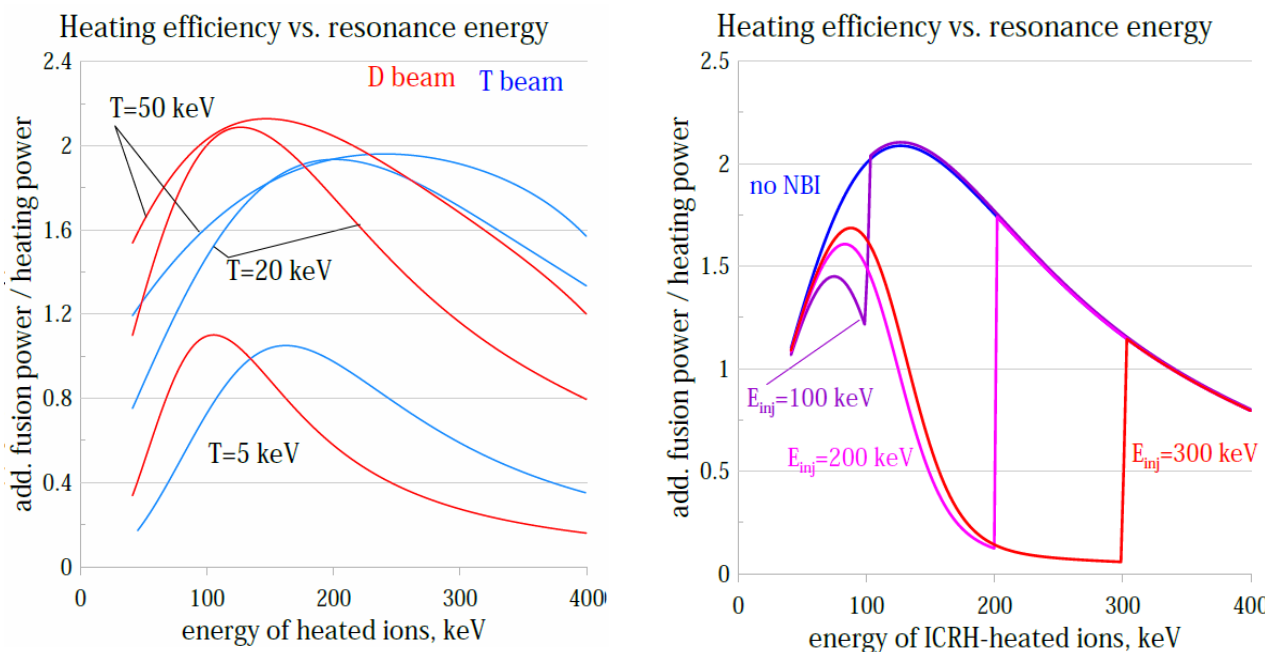


Fig. 1. ICRH efficiency versus energy of heated ions. Left panel: in the absence of NBI at various fuel temperatures ( $T$ ). Red curves, deuterium is heated; blue curves, tritium. Right panel: in the presence of NBI with various injection energies ( $E_{inj}$ ), deuterium being heated.

In Fig. 1, the dependence of the calculated ICRH efficiency on the energy of the heated ions is presented. Here the efficiency is defined as the ratio of additional fusion reaction power produced by the accelerated ion beam to the heating power. In this figure, results for the DT reaction are presented for the case when either deuterium or tritium ions are heated in the fuel mixture consisting of equal amounts of these isotopes. The situation when heating (i.e., inducing the QLD) is carried out in a narrow energy interval. One can understand from Fig. 1 that in the absence of NBI, the optimal ICRH strategy is to induce maximally strong QLD in a certain neighbourhood of the energy at which the reaction cross-section is maximum. Numerical solution of the optimization problem with the use of Pontryagin's minimum principle confirms this conclusion. The heating efficiency of the optimal strategy exceeds two; it increases to  $\sim 3$  when the tritium fraction increases to  $2/3$  and deuterium is heated and vice versa. It was found that the efficiency increases with a plasma temperature increase and weakly depends on the heating power (in other words, the reaction power has approximately linear dependence on the heating power, although the dependence of the beam distribution function on the heating power is strongly nonlinear; a similar linear dependence of the reaction rate was observed in experiments on JET [3]). It should be emphasized that this discussion concerns only the part of the energy gain produced by suprathermal particles, i.e., here we do not consider the gain from the increase of the thermal plasma temperature.

The case of the simultaneous application of NBI and ICRH was also considered (see Fig. 1). We observe that the presence of NBI, in fact, does not increase the ICRH efficiency when the injection energy does not exceed the energy of the cross-section maximum. When the injection energy is higher, the ICRH efficiency decreases. Note that the efficiency of NBI used without ICRH is about 1.5.

The DD reaction, which was studied in [3], requires a separate treatment.

This work was carried out within the framework of the EUROfusion Consortium and has received funding from the Euratom research and training programme 2014—2018 under grant agreement No 633053, from the National Academy of Sciences of Ukraine (NASU) under the project «Phenomena associated with energetic ions in tokamaks and stellarators» and the project No. PL15/19, as well as from the Science and Technology Center in Ukraine (STCU) and NASU under the project No. 6392. The views and opinions expressed herein do not necessarily reflect those of the European Commission.

1. J.M. Dawson, H.P. Furth, F.H. Tenney. *Phys. Rev. Lett.* 26 (1971) 1156.
2. D.L. Jassby. *Nucl. Fusion* 17 (1977) 309.
3. A.V. Krasilnikov et al., *Plasma Phys. Control. Fusion* 51 (2009) 044005.

## DYNAMIC OF <sup>90</sup>Sr AND <sup>137</sup>Cs ACCUMULATION IN MURINE AND SHREW IN THE CHORNOBYL EXCLUSION ZONE IN 1986–2018

**S. P. Gashchak, J.O. Makliuk**

*Chornobyl Center for Nuclear Safety, Radioactive Waste & Radioecology, Slavutych, Ukraine*

Assessment of radiation impact on wildlife inhabiting contaminated areas is referred to doses absorbed due to external and internal sources of irradiation. Normally actual content of radionuclide (RN) incorporated into organism and external dose rate allow estimating total dose. However, potential effects often depend on long-term history of irradiation, over several generations. Therefore knowledge of the long-term history of irradiation have undoubted value. The given report considers <sup>90</sup>Sr and <sup>137</sup>Cs uptake by murine rodents and shrews, common study objects in Chernobyl. These RN are main radiation contributors in Chernobyl over the last 20–25 years as most of other RN either completely (or considerably) decayed or have very low radiation significance for biota [1].

In theory amount of RN directly defines dose rates around, and the later would follow changes of the first. Roughly if no additional completion, the dose rate repeats generic trend of RN decay. However from the very beginning after the accident irregular changes both of the external dose rate and contamination of the animals were observed while the RN were decaying on classic lows [2]. Reasons of such contradiction were in migration of the RN, transformation of their physical and chemical forms, changes of bioavailability in soil, significant seasonal changes of foodstuff, weathering, etc. [3]. The first analysis of long-term changes of RN transfer in ‘soil – animal’ system was undertaken for 1986 – 2005 period [3] on the base of own and published data. Contamination of the animals was specified referring whole body activity concentration (kBq/kg) to the RN deposition at the study site (kBq/m<sup>2</sup>), i.e. transfer factor (TF). Such approach allowed to combine data obtained on territories different on contamination, and assess long-term changes of the transfer excluding RN decay. The given report continues the analysis, considering 2007 – 2018 period as well.

Following this analysis, changes of RN transfer in ‘soil – animal’ system had several specific stages. The first one (I, Fig. 1) lasted since 1986 till mid of 1990s when TF both <sup>90</sup>Sr and <sup>137</sup>Cs decreased on two orders of magnitude as a result of significant RN immobilisation in soil and transfer to the deeper layers [4]. Then, in 1996–2002 both <sup>90</sup>Sr and <sup>137</sup>Cs exhibited reverse growth of the uptake (II, Fig. 1) as a result of the ‘hot’ particle destruction reported for that period [4]. Regardless considerable seasonal and year variability the total reverse growth of average TF values reached one order of magnitude. Over the next 2003–2008 period (III, Fig. 1) the repeated decrease of took place. Evidently it was caused by further immobilisation of RN earlier leached from the destroyed ‘hot’ particles. Since 2008–2010 the reverse growth of TF <sup>137</sup>Cs was taking place, and increased on an order of magnitude by 2018; likely TF <sup>90</sup>Sr did not grow so much (IV, Fig. 1). The only what could explain the later increase is global changes of the climate. On the data of the Chernobyl meteostation, average temperature of air in May-September of 2008–2018 exceeded average value for the last 30-year period, and continues to grow (Fig. 2). At that sum of precipitation year-by-year decreases. Previously we reported of positive correlation between average temperature of air and RN TF [3]; perhaps this is an effect of RN ‘concentration’ in food of herbivorous animals at higher temperature. Though the lack of precipitation and water in ecosystems is getting obvious, while relation between precipitation and RN TF in the system ‘soil–plant’ is well-known [5], influence of the precipitation on RN transfer in ‘soil – animal’ system is not noted. Such contradiction could be explained by complex multi-factorial impact on RN migration in trophic chains, as well as heterogeneity of the initial data (different sites, soil conditions, species composition, seasonal changes of the food composition, etc.).

Thus, over the 2008–2018 period, the growth of RN transfer in ‘soil–animal’ system was observed. It reached values similar as 20 years ago. However due to RN decay (in 2018 – only 46–48% of initial deposits), contamination of animals (specific activity) was in ca. 10–15 times less than soon after the accident. Over the 30-year period it grew up and dropped down several times within two order of magnitude range. Therefore assessing radiobiological effects researchers have to refer to the particular radioecological conditions of the study period and study sites.

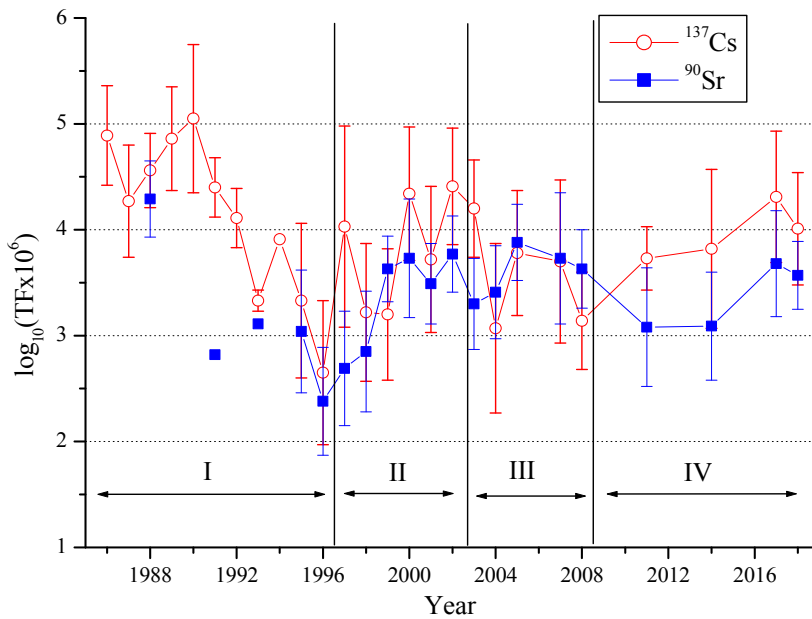


Fig. 1. Dynamic of the RN transfer in system 'soil – animal' in the Chernobyl exclusion zone in 1988–2018. I, II, III and IV – conditional periods (see text),  $\text{mean}_{\text{geom}} \pm \text{SD}_{\text{geom}}$

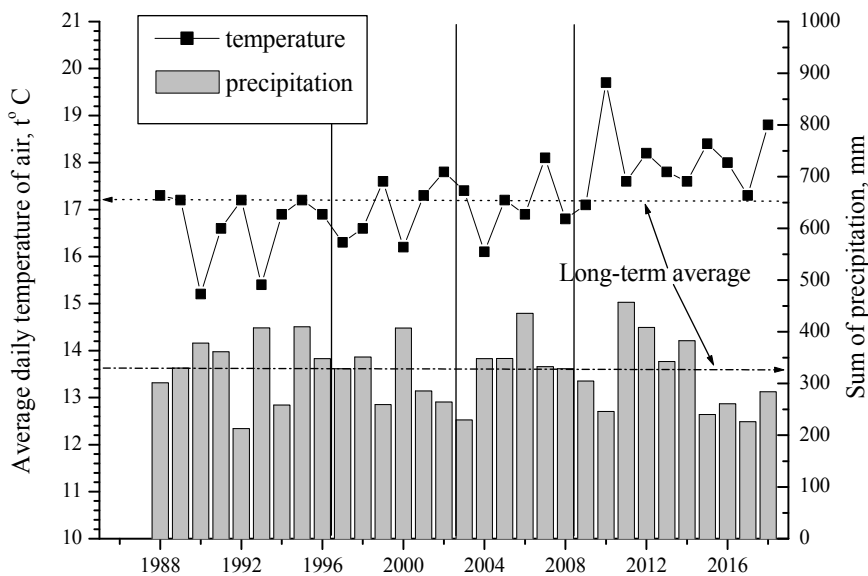


Fig. 2. Average daily temperature of air (°C) and sum of precipitation over May–September in 1988–2018 (on the data: Chernobyl meteorological station)

1. Beresford N.A. et al. (2010) Predicting the radiation exposure of terrestrial wildlife in the Chernobyl exclusion zone: an international comparison of approaches. *J. Rad. Prot.* 30: 341-373.
2. Baryakhtar V.G. et al. (2003) Problems in small mammals radioecology. *Environmental Sciences and Pollution Research*. Special Issue 1: 95–106
3. Makliuk Y. A. et al. (2007) Long-term dynamic of radioactive contamination ( $^{90}\text{Sr}$ ,  $^{137}\text{Cs}$ ) of small mammals in Chernobyl zone. *Ecology*. 38 (3): 198–206. (Russian)
4. Ivanov Yu.A., Kashparov V.A. (2003) Long-term dynamics of the radiological situation in terrestrial ecosystems of the Chernobyl Exclusion Zone // *Environ. Scien. Pollut. Research*. Spec. Iss. No. 1: 13–20.
5. Shcheglov A.I., Tsvetnova O.B., Klyashtorin A.L. (2001) Biogeochemical migration of technogenic radionuclides in forest ecosystems. M.: Nauka, 235 p.

## IRRADIATION METHOD OF INCREASING ANTITUMOR EFFICACY OF CONIUM

**M.A. Zabolotnyy<sup>1</sup>, G.I. Dovbeshko<sup>2</sup>, G.I. Solyanik<sup>3</sup>, L.N. Kirkilevskaya<sup>4</sup>**

<sup>1</sup>*Taras Shevchenko National University of Kyiv, Ukraine;*

<sup>2</sup>*Institute of Physics of NASU, Kyiv, Ukraine;*

<sup>3</sup>*R.E. Kavetsky Institute of Experimental Pathology, Oncology and Radiobiology of NASU, Kyiv, Ukraine*

<sup>4</sup>*Kiev medical University, Kyiv, Ukraine*

**Introduction** To date, there is a steady tendency towards individualization of treatment of cancer patients, which is associated with the individual sensitivity of the body to therapeutic agents (which may vary 10-40 times) and the selectivity of their antitumor activity. The latter is manifested in the fact that the difference between the dose of antitumor drugs, which provides effective inhibition of the tumor process, and the dose that causes significant damage to normal organs and tissues of the body, is small enough. It is also important that the significant contribution to the variability of the body's sensitivity to antitumor drugs makes the resistance of malignant tumors. Actuality of researches is conditioned by the necessity of creation of non-destructive physical methods of modification of antitumoral preparations for the increase of their therapeutic efficiency. Recently, a method has been proposed for modifying the optical and therapeutic characteristics of doxorubicin (an anthracycline line) by using preliminary irradiation of the solvent with high-energy electrons [1]. The role of the modifying factor was assigned to the bubstons (nanobubbles of air surrounded by a double electric layer). In this work, we study the possibility of modifying the alkaloid line using the example of the anti-tumor drug Conium.

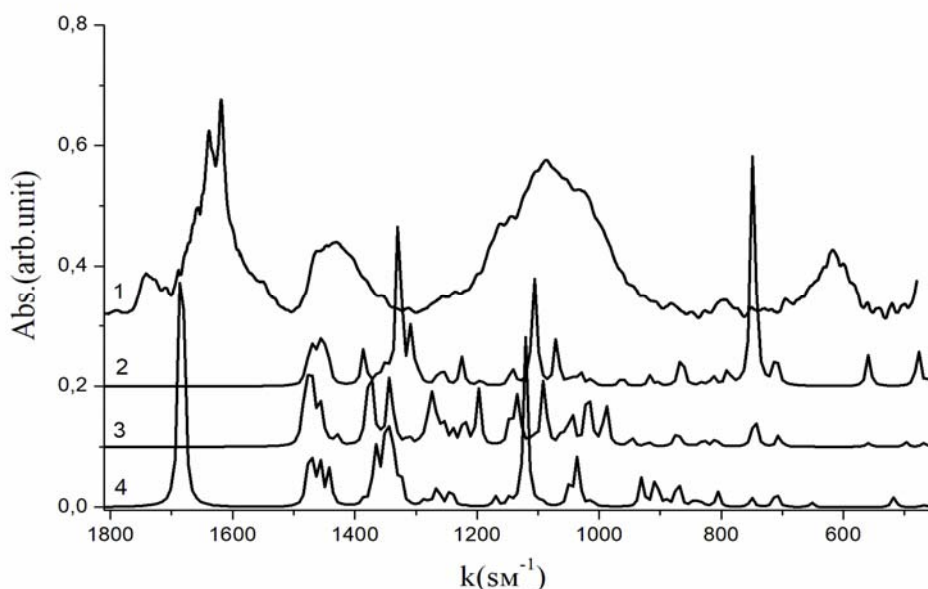
**The of research objective** - is the study and analysis of influence of previous electrons irradiation of solvent on optical and therapeutic properties of solution of medicinal preparations of anthracycline and alkaloid rows for the increase of their efficiency.

**Materials and methods** The measurements used drugs doxorubicin ("Pharmacia Italia SpA", Italy) and Conium (Weleda, Germany). Drug Conium, contains a number of alkaloids, the main of which are Coniin ( $C_8H_{17}N$ ), N-Methylconiin ( $C_9H_{19}N$ ),  $\gamma$ -Conitsiin ( $C_8H_{15}N$ ), Conhydrin ( $C_8H_{17}NO$ ) and Pseudoconhydrin ( $C_8H_{17}NO$ ) [3]. As a solvent, a physiological solution of 0.9% NaCl ("Novofarm-Biosynthesis", Ukraine) was used. All samples for recording IR spectra were prepared in KBr tablets. The IR spectra were recorded using a Bruker IFS 66 IR Fourier spectrometer (Germany) in transmission geometry. The accuracy of the determination of the wave number was  $0.2\text{ cm}^{-1}$ , the accuracy of determining the transmittance of 0.1%. The saline collected into sterile 20 ml medical syringes was irradiated with 2.0 MeV electrons using the ILU-6 linear accelerator. Measurement was carried out not later than 10 days after irradiation of the physiological solution. The sample temperature was within the range of 20-25 degrees Celsius. The registration and processing of the spectra was carried out using the OPUS 5.5 program.

**Results** The calculations of the dipole moments and the energy of the ground states of the alkaloid's molecules (Table 1) showed that three alkaloids ( $\gamma$ -Conitsiin, Conhydrin, Pseudoconhydrin) of the six studied have higher values of dipole moments, which can probably lead to the formation of adducts involving of these molecules.

The name of alkaloid	Dipole moment, D (Debye)	Energy of the basic state, Eh (Energy Hartree)
Coniin	0.84	-371.8857
N-Methylconiin 1	0.4628	-411.7231
N-Methylconiin 2	0.4713	-412.1554
$\gamma$ - Conitsiin	1.83	-369.2145
Conhydrin	1.30	-448.1843
Pseudoconhydrin	2.39	-451.1421

Of particular interest is  $\gamma$ -Conitsiin, the only of the alkaloids that make up the Conium, which has a double bond connecting the N and C atoms. The presence of a double bond in the  $\gamma$ -Conitsiin may indicate the possibility of the formation of stable chemical complexes by it. For the molecules of each of the alkaloids, geometry optimization was performed and the IR spectra were calculated, and a scale factor of 0.9720 was used for the spectra Fig.1.



During optical studies, the spectral dependences of absorption ( $A$ ) of solutions of therapeutic drugs in non-irradiated and previously irradiated by electrons of a solvent in the infrared light range were measured. The spectra were determined in the wave vector range ( $k$ ) [ $4 \cdot 10^2 - 2 \cdot 10^3$ ]  $\text{cm}^{-1}$ . The energy of the irradiating electrons was 2.0 MeV. Analysis of the absorption spectra of solutions of alkaloids obtained using irradiated and non-irradiated solvents showed, the addition of an irradiated solvent to a different dose of absorbed high-energy electron irradiation affects the positions of the maxima of the absorption bands of the Conium. Such a displacement of the absorption lines of the horse in the oscillating region of the IR spectrum is evidence of a change in its conformational state, due to interaction with the molecules of the irradiated solvent. The values of the dose of absorbed ( $I$ ) irradiation were 5, 10, 15, 20, 40, 50, 60, 80 kGy.

Correlation analysis of Pearson [1] was used in the comparative analysis of absorption ( $A(k, I)$ ) of solutions of antitumor drugs. The interval  $\varepsilon$  is evenly divided by 1200 points. The study of the ability of high-energy electron irradiation of a physiological solution, as a solvent of a drug, to modify the pharmacological activity of the antitumor drug Conium was investigated *in vitro* using the line of cancer cells of the lung carcinoma of Lewis (LLC). It was recorded that LLC incubation for 24 hours in the presence of Conium, dissolved in a non-irradiated saline solution, resulted in a concentration-dependent decrease in the number of living cells.

**Conclusions -1.** Thus, preliminary radiation irradiation of the solvent, without substantially changing the medications (in all cases, the correlation coefficient exceeds the critical value), changes some of its properties in the oscillation range, which significantly depends on the conformational state of the molecules. **2.** The ability of high-energy electron irradiation of a solvent to increase the pharmacological activity of antitumor drug Conium (especially in the range of low concentrations of drugs) is established. **3.** It has been established that the conformations of the molecules of alkaloids with the lowest energy have the maximum possible linear dimensions and the smallest values (for stable states) of the dipole moment.

## References

1.L.I. Aslamova, M.A.Zabolotnyy, G.I, Dovbeshko, G.I.Solyanik, 14<sup>th</sup> International conference Medical Physics in the Baltic States 2019, 7 – 9,11, 2019, Kaunas, Lithuania, Proceedings of International Conference “Medical Physics 2019”, p. 151 – 152.

**THREE DECADES SINCE THE CHORNOBYL ACCIDENT:  
MALIGNANT NEOPLASMS INCIDENCE IN AFFECTED GROUPS OF UKRAINIAN  
POPULATION.**

<sup>1</sup>Prysyazhnyuk A.Ye., <sup>1</sup>Bazyka D.A., <sup>1</sup>Gudzenko N.A., <sup>1</sup>Fuzik M.M.,  
<sup>1</sup>Trotskyuk N.K., <sup>2</sup>Fedorenko Z.P., <sup>3</sup>Ryzhov A.Yu., <sup>2</sup>Gulak L.O., <sup>1</sup>Babkina N.G.,  
<sup>1</sup>Khukhrianska O.M., <sup>2</sup>Goroh Ye.L., <sup>1</sup>Danevich S.A.

<sup>1</sup>State Institution “National Research Center for Radiation Medicine, National Academy of Medical Sciences of Ukraine” 53, Melnykov str., Kyiv, 04050, Ukraine

<sup>2</sup>National Cancer Institute, 33/43 Lomonosov str., Kyiv 03022, Ukraine

<sup>3</sup>Taras Shevchenko National University of Kyiv, Volodimirska str. 60, Kyiv, 01033, Ukraine

**The goal** of the study was to define levels and trends dynamic of the malignant neoplasms incidence at whole and those of specific sites in groups of Ukrainian population affected by the Chernobyl accident during a long period of observation.

**Materials and methods.** Study groups were the Chernobyl accident recovery operation workers (CRW) of 1986-1987 years of participation, evacuees from the restricted 30-km zone around the NPP and residents of the territories of Ukraine most contaminated with radionuclides. Periods of observation were 1994-2017, 1990-2017 та 1980-2017 accordingly. Analysis was carried out with the standard methods of descriptive epidemiology: calculation of crude, age-specific and age-adjusted incidence rates with their 95% confidence intervals and standard errors ( $p=0.05$ ).

**Results, discussion and conclusions.** Malignant neoplasms incidence in total exceeded national level only in CRW group. The incidence either in evacuees or in residents of the most contaminated territories did not exceed national indices. At the same time in CRW group the significant increase of the malignant neoplasms standardized incidence rate (SIR) - 106,7 % (95% ДІ 104,9–108,5) was defined.

Time trends of the incidence rates in population of contaminated territories were similar at whole. Average annual cancer incidence rates increased until beginning of 90<sup>th</sup>. Since 1993 decrease of rates until 2005 occurred. Since 2006 the increasing trends was observed there again. Such dynamics were characteristic both for Ukraine in total and for the most contaminated with radionuclides districts (rayons).

Results of our study did not suggest a radiation associated excess of leukaemia or lymphoma in population of the territories most contaminated with radionuclides.

At the same time statistically significant dose dependent leukaemia risk increase in a cohort of 110 000 CRW was observed in a frame of Ukrainian- American project. The excess relative risk (ERR) at 1 Gy of exposure in 1986-2000 was estimated to be 3,44 (95% CI 0,47 - 9,78,  $P < 0,01$ ) [Romanenko A.Y., 2008]. Extending the observation period to 2006 inclusive, led to a decrease in risk estimates to 1.26 (95%CI: 0.03, 3.58,  $p=0,01$ ) [L. B. Zablotska, 2013].

Significant excess of thyroid cancer incidence above the national level was defined in each of the main groups of affected population including 4.4-fold increase in recovery operation workers, 4.0-fold in evacuees and 1.3-fold in residents of the territories most heavily contaminated with radionuclides. It might be caused by radiation exposure of thyroid due to radioactive iodine fallouts. Excess of thyroid cancer incidence was observed not only in children and adolescents but in adults as well. The excess tended to increase over time.

Significant increase of breast cancer incidence rate was registered in females participated in recovery operation works in 1986-1987.

The estimates obtained, on the whole, statistically correspond to those determined for the survivors of the atomic bombing of Hiroshima and Nagasaki (W. L. Hsu et al, 2013).

Because of significant difference between latent periods of different radiation related tumors, attention should be drawn not only to thyroid, breast cancers and leukemia, but also to lung, stomach, colon, ovary, urinary bladder, kidney cancers and multiple myeloma.

#### References

1. The Ukrainian-American study of leukemia and related disorders among Chernobyl cleanup workers from Ukraine: III. Radiation risks [Text] / A. Ye. Romanenko, S. Finch, M. Hatch et al. et al. // Radiation Research. – 2008. – Vol. 170. – P.711 – 720.
2. Radiation and the Risk of Chronic Lymphocytic and Other Leukemias among Chernobyl Cleanup Workers [Text] / L. B. Zabloeska, D. Bazyka, J. H. et al. // Environmental Health Perspectives - 2013. – Vol. 121. – No.1 – P. 59-95.

3. Epidemiology of late health effects in Ukrainian chornobyl cleanup workers / D. Bazyka, A. Prysyzhnyuk, N. Gudzenko et. al. *Health Phys.* 2018. Vol. 115(1). P.161–169.
4. The incidence of leukemia, lymphoma and multiple myeloma among atomic bomb survivors: 1950–2001. W. L. Hsu, D. L. Preston, M. Soda et al. *Radiat. Res.* 2013. Vol. 179 (3). P. 361–382.

## INVESTIGATION OF NaX AND TiO<sub>2</sub> RADIATION RESISTANCE

**H. Vasylveva<sup>1</sup>, I. Mironyuk<sup>2</sup>, V. Tryshyn<sup>3</sup>, M. Strilchuk<sup>3</sup>, H. Dovbeshko<sup>4</sup>, V. Neymash<sup>4</sup>**

<sup>1</sup> *Uzhgorod National University, Uzhgorod, Ukraine*

<sup>2</sup> *Vasyl Stefanyk Precarpathian National University, Ivano-Frankivsk, Ukraine*

<sup>3</sup> *Institute for Nuclear Research of NAS Ukraine, Kyiv, Ukraine*

<sup>4</sup> *Institute Physics of NAS Ukraine, Kyiv, Ukraine*

The challenges in working on the scientific problems of determining the age of strontium-yttrium  $\beta$ -source, may be divided into two main areas: 1) transfer of the active part of sources to the dissolved state with keeping the initial isotope ratio constant; 2) separation of strontium, yttrium and zirconium isotopes with the highest possible accuracy. The both stage of this work related with using adsorbents.

The first stage is related to using the adsorbents as a carrier. Commercial synthetic NaX zeolite is the basis of active part of some strontium-yttrium sources for example “БІС”, and relates to faujasite topology (FAU). NaX is the first material with adsorption properties, which is the object of nuclear forensics. NaX is synthesized according to technique TU 38.10281-88. The main raw material of NaX is kaolin. NaX lattices have a network of pores diameter of nearly 7.4 - 8 Å. In NaX, ‘X’ mean that Si/Al ratio in zeolite equal 1-1.4. The disadvantage of this adsorbent, according to our experimental data, and the results described in the literature [1], is the low chemical resistance in acidic medium. Cations of Mg<sup>2+</sup>, Al<sup>3+</sup>, Na<sup>+</sup> are recovering from the zeolite’s structure in acid medium.

Therefore, we suppose, that the zeolite with radioactive strontium (i.e. active part of radioactive source) is stabilized by heating to temperatures of 1000 °C and above. The zeolite loses its structure and turns into an amorphous substance, like glass, under heating to temperatures of 1000 °C and higher. In this case, SrAl<sub>2</sub>Si<sub>2</sub>O<sub>8</sub>-type compounds may be formed. There are a few articles about this, but a lot of scientific reports in period of 1970-1996 years indicate a large number of investigations in this science direct.

The main characteristic, which caused the using NaX as carrier of <sup>90</sup>Sr, was its radiation resistance. Radiation resistance is related to thermal stability.

Basically, radiant stability is the invariability of the structure and chemical properties of the material at high doses of radioactivity. The high radiation resistance of NaX is confirmed by its high thermal stability. Only when heated to temperatures above 800 °C and lasting at least 6 hours in its structure changes begin.

Regarding the second area of our research, it should be noted that adsorbents that can be used to separate isotopes with mass 90 should have chemical and radiation resistance. The separation of isotopes in the production of radio-pharmaceutical preparations, or in radiochemistry is carried out, preferably, in an acidic environment.

Extremely high chemical and thermal stability is characteristic of TiO<sub>2</sub>-based adsorbents [2].

In our work, we investigated the radiation resistance of adsorbents based on titanium dioxide.

<sup>90</sup>Sr with (T<sub>1/2</sub> = 28 years) and its daughter radionuclide <sup>90</sup>Y (T<sub>1/2</sub> = 64 h) - intense  $\beta$ -emitters in the strontium-yttrium source. The maximal energy of  $\beta$  particles of <sup>90</sup>Sr is 0,6 MeV; the maximal energy of <sup>90</sup>Y higher 2,2 MeV. The average energy of the  $\beta$  particles is about 1 MeV. After 5 half-lives of <sup>90</sup>Y, there is a secular equilibrium between the parent <sup>90</sup>Sr and daughter <sup>90</sup>Y. And if parent strontium is bonded in the matrix of the adsorbent, then the adsorbent will be affected by the  $\beta$  particles of both strontium and daughter yttrium.

A  $\beta$  particle accelerator was used to model this situation. Radiation resistance of TiO<sub>2</sub> samples was investigated on a resonant linear accelerator of  $\beta$  particles “Argus” Institute of Physics, NAS of Ukraine.

The average energy of the electrons generated in the pulse mode was 1 MeV. The minimum radiation dose of the tested samples was 5 kSv, and the maximum 50 MSv.

180 minute after irradiation, adsorption of strontium ions by irradiated samples was investigated. Since stable strontium isotopes were used, the initial and residual concentrations of this element were determined by chemical methods using the standard procedure described, for example, in [2]. The study of adsorption of Sr<sup>2+</sup> with an irradiated sample was also performed as a control experiment. The adsorption value of Sr<sup>2+</sup> upon irradiation with TiO<sub>2</sub> doses of 5 kSv - 50 MSv did not changes and was of 51.39 ± 3.9 mg/g (the condition of the experiment was L:S=100; pH=6,5-7; the initial concentration of the strontium 0,01M). The distribution coefficient (K<sub>d</sub>) also remained unchanged, and equal 1,2 · 10<sup>4</sup> ml/g. The results indicate high radiation stability of the tested TiO<sub>2</sub> samples. The calculation by Monte Carlo method shows that, investigated adsorbent does not change its basic properties at a dose equal to the dose generated by 270 mg <sup>90</sup>Sr during 10

years. It has been noted, that 270 mg/g is the maximum adsorption capacity of the sample in a neutral medium.

This fact confirmed the radiation resistance of TiO<sub>2</sub>-based adsorbents and the prospect of their use in nuclear forensics for the separation of <sup>90</sup>Sr-<sup>90</sup>Y-<sup>90</sup>Zr. That is, the next generation of adsorbents that can be useful in nuclear forensics are TiO<sub>2</sub>-based adsorbents.

1. Reza Sadeghbeigi, 2012. Fluid Catalyst Cracking Handbook (third edition). Chapter 4, p. 87-115 ISBN 978-0-12-386 965-4. <https://doi.org/10.1016/C.2010-0-67291-9>
2. Mironyuk I., et al., 2019. Effects of chemisorbed arsenate groups on the mesoporous titania morphology and enhanced adsorption properties towards Sr(II) cations, Journal of Molecular Liquids, 282, 587 <https://doi.org/10.1016/J.MOLLIQ.2019.03.026>.

## **BIOGEOCHEMICAL MONITORING OF TECHNOGENIC POLLUTION OF THE SURFACE AIR BY RADIONUCLIDES AND HEAVY METALS IN THE MOST POLLUTED AREAS OF KYIV**

**M. Hryhorenko, O. Zhukov, I. Maliuk, V. Tryshyn**

*Institute for Nuclear Research, National Academy of Sciences of Ukraine, Kyiv, Ukraine*

Environmental pollution, including atmospheric air, heavy metals, and radioactive substances, is one of the most pressing environmental problems today.

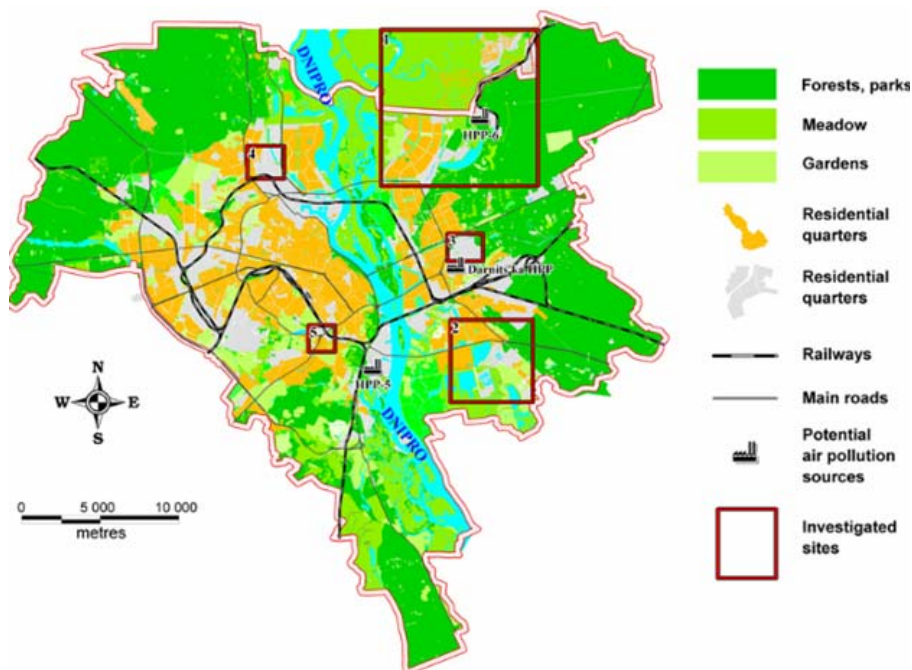
The biological monitoring method has become one of the most widely used for monitoring of surface air pollution. The essence of the method is to analyze the concentration of toxic substances accumulated by the tissues of plant or animal objects (biological monitors) selected within the explored area.

The advantages of this method include the possibility of covering vast territories by area, the ability to study the dynamics of pollution and to carry out retrospective assessments, as well as acceptable economic indicators. Besides, the use of biomonitoring in conjunction with modern multi-elemental analysis methods allows for high monitoring sensitivity, which is essential given the extremely low levels of permissible concentrations of heavy metals in the air. Appropriate analysis and interpretation of the obtained data allow us to identify, as a result, the sources of pollutant emission and to identify the halos of contamination of the surface air layer.

The purpose of this work is to apply the biogeochemical monitoring method to the study of the surface air layer pollution by heavy metals and radioactive substances in five urban industrialized areas located within the Kyiv city.

The heavy anthropogenic pressure in the selected explored areas did not allow the use of typical biological objects, lichens, and mosses as air pollution monitors. For this reason, the bark of black poplar (*Populus nigra L.*) was used, which, according to previous research, has proved to be a good alternative biological substrate indicator, especially when researching urban industrialized regions.

The sampling network was established based on the urban landscape typological principle, taking into account the features of the formation and movement of airflows. The choice of the location of the points also took into account the specificity of the particular objects emissions and the possibility of combined action of several pollution sources.



Location of the sampling point on the Kyiv map.

Samples of the bark of black poplar (*Populus nigra* L.), (*Evernia prunastri*, *Hypogymnia physodes* (*alpha*) Nyl, *Parmelia sulcata* Taylor, *Physcia adscendens*, *Xanthoria parietina*), mosses (*Dicranum polysetum*, *Pleurozium schreberi* (*Brid.*) Mitt) and soil were selected at this stage of work. Samples were selected in four Kyiv districts, which have the highest anthropogenic pressure (residential area "Troyeshchyna" (a potential source of pollution – Kyiv HPP-6), residential area "Kharkivskyy" (waste incineration plant "Energia"), residential area "Kurenivka" ("Lakma", printing plant "Zorya"), and Demiyivska Square (automobile transport)). Their location is shown in Figure.

In the area of the residential quarter "Troyeshchyna" (1) the following were selected: bark – 22 specimens, moss – 12 specimens, lichen – 13 specimens.

In the area of the residential quarter "Kharkivskyy" (2): bark – 32 specimens, lichen – 8 specimens.

In the area of the residential quarter "Kurenivka" (4): bark – 25 specimens, lichen – 2 specimens.

In the area of Demiyivska Square (5): bark – 21 specimens, lichen – 11 specimens.

At each point of the sampling network the bark was taken on the trunks of 3-5 lonely old trees (trunk diameter 25-50 cm) within the plots approximately 20×20 m in size. The top (dead) vegetation-free layer of bark 3-4 mm thick were cut with a sharp stainless steel knife around the barrel at the height of 120-150 cm and placed in specially labeled plastic bags. The total weight of the bark sample was at least 20-50 g.

Bark samples were dried at room temperature to air-dry. The samples were then crushed for 2 min with a plastic working mill with a caprolactam knife. The crushed sample was sifted through a 1×1 mm capron sieve. The obtained small fraction was homogenized using an electromechanical mixer for 15 min and submitted for analysis.

$^{137}\text{Cs}$  content was measured on a CANBERRA gamma-ray spectrometer with ultra-pure germanium detector GC6020.

The results of  $^{137}\text{Cs}$  measurements in some samples are given in the Table.

#### The results of $^{137}\text{Cs}$ measurements in bark samples

Demiyivska Square	Specific activity, Bq/kg	Residential quarter "Troyeshchyna"	Specific activity, Bq/kg	Residential quarter "Kharkivskyy"	Specific activity, Bq/kg	Residential quarter "Kurenivka"	Specific activity, Bq/kg
1	13±2	1	4±2	1	20±2	1	23±3
2	14±2	2	4±0	2	30±2	2	23±2
3	21±2	3	5,9±1,8	3	45±6	3	30±3

4	23±2	4	7±2	4	59±4	4	89±8
5	24±3	5	7,8±1,9	5	70±6	5	101±8
6	33±4	6	12±2	6	186±12	6	173±9
7	85±9	7	69±5			7	
8	162±13					8	
9	514±35					9	
10	737±46						

## STRONTIUM-90 AND CAESIUM-137 CONCENTRATION IN FISH OF THE CHERNOBYL NPP COOLING POND BEFORE AND AFTER DRAW DOWN OF WATER LEVEL

**D.I. Gudkov<sup>1</sup>, A.Ye Kaglyan<sup>1</sup>, K. Nanba<sup>2</sup>, T. Wada<sup>2</sup>, S.I. Kireev<sup>3</sup>, V.V. Belyaev<sup>1</sup>, L.P. Yurchuk<sup>1</sup>**

<sup>1</sup>*Institute of Hydrobiology of the National Academy of Sciences of Ukraine, Kyiv, Ukraine*

<sup>2</sup>*Institute of Environmental Radioactivity, University of Fukushima, Fukushima, Japan*

<sup>3</sup>*State Specialized Enterprise "Ecocentre", Chernobyl, Ukraine*

The submitted results of research were obtained during 2010-2019 using mainly the fish from the north-western part of the Chernobyl NPP (CNPP) cooling pond (CP) and its former water area after draw down of water level. <sup>137</sup>Cs and <sup>90</sup>Sr concentration in water and fish was measured using by gamma-spectrometric and radiochemical methods described (Gudkov et al., Kaglyan et al., 2019). The limited part of samples of the fish tissues were analyzed by method (Kaglyan et al., 2014, 2015).

We studied 16 fish species of different ecological groups: pike (*Esox lucius* L.), zander (*Sander lucioperca* L.), perch (*Perca fluviatilis* L.), wels catfish (*Silurus glanis* L.), channel catfish (*Ictalurus punctatus* Raf.), asp (*Leuciscus aspius* L.), common chub (*Squalius cephalus* L.), common sabrefish (*Pelecus cultratus* L.), common rudd (*Scardinius erythrophthalmus* L.), common bleak (*Alburnus alburnus* L.), Prussian carp (*Carassius gibelio* Bloch), tench (*Tinca tinca* L.), common bream (*Abramis brama* L.), common roach (*Rutilus rutilus* L.), European carp (*Cyprinus carpio* L.), and white bream (*Blicca bjoerkna* L.). The classification of fish by the type of feeding is based on the predominant type of nutrition in studied water bodies. The average number of fish in the annual sample for the most of species was about 15 individuals. The measurement error was 15-25%. The specific activity of radionuclides in fish is given in Bq/kg wet weight. Due to the fact that the change of the hydrological regime of the CP caused the change of the processes affecting the redistribution of radionuclides in the components of ecosystem of the pond, we compare the average specific activity of the radionuclides for two periods: the first one is 2010-2014 - before the drawdown of the water level, and the second one is 2019 - when the process of drawdown of the water level was completed.

The decrease in the water level of the CP resulted in the change of hydrochemical regime of the water body, as well as the remobilization of <sup>90</sup>Sr in the sediments and on the drained territories. In recent years we registered an increase in the concentration of <sup>90</sup>Sr in water in 2.5-3 times, which inevitably leads to an increase in the specific activity of radionuclide in fish. A more intense increase in the specific activity of <sup>90</sup>Sr occurs in pray fish species. Thus, during 2010-2014, the average specific activity of <sup>90</sup>Sr in the common rudd was 210±59 Bq/kg, and during 2019 it was reached 1320±345 Bq/kg, in the common roach 110±27 and 984±60 Bq/kg, in the Prussian carp - 90±25 and 825±67 Bq/kg, and in the European carp - 73±15 and 659±87 Bq/kg, respectively. In predator fish, the average specific activity of <sup>90</sup>Sr before the drawdown of water level in the CP was 115±49 in the perch, and during the period of 2019 it increased to 459±94 Bq/kg, in the zander - 65±9 and 275±17 Bq/kg and in the Wels catfish - 159±100 and 197±62 Bq/kg, respectively. An analysis of the dynamics of <sup>137</sup>Cs concentration in fish of the CP after drawdown of water level indicates that reliable changes in the radionuclide concentration were not occurred.

The radionuclide concentration in the representatives of almost all fish species (except zander and perch) remained at the same level with some fluctuations within the measurement error. Thus, the specific activity of <sup>137</sup>Cs in the common rudd during 2010-2014 was 1030±360, and in 2019 - 1033±211 Bq/kg, in the common roach - 1322±218 and 818±74, in the Prussian carp - 1559±29 and 1047±83, in the common carp - 1100±200 and 633±124, in the wels catfish - 2100±337 and 2800±484, in the perch 6650±826 and 3347±559, and in the zander - 5860±2700 and 1739±368 Bq/kg, respectively. The significant decrease of <sup>137</sup>Cs concentration in the perch and zander, which are, respectively, optional and obligatory predators, in our

opinion is related to the drainage of spawning grounds and, accordingly, the reduction of young fish quantity - the main food items of these species. Thus, the perch and zander find themselves in a food shortage and they are likely to be forced to switch to alternative food sources with less concentration of  $^{137}\text{Cs}$ , which accordingly reflect to the intensity of radionuclide accumulation by these fish species. It should be noted that the representatives of ichthyofauna of all other investigated water bodies of the Chernobyl exclusion zone (except the Pripyat River) a gradual decrease of  $^{137}\text{Cs}$  concentration in fish is going on, and the concentration of  $^{90}\text{Sr}$  remains practically unchanged.

Analysis of the radionuclide distribution in different organs and tissues of fish in the CP in 2019 showed that the highest specific activity of  $^{90}\text{Sr}$  is observed in the scales (2270-6627 Bq/kg), bones (821-2084 Bq/kg) and fins (1560-4884 Bq/kg), and the lowest - in the skin (28-80 Bq/kg), internal organs (14-330 Bq/kg) and muscles (11-30 Bq/kg). For the wels catfish, which lack of the scales, the highest concentration of  $^{90}\text{Sr}$  is determined in the bony spines of the pectoral fins (1725-2127 Bq/kg), in the bones (706-718 Bq/kg) and head (400-484 Bq/kg). More than 90% of  $^{90}\text{Sr}$  is concentrated in fish scales, bones, head and fins. In 2019 the highest specific activity of  $^{137}\text{Cs}$  was observed in fish muscles - 494-4367 Bq/kg, accounting for 35-70% of the total  $^{137}\text{Cs}$  content in the fish body. The analysis of the specific activity of  $^{90}\text{Sr}$  in organs and tissues of fish before the drawdown of water level in the CP in 2014 and during 2019 revealed that the content of radionuclide is increasing in all compartments of fish body, especially in the scales, bones, head and fins. However, no reliable dynamics of  $^{137}\text{Cs}$  concentration in organs and tissues of fish are observed.

The results of the study of the specific activity ratio of  $^{90}\text{Sr}/^{137}\text{Cs}$  in fish of the CP during 2010-2014 indicate that the  $^{137}\text{Cs}$  concentration of representatives of all fish species significantly outweighed the  $^{90}\text{Sr}$  concentration. It should be noted that due to the constant pumping of water from the Pripyat River into the CP (until November 2014), the specific activity of  $^{90}\text{Sr}$  in all fish species was significantly lower than the specific activity of  $^{137}\text{Cs}$  unlike other studied closed and non-flowing water bodies of the CEZ, in fish of whose the  $^{90}\text{Sr}$  concentration always outweighed the  $^{137}\text{Cs}$  one. For the pray fish species this ratio until 2014 was in the range of 0.05-0.48, and for the predatory fish - 0.005-0.150. During the period 2019 the specific activity ratio of  $^{90}\text{Sr}/^{137}\text{Cs}$  was reached to 0.48-2.13 for the pray fish species and 0.08-0.37 for the predatory ones. For the predatory fish, this indicator is much lower, since the assimilation of  $^{90}\text{Sr}$ , which is found in nutrients mainly in poorly digested bone tissue, is not as effective as  $^{137}\text{Cs}$ . It can be concluded that since 2016 the ratio of  $^{90}\text{Sr}/^{137}\text{Cs}$  concentration in fish of the CP has tended to increase. This is especially noticeable for the representatives of pray fish, e.g. for the common rudd the value of  $^{90}\text{Sr}/^{137}\text{Cs}$  in 2019 was predominantly greater than 1, indicating that fish have the  $^{90}\text{Sr}$  concentration above the  $^{137}\text{Cs}$  one.

Thus the drawdown of water level in the CNPP CP resulted in an increase of  $^{90}\text{Sr}$  in fish, which reached 438-2084 (923±235) Bq/kg during 2019 for the pray fish species and 176-567 (359±84) Bq/kg for the predatory fish compared to 41-285 (136±53) and 43-139 (84±28) Bq/kg during 2010-2014, respectively. The specific activity of  $^{137}\text{Cs}$  in this case was 526 - 1612 (931±245) Bq/kg for the pray fish of the CP during 2019, and 1318-4359 (2508±762) Bq/kg for predatory fish compared to 608-2327 (1073±338) and 1740-8340 (3273±649) Bp/kg during 2010-2014, respectively. The  $^{137}\text{Cs}$  concentration in fish during the period of studies with some oscillations within the measurement error remained at the same level or decrease, while the specific activity of  $^{90}\text{Sr}$  since 2016 increased, primarily due to an increase of radionuclide concentration in the water of the CP. The ratio of  $^{90}\text{Sr}/^{137}\text{Cs}$  in the representatives of ichthyofauna has tended to increase since 2016. For the pray fish species this value is increasing faster than for predatory fish. The specific activity of radionuclides in fish during the period 2019 exceeded the permissible levels, according to the standards adopted in Ukraine for fishery products in 5.0-59.5 times for  $^{90}\text{Sr}$  and in 3.5-29.9 times for  $^{137}\text{Cs}$  concentration.

This study was supported by the National Academy of Sciences of Ukraine, by the State Agency of Ukraine on the Exclusion Zone Management and also by the SATREPS Project "Strengthening of the environmental radiation control and legislative basis for the environmental remediation of radioactively contaminated sites". The authors wish to thank personnel of the state specialized enterprises "Ecocentre" and "Chernobyl NPP" for the promoting research within the Chernobyl exclusion zone.

Gudkov D.I., Kaglyan A.Ye., Nazarov A.B., Klenus V.G. Dynamics of the content and distribution of the main dose forming radionuclides in fishes of the exclusion zone of the Chernobyl NPS // Hydrobiological Journal. - 2008. - Vol. 44, No 5. - P. 87-104.

Kaglan O.Ye., Gudkov D.I. Patent for Invention No 106547. A method for determining the specific activity of radionuclides in organs and tissues of fish by their content in the scales. - Application dated 02.25.2013. - Registered in the State Register of Patents of Ukraine for Inventions 10.09.2014 (in Ukrainian).

Kaglan O.Ye., Gudkov D.I., Klenus V.G. et al. Patent for Invention No 107604. A method for determining the specific activity of radionuclides in organs and tissues of fish (perch and pike families) by their content in the fins. – Application dated 22.03.2013. – Registered in the State Register of Patents of Ukraine for Inventions 26.01.2015 (in Ukrainian).

Kaglyan A.Ye., Gudkov D.I., Kireyev S.I., Yurchuk L.P., Gupalo Ye.A. Fish of the Chernobyl exclusion zone: modern levels of radionuclide contamination and radiation doses // Hydrobiological Journal. – 2019. – Vol. 55, No 5. – P. 81–99.

## **RADIOMETRIC DATING OF SEDIMENT RECORDS IN MOUNTAIN LAKE SYNEVYR (THE UKRAINIAN CARPATHIANS) BY $^{210}\text{Pb}$**

**G.V. Laptev<sup>1</sup>, L.S. Pirnach<sup>1</sup>, G.V. Lisovyi<sup>1</sup>, G.A. Derkach<sup>1</sup> Y. Y. and Y.Y. Tyukh<sup>2</sup>**

<sup>1</sup> *Ukrainian Hydrometeorological institut*

<sup>2</sup> *Synevyr National Nature Park*

Dating of environmental archives, including bottom sediments of closed lakes, is an effective tool for reconstruction of the chronology of anthropogenic loads to environment during the industrial development in the last century or due to ongoing climate change. In such studies, undisturbed or low-polluted ecosystems are used as background objects for comparison purpose [1].

In the Ukrainian Hydrometeorological Institute (UHMI) sufficient experience of successful application of radiometric dating techniques using unsupported (excess)  $^{210}\text{Pb}$  for various types of natural sedimentary archives, such as Antarctic ice core or deep sea sediment have been achieved [2, 3].

The principles of radiometric dating of sediment accumulation are based on determination of the activity of natural radionuclides  $^{226}\text{Ra}$  and  $^{210}\text{Pb}$  in the sediment column using detailed slicing of its vertical distribution. The vertical activity profile of the unsupported  $^{210}\text{Pb}$  is recovered by subtracting the  $^{226}\text{Ra}$  activity from the total measured  $^{210}\text{Pb}$  activity for each of the analyzed layers. Chronology dating is then done using special mathematical models [4].

To corroborate the validity of the results of the  $^{210}\text{Pb}$  dating, additional information on the content of anthropogenic radionuclides, such as  $^{137}\text{Cs}$  and  $^{241}\text{Am}$  - products of nuclear testing in the atmosphere or due to accidents, is used as the time markers.

The purpose of this study was to apply the method for bottom sediments of a mountain lake located in the Ukrainian Carpathians. In the spring of 2019, a fieldtrip was carried out to the site of unique facilities within National Nature Reserve (NNR) Synevyr. The field work executed on the lake Synevyr comprised of bathymetric survey of the lake depth, testing water column and collection of undisturbed sediment cores. Furthermore, additional local objects studied were small lake Dyke, sphagnum oligotrophic swamps Zamshatka and Hlukhany, where samples of the sphagnum moss were collected. Based on the field bathymetric survey of the lake Synevyr bottom, a depth map was built, allowing to assign zones of the maximal depths (~22m maximal depth) suitable for collection of undisturbed sediment cores (Fig. 1).

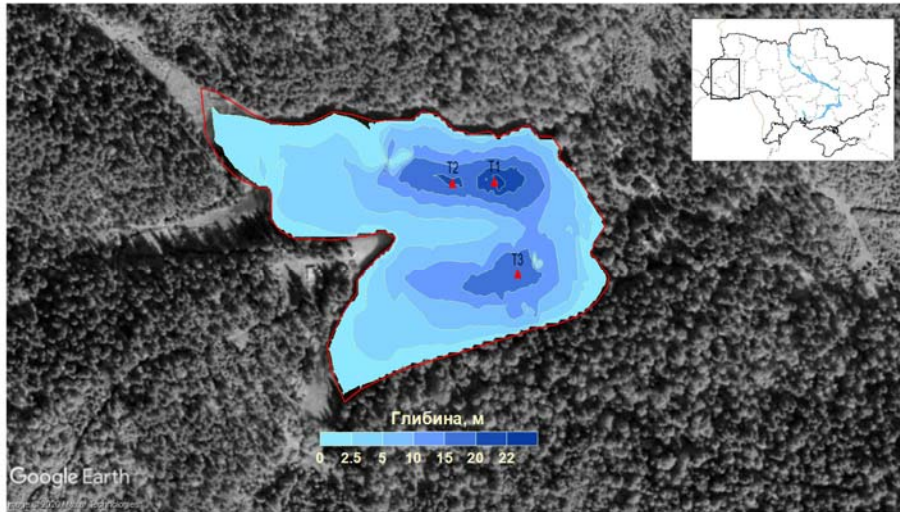


Fig. 1. – Depth map of the Synevyr Lake showing sites of the bottom sediment cores sampling

The first results of the study have also showed that the Lake Synevyr has strong vertical stratification as it was established by the absence of dissolved oxygen at depths below ca. 10 m. Most likely, this stratification is permanent, since the bottom sediments have a laminated (varved) structure, with a clear distinguished sediment accumulation fragments at the bottom of the lake.

The radiometric dating of collected sediment cores using model of unsupported  $^{210}\text{Pb}$  was carried out (Fig. 2). It was confirmed by additional measured vertical distribution of the anthropogenic  $^{137}\text{Cs}$ , which peak concentrations dated as 1963 (maximum of global nuclear weapons tests) and 1986 (Chornobyl accident) satisfactorily coincide with the chronological dates obtained by the lead method. Variations in sediment accumulation at the bottom of Lake Synevyr over the last 120 years have been established, as well as episodes of impulse ingress of erosion products from the catchment due to avalanches or extreme snowmelt.

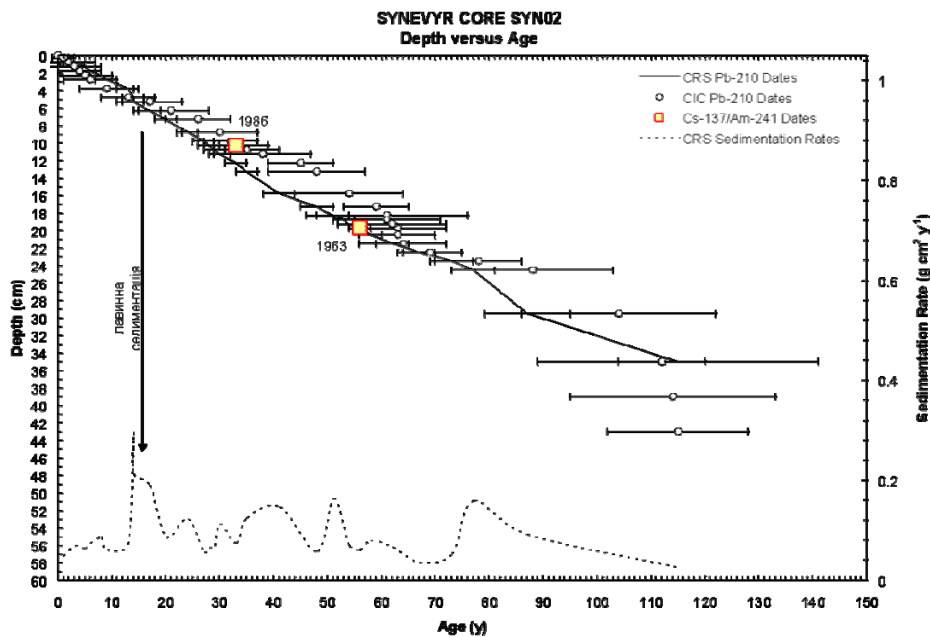


Fig. 2. – Chronological dating of sediment from Lake Synevyr suggested by unsupported  $^{210}\text{Pb}$

The obtained results infer that the Lake Synevyr can be considered not only as attractive tourist destination, but also as a prospectus geochronological archive for studying the history of the transformation of the sediment flows which carry evidence of anthropogenic load on the environment or the effects of ongoing climate change [5].

1. Appleby P. G. Radiometric dating of sediment records in European mountain lakes. // *Limnol.*, 59 (Suppl. 1): 1-14, 2000.
2. Лаптев Г.В., Костеж А.Б., Грищенко В.Ф. О датировании антарктического льда по содержанию  $^{210}\text{Pb}$  // *Наукові праці Укр НДГМІ – 1999.* - Вип. 247. – С. 207 - 216.
3. Лаптев Г.В., Войцехович О.В.. Перспективы радиометрического датирования как базового инструмента морской литодинамики современных морских осадков. Материалы Международной конференции «Литодинамика донной контактной зоны океана» ИОРАН, Москва 14-17 сентября 2009 г., с.151-156.
4. Appleby, P. G., Haworth, E. Y., Michel, H., Short, D. B., Laptev, G., & Piliposian, G. T. (2003). The transport and mass balance of fallout radionuclides in Blelham Tarn, Cumbria (UK). *Journal of Paleolimnology*, 29(4), 459-473.
5. Laptev G. The Black sea SST reconstruction for the past 2000 years using radiometrically dated sediment records from abyssal plain and continental slope. International Symposium on Isotopes in Hydrology, Marine Ecosystems, and Climate Change Studies, Monaco, 27 March–1 April 2011.

### **SPECIFIC FEATURE OF RADIONUCLIDES DISTRIBUTION IN MOSS COVER OF THE UKRAINIAN CARPATHIAN MOUNTAINS**

L. S. Pirnach<sup>1</sup>, G. V. Laptev<sup>1</sup>, E. S. Todosiienko<sup>2</sup>

<sup>1</sup> *Ukrainian Hydrometeorological institute,*  
<sup>2</sup> *Taras Shevchenko National University of Kyiv*

The natural physical and geographical features of the landscapes influence the deposition of atmospheric pollution, including radioactive, on the territories over which air masses extend. The most important role is played by the mountain ranges. Specific geographical and climatic features of the mountains lead to an increased deposition of radioactive atmospheric fallouts over their territories. In Western Europe, mountainous areas have been found to show a higher activity of  $^{137}\text{Cs}$  in the environment than most the flat areas [1].

This paper summarizes the 2016-2019 studies conducted in the Ukrainian Carpathian Mountains, which could be contaminated during the formation of the so-called Chernobyl “southern trail” in 1986. Field work was performed on various elements of relief at the Carpathian Biosphere Reserve (Chornogirsky, Svidovetsky and Marmarosky massifs) and Gorgany Reserve. Special attention (about 70% of the sampling sites) was given to the highest altitude alpine sites, among them 11 highest peaks of the Ukrainian Carpathians.

The purpose of this study is to identify patterns of landscape differentiation of natural ( $^{210}\text{Pb}$  and  $^{40}\text{K}$ ) and anthropogenic ( $^{137}\text{Cs}$  and  $^{241}\text{Am}$ ) radionuclides at different geographical scale levels.

Local screening of the radiation doses was carried out “in situ” to identify areas with higher activity (“hot” spots) and sampled. Most of the samples collected were mossy soil. Mosses are known by enhanced levels of concentration the contaminants, radionuclides and heavy metals in particular. This allows them to be attributed to the plants-indicators of local technogenic pollution. In addition, mosses are found in all vertical mountain ranges and is a significant biogeochemical barrier to the vertical and horizontal migration of radionuclides in forest biocoenoses [2].

Field radiometric measurements at different arrays of the Ukrainian Carpathians revealed the presence of small ca.1 m<sup>2</sup> spots with increased level of equivalent radiation doses (up to 0,14-0,16 μSv/h, as much as twice higher compared to the neighbouring sites). Conditions which are favourable for the accumulation of snow cover were observed for some of these places (in particular, on the Svidovetsky massif).

Analytical work was carried out in the UHMI laboratory including measurements of gamma emitting radionuclides using gamma spectrometry system equipped with HPGe detector GMX40 (ORTEC).

About 90 measuring samples prepared from 70 sampling points have been investigated to date.

Analysis of the results<sup>1</sup> of gamma emitting radionuclide activity concentration revealed in particular the following statistically significant (P = 0,99) Pearson Product Moment Correlation (PPMC).

---

<sup>1</sup> Radionuclide activity at the time of measurements made in 2016-2019 in the text is given

For the mossy cover of all the study areas, a high linear correlation was established between the dry bulk density of the measured samples (DBD) and the content of natural radionuclides  $^{210}\text{Pb}$  (reverse) and  $^{40}\text{K}$  (direct correlation). This indicates the bounding of radionuclides to different soil constituents:  $^{210}\text{Pb}$  — organic and  $^{40}\text{K}$  — mineral, provided that the radionuclides are uniformly distributed over the area: mainly due to atmospheric flux for  $^{210}\text{Pb}$  or indicative for mineral particles  $^{40}\text{K}$ . A strong Pearson correlation was established between the content of these two elements in the samples (Fig. 1 a)), which allows estimating in a certain interval the specific activity of one element in the presence of the results of determining the other (for example,  $^{40}\text{K}$  by  $^{210}\text{Pb}$ ).

In case of  $^{241}\text{Am}$  it was concluded that further research is needed, although in general its distribution is similar to  $^{210}\text{Pb}$ . This might be the result of long term chronic radioactive fallout in the region starting from a period of intensive atmospheric nuclear tests in 1950-60s and well known increase of  $^{241}\text{Am}$  activity with time due to radioactive decay of the parent  $^{241}\text{Pu}$ .

Unlike other investigated radionuclides,  $^{137}\text{Cs}$  is clearly differentiated by the content both on larger scale and locally. In particular, on the Chornogirsky ridge and its eastern slopes  $^{137}\text{Cs}$  activity is observed to be two orders of magnitude more than on other arrays. The southwestern edge beyond the peak of Petros, which probably lies beyond the Chornogirsky spot, is significantly cleaner in the territory of Chornogora.

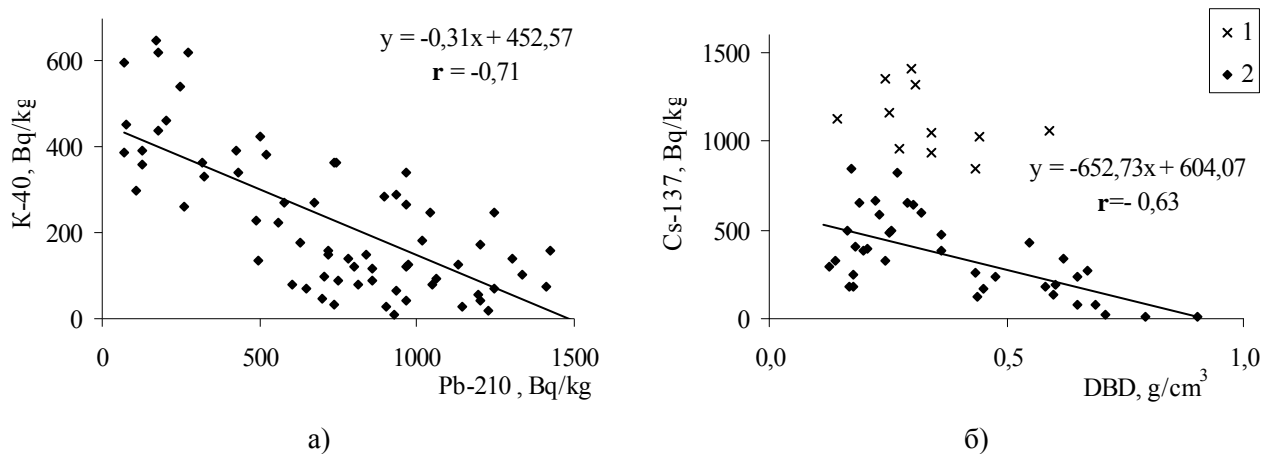


Fig. 1. Diagrams of dispersion and correlation between: a) concentrations of  $^{210}\text{Pb}$  and  $^{40}\text{K}$  (for all investigated areas); b) the specific activity of  $^{137}\text{Cs}$  and DBD for sampling of the ridge and the eastern part of Chornogora with 1, 2 - group.  $r$  is the Pearson correlation coefficient.

At the same time, the presence of spots (100 cm<sup>2</sup> at most) containing  $^{137}\text{Cs}$  in the top layer of moss cover over 1000 Bq/kg (dry weight) is observed in the Chornogora. Taking into account that for adjacent sites the activity of  $^{137}\text{Cs}$  is sometimes less than half, it is possible to make an assumption about the presence in the accidental fallout of the so-called “hot” particles with increased specific activity.

The correlation analysis of the measurements of 50 sampled mosses from the ridge and southern slopes of Chornogora follows in line with this hypothesis. If about 20% of measured samples with the highest specific activity above 850 Bq/kg (which can be conditionally attributed to presence of “hot” particle in initial fallout, group 1 in Fig. 1 b), are discarded from the statistical analysis, a noticeable correlation of  $^{137}\text{Cs}$  with the organic matter content is observed (group 2 in Fig. 1 b) as it should be, given the adsorption properties of this soil type with respect to the  $\text{Cs}^+$  cation.

It should be noted that all the areas where the highest levels of concentration  $^{137}\text{Cs}$  have been found are also characteristic with the established meteorological prolonged period of stable snow cover [3]. It was suggested that the most likely they were covered with the snow at the time of the Chernobyl accident fallout in 1986. Moreover, during that period atmospheric precipitation could occur in the form of direct snowfall, which intensively traps the solid atmospheric aerosols e.g. smallest Chernobyl-origin radioactive particles [4].

The results of research showed that redistribution of radionuclides, both natural and anthropogenic, over different elements of the mountain’s landscape depends on the absorption properties of the mosses which superimpose the accumulative properties of the relief itself. Mosses demonstrate a strong intercept function in vertical and horizontal migration of radionuclides.

1. Pourcelot L., Louvat D., Gauthier-Lafaye F., Stille P. Formation of radioactivity enriched soils in mountain areas. *J. Environ. Radioactivity*, №68, 2003, P. 215-233.
2. Болюх В.А., Вирченко В.М. Накопление радионуклидов мхами Украинского полесья // *Украинский бот. журн.* 1994. Т. 51. №4. С. 39-45.
3. Довідник зі снігового покриву в горах України. УкрНДГМІ МНС України. НАН України. Київ-2013.- 218 с.
4. Алексеев В.Р. Снежный покров как индикатор кумулятивного загрязнения земель // *Лед и снег.* 2013. № 1 (121). С. 127 – 140.

## **RADIATION MAPPING AND «RADIATION WEATHER» PARAMETERS ON THE RESEARCH OF WETLAND «CHORNE BAGNO»**

Svatiuk N.<sup>1</sup>, Maslyuk V.<sup>1</sup>, Symkanich O.<sup>2</sup>, Sukharev S.<sup>2</sup>

<sup>1</sup> *Department of Photonuclear Processes, Institute of Electron Physics, Uzhhorod, Ukraine,*

<sup>2</sup> *Department of Ecology Environment, Uzhhorod National University, Uzhhorod, Ukraine,*

It is known about the importance of all types of radiation: terrestrial, cosmic, and man-made origin, as factors of its permanent impact on the life and evolution of biota. The life of biota takes place on the surface of a natural nuclear reactor such as earth, and radiation itself is as important as other natural factors: terrestrial gravity, the composition of the atmosphere. so far, little is known about the mechanisms of adaptation and protection of living organisms to the action of ionizing radiation, the role of radiation in the metabolism of living organisms, whether it is integrated into energy processes at the cellular level? We can say that the set of radiation factors in the territory in which living organisms, including humans, form the parameters of "radiation weather" [1]. These include the presence and intensity of the emitters  $\alpha$ -,  $\beta$ -,  $\gamma$ -radiation, the structure/spectra of terrestrial radiation, and for high-altitude regions, the radiation characteristics of the Earth's cosmic zones are essential. The levels of terrestrial radiation are unevenly distributed over the earth's crust and depend on the composition and concentration of radioactive isotopes of natural (radionuclide U, Th, Np series, <sup>40</sup>K, cosmogenic) and technogenic origin. The most recent ones, caused by numerous accidents at nuclear facilities and the effects of military nuclear testing, have a significant impact on the structure of terrestrial radiation and are a constant source of anxiety. However, the risks associated with the consequences of nuclear catastrophes have stimulated the creation of databases of proliferation, accumulation of radionuclides by living organisms, the features of their adaptation and evolution under the conditions of radiation factors [2], as well as the development of radioecological studies of the environment, not technogenic. Radioecology has considerable potential to form a picture of the existence of biological species in the conditions of natural radiation factors, assessing threats when they change: decrease/increase, change in the structure of radiation. Such problems arise in long-term space expeditions, plans for the colonization of other celestial bodies.

The ideas of radiation (radiogeochemical) mapping of the environment as an essential component of the biosphere were initiated by the first president of the academy of sciences of Ukraine V. S. Vernadsky [3]. His work is associated with an understanding of the fundamental role of radioactivity for human existence, the concomitant release of heat in the evolution of the Earth, "wide-into-earth-permeability", the patterns of propagation and accumulation of natural radionuclides. In Europe now is implementing a large-scale program to create a European atlas of natural radioactivity, which began in 2006 [4]. The subject of such mapping is the distribution of the U/Th/<sup>40</sup>K chemical elements in the terrestrial surfaces and their daughter radioactive products of their transformations (<sup>220,222</sup>Rn), estimates of the cosmic radiation intensities, and the data of the monitoring of the geogenic radon potential. The first results of radiation mapping and the concept of "radiation weather" on the example of protected areas of Transcarpathia were presented in [5].

In this paper, the methodology for the approach to the estimation of terrestrial factors of "radiation weather" is based on the idea of the quasi-equilibrium of nuclides of natural series U, Th, Np, which determine the activity structure of the natural background, as well as the presence of radionuclides of anthropogenic origin. The degree of deviation from such equilibrium is different for different objects of the

environment: soils, reservoirs, rocks, as well as due to the different man-made activity on the territory. Radiation weather parameters can be estimated by setting their standards through the specific content of fixed sets of radionuclide-tagged natural series [5]. This technique makes it possible to control the equilibrium state of nuclides of natural U/Th series in the objects of study of this territory since their selected sets have different half-lives  $T_{1/2}$ . Creating bases for standards for radionuclide content of natural and man-made origin and radiation mapping is vital for a number of applications, and first of all to set the parameters of "radiation weather" and to assess the ecological status of the territory. These data are also important for the problems of nuclear dating, the establishment of time scales and the nature of global factors, which can lead to the disturbance of the equilibrium of nuclides of natural series U, Th [6].

When it is possible to talk about the age equilibrium between the content of isotopes of natural series, it allows evaluating the atomic content  $N_i$  of the corresponding chemical elements of the  $i$ -th grade in the

samples. Thus, for known ratios,  $\frac{T_{1/2}^{(Th)}}{T_{1/2}^{(U)}}$ ,  $\frac{T^{(Th)}}{T^{(40K)}}$  and  $\frac{A^{(Th)}}{A^{(40K)}}$ ,  $\frac{A^{(Th)}}{A^{(U)}}$ , respectively, half-lives and activity

standards of U / Th series and  $^{40}\text{K}$ , the ratios of their chemical elements expressed in atomic percentages, U: Th: K, are determined from the equations:

$$\frac{N_{Th}}{N_U} \cong \frac{T_{1/2}^{(Th)}}{T_{1/2}^{(U)}} * \frac{A^{(Th)}}{A^{(U)}}, \quad \frac{N_{Th}}{N_{40K}} \cong \frac{T_{1/2}^{(Th)}}{T_{1/2}^{(40K)}} * \frac{A^{(Th)}}{A^{(40K)}}, \quad (1)$$

The patterns of propagation and distribution of radionuclides that form the indicators of radiation weather were investigated on the "Chorne Bahno" wetland model. Soil samples, as specimens of protected areas, were sampled on the surface, at a depth of 20 cm, and a depth of more than 50 cm, according to standard procedure, along with mountain ranges and ridge valleys. Fig. 1 shows the result of the radiation mapping performed for wetland "Chorne Bagno," which shows the deep propagation of uranium and thorium radionuclides. Such maps allow us to obtain data on the content standards of chemical elements by the number of Th and U atoms using formula (1) and to investigate their migration ability.

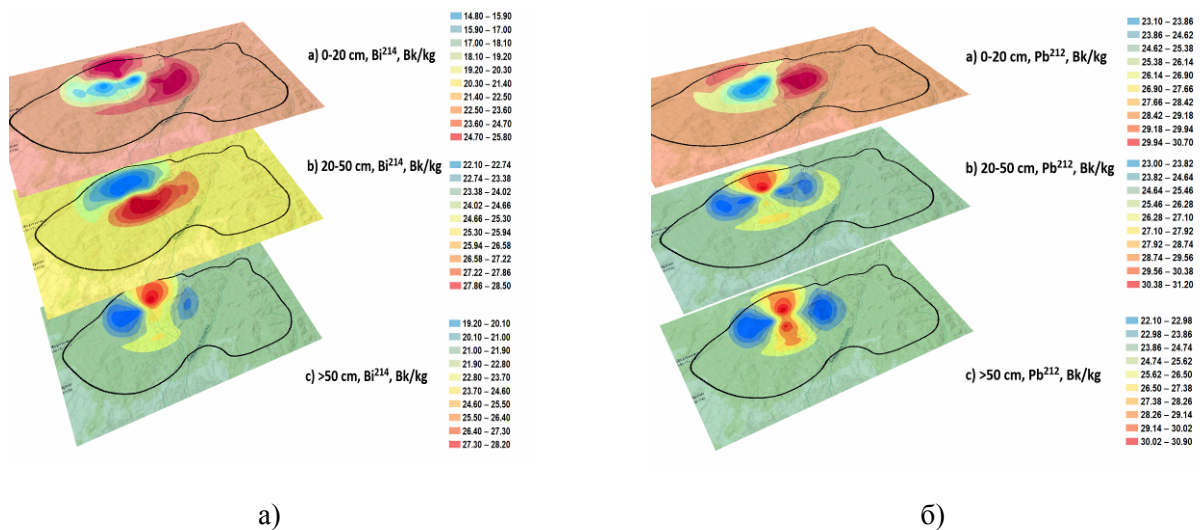


Fig. 1 Radioactive mapping data of the wetland "Chorne Bagno", Transcarpathia: a) the distribution profile of natural uranium radionuclides; b) respectively, for the thorium series.

Thus, the results of radioisotope studies allow obtaining an estimation of the geochemical parameters of the protected areas of Transcarpathia. The activity standards of isotope markers can be used to establish the parameters of "radiation weather." For radiation identification of the territory, it is essential the data on the atomic content of U:Th:K [5]. The data in Fig. 1 indicates the importance of accounting the migration ability of nuclides of U/Th/K series in radiation mapping problems. The same methodology can be applied to other regions.

2. Mycobiota of Ukrainian Polesie: the consequences of the Chernobyl disaster / N. N. Zhdanova, V. A. Zakharchenko, A. I. Vasilevskaya and others. - Kiev: Kiev, 2013. - 382 p.
3. Vernadsky V.I. About radioactive chemical elements in Earth's Korea. Practical medicine. 1915. № 10–11. Pp. 143–195.
4. Cinelli G., et al Journal of Environmental Radioactivity V. 196, January 2019, P. 240-252
5. Svatiuk N., Maslyuk V., Symkanich O., Sukharev S. Radiological, concept: “Radiation weather” and “radiation identification of the environment” *Uzhgorod University Scientific Bulletin. Series: Physics №44. Uzhgorod, 2018. C. 99 - 108.*
6. Pop O., et al Radiochimica Acta, V. 107, Issue 3, 2018, P. 207–213.<sup>1</sup>